University of Strathclyde

Department of Chemical and Process Engineering

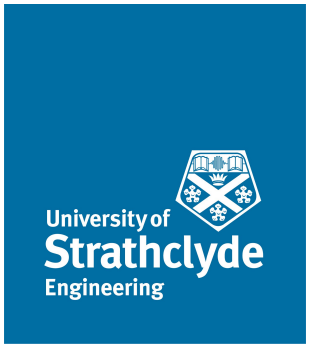

Fractional Flow for Reversed Flow Boundary Condition in Foam Improved Oil Recovery (IOR)

by

Eneotu, Maclean Jacob

Under the Supervision of Dr Paul Grassia

Reader, Department of Chemical and Process Engineering

A thesis submitted to the Department of Chemical and Process Engineering, University of Strathclyde in partial fulfilment of the requirements for

the degree of Doctor of Philosophy (PhD)

June, 2021

Contents

List of Figures

List of Tables

Declaration

'This thesis is the result of the author's original research. It has been composed by the author, has not been previously submitted for examination which has led to the award of a degree, and is submitted to the Department of Chemical and Process Engineering, University of Strathclyde in partial fulfilment for the award of the degree of Doctor of Philosophy in Chemical and Process Engineering.' References and citations have been provided to acknowledge previously published papers and theses used in this study.

Signed..... **Date**.....

Acknowledgements

First and foremost, I would like to express my sincere gratitude to my supervisor; Dr Paul Grassia for his support through these years. With the support and guidance provided by him, I have been able to achieve my goals. Without his continued guidance and support, I am sure that achieving my end goals would not have been easy. My thanks also goes to the Petroleum Technology Development Fund – PTDF, Nigeria under whose sponsorship I undertook this research.

My sincere thanks also goes to Professor George Hirasaki and Professor William Rossen of William Marsh Rice University, Texas, USA and Delft University of Technology, Netherlands respectively. As experts in this area of research, their immense knowledge, ideas and suggestions have been sources of encouragement in the course of my research.

Finally, I would like to express my gratitude to my parents, my brother, uncles and aunties. Without their tremendous support, understanding and encouragement in the past few years, I'm sure this journey would have proven to be a difficult one. Also, my sincere thanks to my research group members; Carlos Torres-Ulloa, Yaw Boakye-Ansah and Elaheh Esmaeili for a cherished time spent together researching around the same subject area; foam. Special thanks to Carlos Torres-Ulloa for helping me get up to speed with MATLAB which proved invaluable in my research.

Abstract

Due to the special flow properties of foam compared to those of conventional liquids and gases, injecting foam into oil reservoirs can be an excellent way of extracting the oil in place. This ability of foam as an efficient IOR mechanism is made possible by its tendency to cause a reduction in the mobility of the injected gas; consequently increasing the gas sweep efficiency. In addition, foam helps to suppress viscous fingering that conventional CO_2 or gas injection could cause.

In foam improved oil recovery (IOR), it is usually the dispersed gaseous phase (that is, gas within foam) that displaces the residual oil left behind by primary and secondary oil recovery methods. It is also possible to envisage a reverse case in which the liquid phase (partly oil, but usually containing a significant amount of water plus some surfactant), pushes invading fluid back; hence allowing for flow reversal. This could happen at depth on a foam front if, for example, the gas injection pressure declines or alternatively as a new injection well comes online downstream of the foam flow. In that situation, initially foam will be displacing water. Then at a certain time, flow reversal takes place. The simplest model for this is $q_t(t > t_r) = -q_t(t < t_r)$; where '$t_r$' is the instant in time at which reversal takes place, 'q_t' is total fluid flow rate and 't' is any arbitrary time other than 't_r'. Hence, foam displaces water up to 't_r', then water starts displacing foam for $t > t_r$. This study is focused on how multiphase (i.e. foam and water) flow in porous media as described by the fractional flow model, behaves when this sort of reversal happens.

Using the fractional flow model and the method of characteristics (MOC), this study has shown that during flow reversal, there is a shock – that is, a jump in water or liquid

saturation 'S_w' between foamed gas with a small amount of water (downstream of the shock) and water with a small amount of foamed gas (upstream of it). The magnitude of the jump in water saturation at the shock grows over time. Depending on how quickly over time the water saturation 'S_w' decreases downstream of the shock and how quickly 'S_w' grows upstream of it, the speed of the shock (itself determined by a Rankine-Hugoniot condition or integral mass balance) is found to vary in different ways over time. Typically, the tendency is that the shock speed decreases with time, at least initially. The position of the shock can also be updated provided the speed is known. Moreover, once an updated position of the shock is specified at any instant in time, so called characteristic fans ahead of and behind it can be used to determine water saturations on either side of the shock. Characteristics are lines of constant liquid saturations in a distance–time plot, while fans are sets of characteristics with different liquid saturations spreading out from a point in the plot.

Thus, it is possible to iterate between determining water saturations across the shock (based on intersections of characteristic lines at the current shock location) and determining (based on those saturations) how fast the shock moves at any given instant and where it will be at a later time. This study also suggests that during flow reversal in foam IOR, characteristics that start off behind the shock will collide with the shock as they move downstream, whilst the shock itself will collide with characteristics ahead of it. Ultimately, the overall solution to the foam IOR problem during flow reversal will depend on the interaction between the two characteristic fans. The solution for the propagating shock also makes it possible to contrast the mobility of the foam front during the forward and reverse flow stages.

Chapter 1

Introduction

The main aim of this thesis is to provide an understanding into how oil recovery modelled by the fractional flow theory behaves when there is a change in flow direction during foam improved oil recovery (IOR). In this Chapter, the importance of this research has been highlighted. Section 1.1 gives a general background information on oil and gas production cum oil recovery processes, and foam improved oil recovery process. An overview of what happens in a flow reversal process involving foam is briefly described in section 1.2. The aim and objectives of this research have also been outlined in section 1.2. Finally, section 1.3 gives the structure/outline of the thesis.

1.1 Research context

Hydrocarbons (oil and gas) are usually produced first by using the reservoir natural drive (that is natural energy sources of the reservoir). According to Tarek and Nathan (2012), these sources of energy in the reservoir could be from aquifer expansion when an aquifer exists (this natural drive is called water drive) or from gas cap or solution gas expansion (this type of natural drive is collectively called gas drive). The difference between the two gas drive mechanisms is that, in gas cap drive, the primary source of reservoir energy is an initial gas cap (that is free gas) that exists in the reservoir, while in solution gas expansion,

the source of reservoir drive energy is usually from the expansion of the reservoir fluids and the rock. The nature of the reservoir, whether undersaturated (i.e., where reservoir pressure $>$ bubble point of oil) or saturated (where reservoir pressure $\leq$ bubble point of oil) determines which mechanism plays the dominant role (Tarek and Nathan, 2012).

In an undersaturated reservoir where no free gas exists, the reservoir pressure remains above the bubble point, hence the reservoir drive energy is provided only by the limited expansion of the reservoir fluids (i.e., oil and water) and rock. In a saturated reservoir, as production or extraction of oil takes place, bubbles of gas begin to evolve and expand thereby providing the needed energy. It is important to note that as bubbles of gas begin to form and are liberated from the solution (i.e., oil and water), there will be shrinkage in the volume of oil produced. Be that as it may, this shrinkage will be more than counterbalanced by the expansion of the solution gas. Hence in such reservoirs, the primary source of energy is still provided by the solution gas expansion.

The processes described above are collectively called primary recovery or production. During the process of primary recovery, the reservoir pressure is considerably higher than the bottom-hole pressure inside the well-bore. This high natural differential pressure drives hydrocarbons toward the well and up to the surface. During primary recovery though, only a small percentage of the initial hydrocarbons in place are produced, typically around 10% for oil reservoirs (Speight, 2017).

The next stage is then secondary production during which external fluid such as water or gas is injected into the reservoir through injection wells located in rock that has fluid communication with production wells, thereby helping to maintain reservoir pressure and to displace hydrocarbons toward the well-bore. The successive use of primary recovery

and secondary recovery in an oil reservoir produces about 10% to 40% of the original oil in place (Zendehboudi and Bahadori, 2017).

Rather than simply trying to force the oil out of the reservoir, as did the previous two methods explained above, there is another production method which seeks to primarily alter the properties of the reservoir fluids (i.e. oil in the case of oil reservoir) particularly to make it more conducive to extract. This method or mechanism is termed enhanced oil recovery or tertiary recovery or improved oil recovery. These terms are sometimes used interchangeably even though formally, they differ. On the one hand, enhanced oil recovery (EOR) is the main process itself, while tertiary recovery is used when an enhanced oil recovery method is applied after primary and secondary recovery, in fact, EOR can be applied at any stage of reservoir development, hence the term tertiary recovery is less commonly used nowadays. On the other hand, improved oil recovery (IOR) encompasses enhanced oil recovery (EOR) methods as well as new drilling and well technologies, intelligent reservoir management and control, advanced reservoir monitoring techniques and the application of different enhancements of primary and secondary recovery processes (Fanchi, 2002; Surguchev et al., 2005). For the purpose of this study, EOR and IOR are used interchangeably as meaning the same thing.

There are three main IOR methods (Dake, 1978; Al-Jarba and Al-Anazi, 2009), including thermal recovery (which involves the introduction of heat such as the injection of steam to lower the viscosity or thin the heavy viscous oil, and improve its ability to flow through the reservoir), gas injection (which uses gases such as natural gas, nitrogen, or carbon dioxide CO_2 that can be introduced into a reservoir to push additional oil to a production well-bore and that can lower the viscosity of the oil), and chemical injection (which can involve the use of long-chained molecules called polymers to increase the effectiveness of

waterfloods, or the use of detergent-like surfactants to help lower the surface tension that often prevents oil droplets from moving through a reservoir). These methods can either be used independently or in combination with one another. For instance, when surfactant is alternated or mixed with gas, a foam tends to be formed, which is the main focus of this study.

As has been mentioned, in oil and gas production, flow to the surface under the reservoir's drive mechanisms or natural drives including water drive, gas drive (gas cap and solution gas expansion), only produces a meagre fraction of the original oil in place (Clark, 1969; Dake, 1978). Even after primary and secondary production, a reasonable amount of oil or gas could still be left in a reservoir. In order to push the remaining oil and gas out, external or non-reservoir fluids are usually injected into the reservoir. This displacement process is known as enhanced oil recovery (EOR) or in a broader term improved oil recovery (IOR) when it includes other techniques or processes all aimed at pushing the left over oil and gas out. One of such fluid that can be injected back into the reservoir is foam (Ali et al., 1985; Sheng, 2013). It is very promising for oil displacement and easy to produce in-situ a hydrocarbon reservoir by injecting alternate slugs of surfactant solution and gas.

Due to foam's special flow properties compared to those of conventional liquids and gases, early studies including Ali et al. (1985), Ploeg and Duerksen (1985), Liu and Besserer (1988), etc. have shown that injecting foam into oil reservoirs is an excellent way of extracting the oil in place. Foam achieves this favourable sweep efficiency (that is effective or efficient oil recovery process) through the reduction of gas mobility which in turn prevents injected gas from simply surging to the reservoir's top where it would fail to displace the oil, thereby controlling the motion of all the other reservoir fluids that

are present including the oil being displaced. In addition, foam helps to suppress viscous fingering that conventional CO_2 injection could cause (see figure 2.4 later on). The foam is usually driven through the oil reservoir under the action of an imposed pressure.

Foam can either be injected into a reservoir after it has been formed at the surface (i.e. by co-injecting surfactant and gas) or foam can be formed in-situ by alternating the injection of surfactant slugs and gas; this is commonly referred to as surfactant-alternating-gas injection (SAG). The latter is often preferred (Shan and Rossen, 2004); but either way, the foam is driven through the oil reservoir under the action of an imposed pressure.

1.2 Foam in improved oil recovery and objectives of the PhD project

In this section, an overview of foam in improved oil recovery (IOR) has been presented (section 1.2.1), and then the aims and objectives of the thesis have also been outlined (section 1.2.2).

1.2.1 Overview of foam in improved oil recovery (IOR)

Despite the above advantages that foam offers as stated in section 1.1, it is known to be an intrinsically complex fluid. As such, the physical rules governing its movement or propagation in porous media have still not been thoroughly established. At the moment though, one thing that is fully established according to Bernard et al. (1965), Gillis and Radke (1990) and Tang and Kovscek (2006) is that when foam is injected into a reservoir, it has the ability to help in diverting part of the injected gas (foamed gas to be specific) into the previously unswept and hence oil-rich zone of the reservoir, thus helping in an

efficient oil recovery process. In the study of Shan and Rossen (2004), it was stated that during the process of foam improved oil recovery, a narrow foam front of finely-textured, very low-mobility foam is generated at the leading edge of the gas bank. This front, which has very low mobility, separates downstream liquid (that is, surfactant solution and oil) from upstream injected gas (usually in the form of coarsely-textured, moderately low mobility foam). A proper understanding of how the aforementioned finely-textured, low mobility foam front evolves over time is key to understanding the foam improved oil recovery process itself.

During flow in one direction, this foam front consisting of finely-textured, low-mobility foam tends to grow in thickness gradually with time, whilst still covering a narrow region with respect to the reservoir's scale. The foam front also slows over time. There is currently no knowledge or study at the moment that has attempted to look into what will happen if the foam front changes direction. Changes in flow direction are likely occurrences in hydrocarbon extraction whenever additional injection and/or production wells are brought on stream as pressure fields then change. This could also happen if a pump feeding an injection well were to fail or alternatively if for any reason, an injection well is shut-in, thereby causing reservoir pressure downstream to build up again (relative to upstream pressure) particularly at depth and consequently causing some liquid to move in the opposite direction. Even though this situation could happen, it has never been analysed or modelled in the past. Hence, in this thesis, some mathematical equations underlying fluids displacement in porous media, the consequences arising from changes in the flow direction will be studied with respect to the foam front motion. The research aim and objectives have been outlined below.

1.2.2 Research aim and objectives

The main aim of this work is to study how oil recovery model by the fractional-flow theory (one of the best established models for flow of multiple phases in oil reservoirs (Buckley and Leverett, 1942)) behaves when there is a change in flow direction during foam improved oil recovery (IOR). To achieve this aim, the following objectives have been set out:

- Study the foam flow mechanism in porous media.
- Study the application of the fractional-flow theory, the Buckley and Leverett (1942) equation, which is a frontal advance equation, coupled with equations for the mobility of oil-water system (Brooks and Corey, 1964) and in a foam-water system (Persoff et al., 1991).
- Study how a foam shock front (such a solution being admitted by fractional flow theory) propagates in a porous medium during reversed flow.
- Indicate how the pressure-driven growth model of foam improved oil recovery must be reformulated to account for flow reversal during the foam displacement process.

1.3 Structure of the thesis

This thesis is submitted in accordance to the University's Regulations 20.1–20.5. It is structured as follows: Chapter 2 provides literature review including properties of foam and foam formation, foam flow in porous media and its uses in enhanced or improved oil recovery, field applications of foam and a number of foam models, etc. Chapter 3 introduces the main problem to be addressed in this thesis which is the behaviour of the

fractional flow model when there is a change in flow direction (that is flow reversal). It also draws analogies with a related problem which involves boundary conditions being changed at a certain time, but no flow reversal. This Chapter also provides the method and algorithm on how to solve the problem to be addressed in this thesis. Chapter 4 presents and discusses the results of this research. Chapter 5 contains a published paper (Eneotu and Grassia, 2020) titled **"Modelling Foam Improved Oil Recovery: Towards a Formulation of Pressure-Driven Growth with Flow Reversal".** This Chapter basically explains how to reformulate the so called pressure-driven growth model of foam flow (a 2-D model), taking into account flow reversal, using an understanding of the behaviour of the fractional flow theory during flow reversal considered in previous chapters. A 1-D fractional flow theory underlies the 2-D pressure-driven growth model. Conclusions and insight on future work that can be studied as complement to this research are then stated in Chapter 6.

Chapter 2

Literature Review

This literature review chapter is laid out as follows. Section 2.1 deals with the definition/description of foam and how it is is formed. Section 2.2 then deals with properties of foam. After that, section 2.3 deals with foam flow in porous media. Finally, section 2.4 deals with how foam flow in porous media is modelled.

2.1 Foam and its formation

Foams are complex agglomerations of gas bubbles separated from each other by thin liquid films (Bikerman, 1953). It is pertinent to distinguish between bubbly liquids and foams. In bubbly liquids, the bubbles are well separated from each other; the diffusion of the gas is between the bubbles and the solution which acts as a reservoir of gas. Moreover, the smallest bubbles in bubbly liquids have a greater pressure relative to the liquid, and they lose more gas than they receive, while in foams, the largest bubbles receive more gas from the liquid and/or neighbouring bubbles than they lose to it, so the small bubbles shrink and the largest bubbles continue to grow (Cantat et al., 2013). The industrial or practical applications of foam include but are not limited to oil recovery, ore separation, vehicle manufacture, food products, industrial cleaning. A foam can be formed in two main ways (Walstra, 1989). The first method is by the supersaturation of liquid with

gas, either by dissolving gas under pressure and then releasing the pressure or by simply allowing gas to form in situ. The second method is a mechanical method where gas is either injected through narrow openings or by beating - formation of bubbles in the wake of a fast-moving rod (Walstra, 1989).

The bubbles initially formed are often large. They can be broken into smaller ones by invoking a high velocity gradient in the liquid, which causes shearing forces to act on the bubbles. As soon as bubbles have formed, several changes start to occur. The changes according to Walstra (1989) are:

- Smaller bubbles dissolve, while bigger ones may grow in size, by diffusion of gas through the continuous phase. This is called disproportionation or Ostwald ripening.
- Bubbles rapidly cream, thereby causing segregation into a foam layer on top of a bulk liquid.
- Bubbles deform one another, leading to a polyhedral foam.
- Liquid drains from foam to the bulk.
- Lamellae between foam bubbles rupture, leading to their coalescence.

According to Walstra (1989), some processes occur faster than others during foam formation; notably the first and fifth process listed above are often slower. The remaining processes may occur almost simultaneously and the processes may enhance each other; for example, the fourth process enhances the fifth process. Another important piece of information in the formation of foam concerns the liquid and gas content, hence the classification of foam into dry and wet foam. On one hand, a dry foam is one with little

liquid content and high gas fraction. Dry foam is sometimes called polyhedral foam as it is composed of thin films separating bubbles (see figure 2.1). On the other hand, wet foams sometimes known as spherical foams (again see figure 2.1) because of the spherical shape they adopt have a large percentage liquid content and low gas volume.

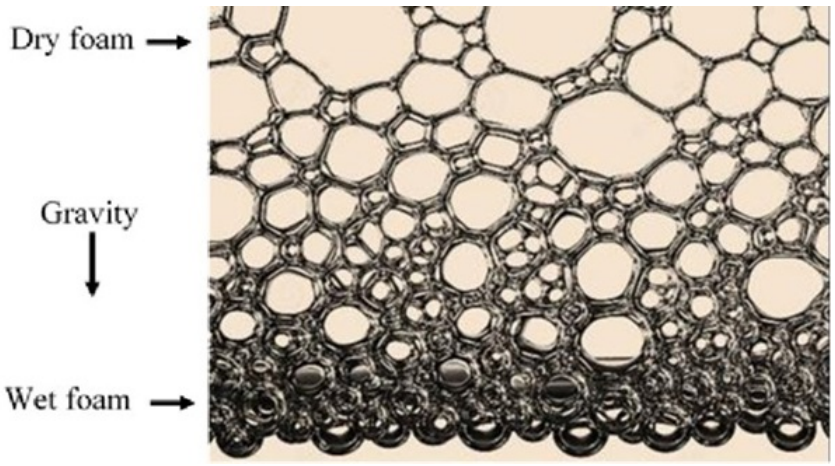

Figure 2.1: Foam structure in the form of dry and wet and its variation under gravity (Akbari et al., 2018).

Another classification of foam is based on the length or size of the bubble and the size of the confining vessel in which the foam is placed. Based on this, foams could be macro-foam or micro-foam. Macro-foams are foams in which the size of the confining container is much bigger than the bubble size. Examples include foam flow through pipes or foam flow at the surface of coatings which contains bubbles usually greater than 100 µm that tend to rise very quickly. According to Stokes' Law, the larger the bubble size, the faster the rise through the fluid, because the velocity of the bubble rising through the fluid will be directly proportional to the square of the radius of the bubble (Hallack et al., 2010). In micro-foam however, the size of the confinement which the foam is comparable to the size of the bubble. Moreover, the foam bubble can become entrained within the liquid due to the fact that the rise to the surface of the liquid is typically not fast as a result of having small radius bubbles usually between 10 to 100 µm (Hallack et al., 2010). Examples include flow in capillary tubes and foam flow in porous media where

the size of the bubbles forming the foam are comparable to the pore dimensions. In cases like these, wet or dry foams can be formed (Kraynik, 1988; Kovscek and Radke, 1993a), but the wet foam region will not consist of spherical bubbles due to the confining pores. From the foregoing, it is pertinent to note that the type of foam that is of interest to this project is foam within a porous medium (Kovscek and Radke, 1993b). Some foam properties however describe general characteristics of foams, whether confined or not. Before proceeding however, it is also important to describe some general characteristics of foams.

2.2 Foam properties

In terms of foam properties, one important static property is surface tension between gas and water. This property is important because as stated previously, foams are comprised of liquid films and gas bubbles. Thus, in the thermodynamic sense, foam is an unstable system. When foams are generated, the surface area of liquid is increased and surface energy is increased. In accordance with the principle of Gibbs free energy, the system will tend to lower the surface energy state as it initially has large free energy. Moreover, a lower surface tension reduces the energy of the foam system, thereby favouring foam stabilisation. The common substance used in achieving a low surface tension is surfactant. The presence of a surfactant is essential for making and stabilising a foam. A surfactant adsorbs onto the air-water interface, thereby lowering the surface tension. In consequence, a surfactant also lowers the energy cost of creating foams (AlYousef et al., 2017). In fact, according to Belhaij et al. (2014), the foamability or foaming capacity and stability of foams increases with an increase in surfactant concentration up to the so called critical micelle concentration (CMC). However, above the CMC there is not any

significant effect of addition of yet more surfactant (Belhaij et al., 2014). The critical micelle concentration (CMC) is simply defined as that surfactant concentration above which micelles (micelles are just molecular aggregates) begin to form. The physical implication of the CMC is that above the CMC, the surface tension does not reduce further, because the formation of micelles is a sign that the fluid-fluid interfaces are fully occupied by surfactant molecules. Thus, CMC somehow specifies the limiting concentration for practical use of surfactant. In this work, the interest is in a case where surfactant solutions are used together with gas in oil reservoirs with residual oil saturation, such that oil is initially immobile. The surfactant and gas are injected alternately, hence the process is called surfactant-alternating-gas (SAG) process.

Generally, foam properties are considered in terms of foam drainage, foam rheology, foam coarsening and foam collapse. In each case, the structure of the foam plays a role. In particular, structural rearrangements (often described as topological changes) are often seen as the essential feature of the behaviour of a foam (Weaire et al., 2001). Foam drainage is simply the transport of liquid through the foam, driven by gravity or pressure differences (e.g. capillary pressure differences). When this happens, foam is said to have been drained. This process is similar to *creaming* in emulsions where the drainage rate is usually not so pronounced, being slowed due to the closeness in the densities of the fluids (say oil and water), unlike in foams where the density difference between the fluids is usually larger. A model in which the liquid drains only through the Plateau borders (the liquid-filled channels between the bubbles), with a Poiseuille (or no-slip) boundary condition, works well in many cases as the true boundary condition at the boundaries between air and liquid films or Plateau borders is not fully known (Weaire et al., 1997). An understanding of this process, particularly in the limit of low liquid fraction, has been

aided by the development of non-linear foam drainage equations (Weaire et al., 1997). The study of these equations is however beyond the scope of this work.

Foam rheology has to do with how foam responds to externally imposed stress. Depending on the magnitude of stress, foam may exhibit several rheological behaviours. At low strain, hence low stress, some foams can behave like elastic solids thereby causing the bubbles to be deformed, without causing any modification to the packing topology since the applied strain is too small (Weaire et al., 2002). However, at a critical yield stress, the packing topology can change and the foam will flow. In a flowing foam, the stress is composed of a yield stress part plus a dissipative (viscous) part.
As the stress increases, foams can thereby exhibit non-Newtonian behaviour (i.e. do not show constant viscosity independent of stress); instead the effective viscosity falls as the stress increases. Then, at a very high stress, foams can behave like a Newtonian fluid - liquid-like (Weaire and Hutzler, 1999).

As stated previously, when foam is formed, it is dynamically unstable. As it evolves towards 'thermodynamic equilibrium' (it is pertinent to note that foams are always unstable, they will approach thermodynamic equilibrium but not actually reach it), there is a reduction of the total surface area thereby leading to a growth in the average size of the bubbles over time. These changes are primarily due to the diffusive exchange of gas through the liquid films because of pressure differences between bubbles. They can also be caused when the liquid films between the bubbles are ruptured. This latter effect can actually be minimised by using a surfactant that generates stable films. These changes experienced by the bubbles that form the foam are what contribute to foam coarsening or foam collapse. Ultimately, certain bubbles will shrink and collapse, so as time goes on there are fewer and fewer bubbles in the foam. Drainage also plays its part (Weaire

et al., 1997) by making films more susceptible to breaking. Indeed a factor that influences foam collapse is film stability as a decrease in thickness of the film can rupture the film and eventually lead to foam collapse (Manlowe and Radke, 1990). As stated before, film stability is a function of surface tension and other forces acting on the film. A lower surface tension can aid in the stability of individual films and ultimately the foam stability. These processes including foam drainage, coarsening and rheology are actually interdependent. For example, drainage results in a drier foam with increased rheological shear modulus and accelerated coarsening, while coarsening in turn enhances drainage, but also decreases the rheological shear modulus (Kraynik, 1988; Saint-Jalmes and Durian, 1999). A schematic of their interdependence is shown in figure 2.2. The coupled phenomena of drainage, coarsening, and foam collapse are somewhat complicated, and their in-depth study is not in the scope of this thesis.

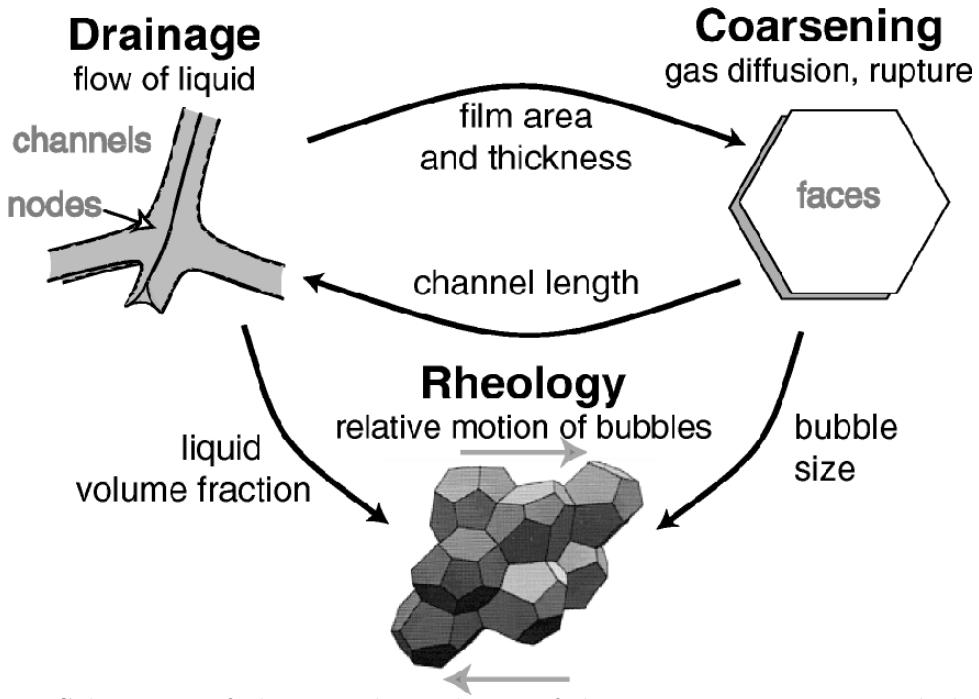

Figure 2.2: Schematic of the interdependence of drainage, coarsening, and rheology of foams (Durand and Langevin, 2002).

2.3 Foam flow in porous media

According to Hirasaki (1989), foam in porous media is usually described as a distribution or dispersion of gas in a liquid such that the liquid or aqueous phase is continuous, while some part of the gas phase is made discontinuous by lamellae (that is thin liquid films) as shown in figure 2.3. It is important to state that in porous media, there is no such thing as a bulk foam phase because bubbles tend to be comparable in size with pores. Moreover most of the liquid usually separates from the gas once foam enters into a porous medium. Much of the liquid takes up the smaller pore spaces that it will fill even if foam is not present; with gas and foam lamellae occupying the larger pore spaces. When foam is injected into a hydrocarbon reservoir for the purpose of enhanced oil recovery (EOR), it traps a large portion of gas in place. In other words, foam generally consists of both trapped and flowing gas. The small-to-medium pore spaces in the porous medium are normally occupied by the trapped gas, while the flowing gas tends to occupy the largest pores with lamellae separating bubbles (Almajid, 2019). It is the liquid lamella trapping the gas that creates friction at the Plateau border between them and liquid films at the pore walls. This is where most of the friction comes from and eventually resulting in a low mobility of the lamella, and therefore a decreased mobility of the gas between them (Gillis and Radke, 1990; Tang and Kovscek, 2006).

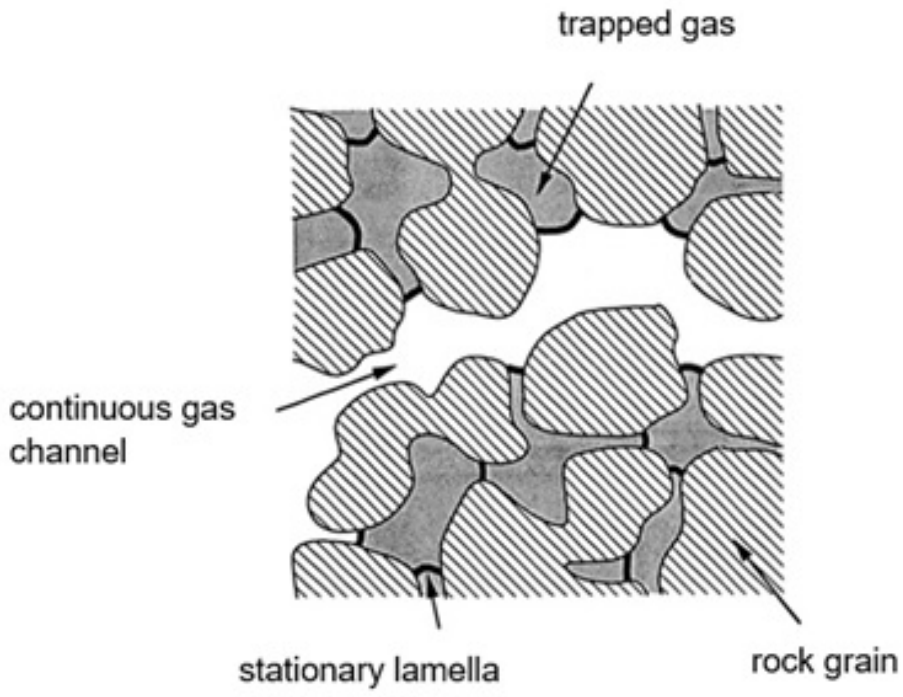

Figure 2.3: Schematic of foam in porous media (Kovscek and Radke, 1993b).

The injection of foam into (or production of foam within) a reservoir therefore has the ability to cause a reduction in the gas mobility caused by the presence of thin liquid films (lamellae). This proves advantageous compared to conventional gas injection where the sweep efficiency (i.e. the overall measure of the effectiveness of an enhanced oil recovery method) of the reservoir is poor despite the displacement efficiency (i.e. fraction of oil recovered from a zone that is actually swept by a displacement process) being good. In a conventional gas injection, because of low gas density which equates to high gas mobility, there will be the problem of gravity override (Rossen and Lim, 1995; Shan and Rossen, 2004; Boeije and Rossen, 2014) – a phenomenon whereby the injected gas will override most of the liquid or oil-rich zones it is supposed to be displacing, as instead gas will tend to surge to the top of the reservoir. Also, viscous fingering or viscous instability problem often associated with conventional gas injection could arise (Homsy, 1987). This is because with a higher viscosity ratio (between displaced and displacing fluid), an uneven fingered profile could be created as the gas flows through the reservoir

(even in a porous medium or reservoir which has a homogeneous permeability). This is even worse in heterogeneous reservoirs where preferential paths in high permeability zones could also lead to fingering as the gas flows through zones with the highest permeability in the reservoir. As a result, a significant amount of recoverable oil is bypassed. In severe cases, following preferentially regions of high mobility, gas will then start to flow towards the production wells thereby 'overriding' the reservoir. Ultimately, there will poor oil recovery with high production rates of injected gases (Shan and Rossen, 2004).

Figure 2.4 illustrates the advantage of foam injection over conventional gas injection. Foam is also advantageous compared to a water alternating gas (WAG) process (Farajzadeh et al., 2016; Sagbana et al., 2017); even though this process improves sweep efficiency, it eventually suffers from viscous instabilities and gravity segregation and therefore will also prove unsuccessful when it comes to controlling the gas mobility. Thus, by foaming the gas and therefore reducing its mobility especially in the regions to be swept or regions of high permeability in a reservoir, the problems encountered in a conventional gas injection or even a more advanced form of gas injection which involves alternating water and gas (i.e. water alternating gas injection, WAG as mentioned above) can potentially be overcome. To summarise, when foam is introduced into a reservoir or has been formed in situ, it reduces the mobility of the gas by trapping a large amount of the gas, so that part of the gas is diverted into the oil-rich part of the reservoir and therefore enhances the oil recovery.

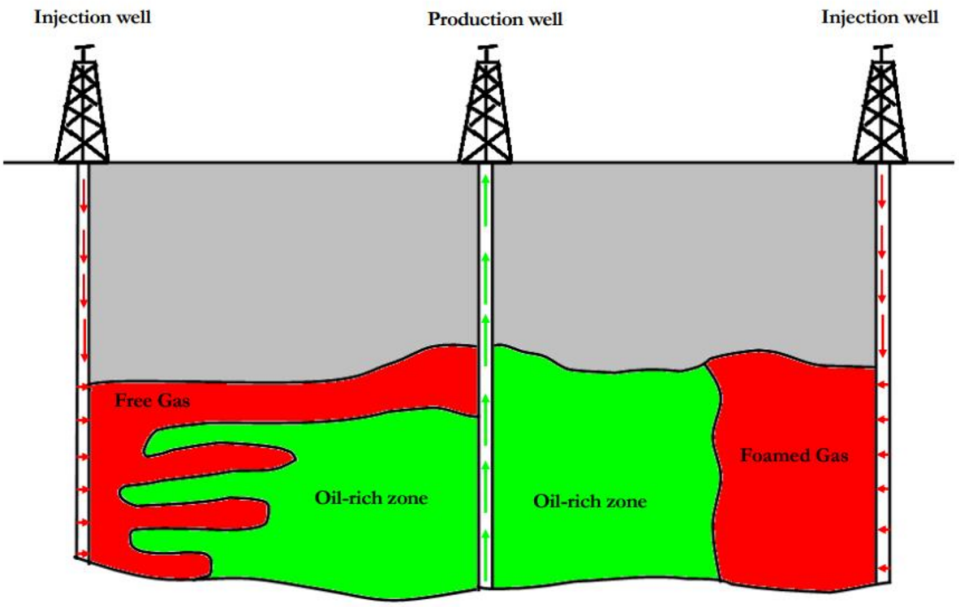

Figure 2.4: Schematic of conventional gas injection versus foam injection showing a modification of the gas profile caused by foam (Farajzadeh et al., 2012a).

Furthermore, according to Farajzadeh (2009), foam can affect the oil recovery process in two main ways: (a) by increasing the displacing fluid viscosity, thereby stabilising the displacement process and (b) by causing a reduction in the capillary forces between the foam and the oil, considering foam as a continuous phase (continuum scale model), thereby reducing the interfacial tensions due to the presence of surfactant (this is particularly important in chemical foams; that is chemical-chemical stabilised foams). In addition, the interfacial mass transfer between gas and oil will also play an important role in mobilising the oil in-place by dissolution, viscosity reduction and oil swelling. Oil swelling is simply the increase or expansion in the volume of the crude oil in a reservoir due to the complete or partial dissolution of a solvent (in this case gas, say CO_2) molecules into the crude oil (Fakher et al., 2020). The mass transfer of the gas phase across the gas-oil interface and the molecular diffusion of the gas inside the oil phase is what controls the rate of the dissolution of the gas (Rezk and Foroozesh, 2018). As such, in the presence of swelling, more interfacial mass transfer will be made possible since the gas is in more contact with oil.

2.3.1 Generation of foam in porous media

When discussing foam generation in porous media, three flow regimes usually encountered in the field application of foam must be considered (Rossen, 1996). These regimes include the region of the surface facilities and well where bulk foam could be created as a result of turbulence, the next flow regime is at the sandface (that is the downhole completion interface or the physical interface between the reservoir formation and the wellbore) and the region close to the sandface where pressure drop and flow rates are usually high. The third flow regime is then the formation proper, further away from the injector where flow rates and pressure drop are much lower. It is important to note that even though during experiments to study foam generation, the process of lamellae (thin films) creation is an important part of foam generation process, this is still distinct from foam generation itself (Rossen, 1996). A simple way to distinguish between these two processes is to realise that in foam flow, whether foam texture is refined or not, individual lamellae are continually created and destroyed (Falls et al., 1988). This process of continuous creation and destruction of individual lamellae is different from actual foam generation which is generally defined as the initial creation of a foam from gas and surfactant solution (Rossen, 1996).

As stated above though, the process of lamellae creation is an integral part of foam generation. At least three mechanisms of lamellae creation are contained in literatures, viz. lamellae division, snap-off and leave-behind (Ransohoff and Radke, 1988; Rossen, 1996). These mechanisms account for foam generation in situ a porous medium. In a porous medium with several pore throats, when a moving lamella enters the porous medium, lamellae stretch, break and reposition new lamellae in each unblocked pore

throat. This happens when for instance, an upstream bubble (called the parent or mother bubble) is being squeezed against an obstacle and then touches another bubble (called the fragmenting bubble), thereby subdividing the existing or parent bubble into fragments or daughter bubbles (see figure 2.5). This explains the mechanism of lamellae creation through lamella division. For snap-off, this mechanism of lamellae creation is made possible when there is accumulation of liquid in narrow pore spaces thereby bridging the pore throat, which ultimately creates a new interface in the throat as seen in figure 2.6. This mechanism usually requires both low and high capillary pressures at various stages of the process - a low capillary pressure in order to allow liquid to re-invade the throat and a high capillary pressure so as to allow gas to take up the space at the throat (Dharma, 2013). Several literature sources including Falls et al. (1988), Rossen (1996), Tanzil et al. (2002), Rossen (2003), Rossen (2008), and Kovscek et al. (2007) have stated that the snap-off mechanism depends on the heterogeneity of the porous medium-cum-reservoir, and the local dynamic capillary pressure between the liquid and the bubble spanning the pore-spaces. In the study of Almajid et al. (2019), the authors stated that in porous media, between the snap-off mechanism and lamella division, the former is more dominant. The third mechanism of lamellae creation and, by extension, foam generation, is leave-behind. According to Dharma (2013), the leave-behind mechanism only takes place during a drainage process – i.e. when a non-wetting phase is used to displace a wetting phase during enhanced oil recovery processes. This mechanism occurs when adjacent pore bodies are invaded by gas from different directions, thereby creating lamellae in the throat between adjacent pore bodies as shown in figure 2.7. In leave-behind, lamellae are created parallel to the flow direction, which is often associated with continuous-gas foams with low to moderate mobility reduction, i.e. just low to

moderate ability to restrict gas flow (Gauglitz et al., 2002). These 3 mechanisms of lamellae generation are shown in figures 2.5–2.7.

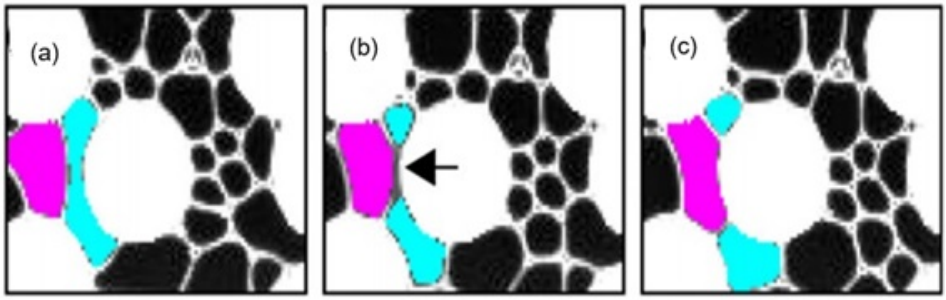

Figure 2.5: Schematic of lamella division. (a) shows a parent bubble coloured cyan touching a fragmenting bubble coloured purple. The arrow in (b) shows the position at which the splitting lamella touches the fragmenting obstacle or bubble, thereby triggering the division process leading to the 2 fragments in (c) (Géraud et al., 2017).

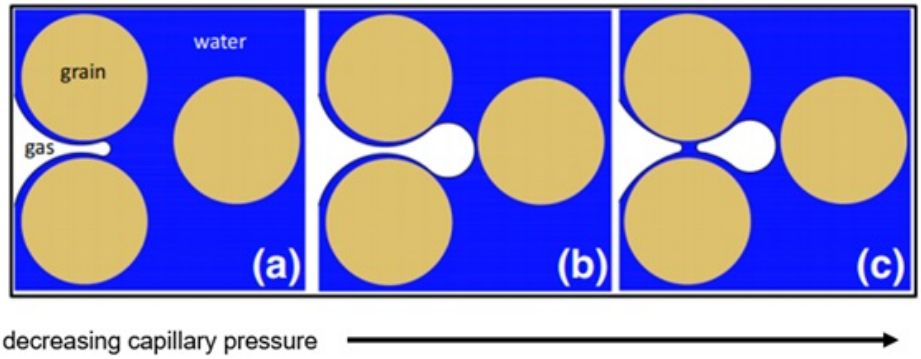

Figure 2.6: Schematic of snap-off mechanism of lamella creation in a pore-throat. The capillary pressure here is defined as the gas-to-liquid pressure difference (Almajid and Kovscek, 2020).

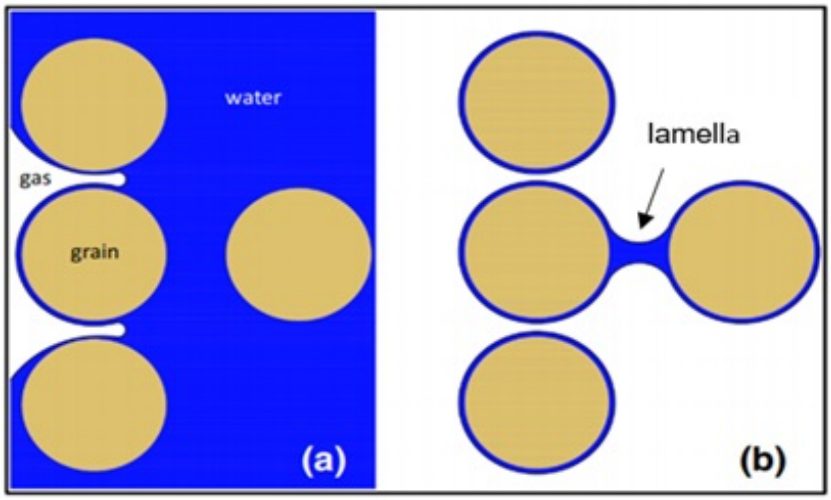

Figure 2.7: Schematic of leave-behind mechanism of lamella creation. (Almajid and Kovscek, 2020).

Experimentally, foam generation is usually inferred from a sudden drop in the mobility of the gas flowing through a porous medium. Be that as it may, sometimes, strong foam generation might not occur, but there could still be a small reduction in the mobility of gas. This is usually due to a static foam with few lamellae blocking only a few gas pore throats (Mohanty, 1981; Friedmann et al., 1991). Furthermore, it is pertinent to know that foam generation in oil and gas formations (oil-bearing rocks) bears no resemblance to bulk foam generation in pipes and other large flow channels. On the one hand, in foam generation in pipes and other large flow channels, shear flow could break large bubbles apart to create smaller bubbles (Harris, 1989). On the other hand, in real life porous media, lamellae are usually created by capillary forces and not viscous forces (Rossen, 1996). To study these phenomena in the laboratory, various artificial foam generators exist, which attempt to either increase turbulence (and hence induce shear) or in some cases even act as artificial porous medium to generate foams. The study of Friedmann and Jensen (1986) considered several laboratory foam generators of the artificial porous media type.

The authors considered two foam generators (sandpacks additionally prepacked with different steel-wools). Both generators had the same physical dimensions, but the latter was tightly packed compared to the former. The principle behind these foam generators is that, rather than allowing the chemical interaction of the foaming agents to generate foam, mechanical tools (i.e., foam generators) are incorporated into a foam flooding experiment such as the one shown in figure 2.8, to mix the foaming materials, and hence provide the needed energy to generate foam. It must however be noted that there are also cases when foam generators are not needed. In such cases, there is usually enough turbulence in the system to generate the foam. A particular case was the field test by

Ploeg and Duerksen (1985), where there was enough turbulence in the system while injecting sulfonate-nitrogen along with steam. As such, no significant effects were observed on the pressure or energy needed in order to generate foam.

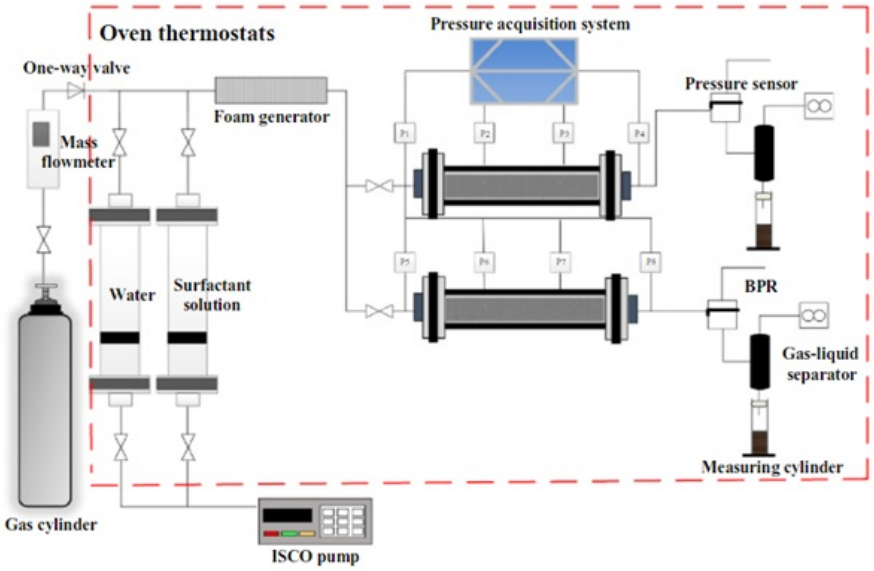

Figure 2.8: Schematic diagram of conventional foam flooding experiment with a foam generator Chen et al. (2020).

In hydrocarbon reservoirs, foams can be created by shear flow in the reservoir if surfactant solution and gas are injected simultaneously (Harris, 1989). Here, the surfactant can even be dispersed in the gas phase, say CO_2 phase (Kuhlman et al., 1994). During this process, water is not required to be added as there is water available in the reservoir (Ashoori et al., 2009). Foams can however also be created if surfactant solution and gas are alternately injected into a reservoir. According to Rossen (1996), the process of foam generation depends on the conditions of injection. For instance, in the study of Rossen and Gauglitz (1990) and Friedmann et al. (1991), it was found that foam formed when nitrogen gas and surfactant liquid were steadily and simultaneously injected in a porous medium, for a given surfactant concentration. The two main factors affecting foam generation were injection rate and foam quality (i.e. flowing gas volume fraction). According to the authors, the lower the proportion of liquid in the injected fluids, the higher the injection

rate needed to generate foam. In other words, for a given proportion of liquid, foam generation will tend to occur at relatively high gas velocity which in practice is limited to the near-wellbore region.

2.3.2 Propagation of foam in porous media

Once foam is introduced into a reservoir, it needs to move, being transported or propagated through the reservoir to help in sweeping the residual oil. The ability of foam to spread across large portions of the reservoir, and the speed with which it does so, are crucial to the extent of flow diversion obtained and the economic success of the project. In fact, foam propagation is the key to the mobility control foam process (Skauge et al., 2020). In the context of improved oil recovery or petroleum engineering, foam propagation is simply the growth of the region of low gas mobility. This region of low gas mobility could be a region of discontinuous foam (that is where the path of the gas motion through the medium is broken up by liquid lamellae). Foam propagation can also occur by the growth of a region of continuous-gas foam (but this has not quite such a low mobility as a discontinuous-gas foam would have, because the gas is not hindered by lamellae, hence a continuous gas flow path can be found), which spreads as the surfactant is transported in the reservoir (Rossen, 1996). For continuous-gas foams, any foam propagation relies on surfactant propagation, while for discontinuous-gas foams, propagation is necessarily by movement of gas bubbles. For these foams, propagation is prevented if either foam plugs the formation completely but also if foam collapses completely as it spreads. The latter possibility is the greater concern in field application. Therefore, the issue of foam propagation is closely related to the mechanisms of destruction of lamellae. Several literature sources including Chambers and Radke (1990), Falls et al. (1989), Jiménez and

Radke (1989) and Itamura and Udell (1989) have discussed these issues.

As stated above, in continuous-gas foam, foam propagation is a reliant upon surfactant propagation. In fact, according to Rossen (1996), the rate of surfactant propagation is an upper limit to the rate of foam propagation in porous media. Thus, the slow rate of surfactant propagation alone can make a foam-mobility control process economically inviable. Two factors that can delay surfactant propagation are the fact that surfactant solution must fill the liquid-saturated pore spaces, and must also satisfy the adsorption requirements of the rock surface. For instance, Persoff et al. (1991) showed that if a 99% quality (i.e. 1% liquid) foam flows through a rock with 35% liquid saturation, then 35 pore volumes (PV) of foam must be injected to provide the 0.35 PV of liquid required to displace surfactant-free liquid from the pore space. In this case, to enhance surfactant propagation, a large slug of surfactant can be used to precede the foam. However, if this is done, surfactant can be significantly lost to the rock surface by adsorption, precipitation and even dissolution in residual oil (Kuhlman et al., 1992). Generally, if an injected water contains large amount of clay, divalent ions and low solution pH, there will be an increase in surfactant losses (Lau and O'Brien, 1988; Kwok et al., 1993). In addition, large oil saturations also increases surfactant losses (Mannhardt et al., 1993).

From the above, it can be seen that surfactant adsorption is a significant factor in foam EOR projects. Thus, in field application of foam for the purpose of enhanced oil recovery, surfactant adsorption levels are usually lowered significantly either by reducing surfactant concentrations (where possible) or using sacrificial agents (Hong et al., 1987; Kuhlman et al., 1992; Prieditis and Paulett, 1992). Another point worthy of mention as it relates to foam propagation in field application of foam for the purpose of EOR processes, is that in the near well-bore region where foam generation is usually feasible, foam tends

to propagate with same velocity as surfactant (Rossen, 1996; Gauglitz et al., 2002). The concept of the "limiting capillary pressure" has also been used to link foam propagation, foam mobility and foam texture (see section 2.4.3.2 for details). The model to be discussed in that section concerns modelling foams up to a limiting capillary pressure P_c^* for foam collapse, foam propagation then being represented only in terms of capillary pressure and the transport of water (or aqueous surfactant solution), with foam texture becoming a secondary or implicit variable. By definition, capillary pressure is simply the pressure difference across the interface between two immiscible fluids in contact, in a small capillary tube (in this case in a porous medium), usually expressed in terms of wetting phase and non-wetting phase. In a gas-water system, gas is considered as the non-wetting phase while water is the wetting phase. In other words, the capillary pressure simply defines the difference between the pressure in the non-wetting phase and that in the wetting phase. For aqueous foams in water-wet media, it is simply the pressure difference between the dispersed gas phase and the continuous liquid phase. Large capillary pressures tend to suck liquid out of foam films which can promote foam collapse.

2.3.3 Field applications of foam injection

There have been several foam field applications over the years, and these are reviewed in what follows. Most foam applications in oil wells using gas injection are targeted at gas mobility control in injection wells as well as gas blocking in production wells.

There are basically two ways of injecting foam into a reservoir during enhanced oil recovery (EOR) field projects. The first method is by simultaneously or co-injecting gas and liquid (that is surfactant and water) at a fixed ratio. The foam quality is usually determined by the ratio of the gas flow rate to the total flow rate (that is sum of the gas

and the liquid flow rates). Kuehne et al. (1990) mentioned one co-injection case where an extremely effective EOR foam was created in flow through a baffled pipe and choke valve on the surface. The second method is alternately injecting surfactant and gas slugs into a reservoir, leading to the generation of foam in-situ of the porous medium. This method is called surfactant-alternating-gas (SAG) injection, alluded to earlier. The first method is usually preferable for the creation and maintenance of foam around the injection well (i.e. near-well region). Also, in a heterogeneous reservoir to ensure that all layers are invaded by foam, this method is usually preferred (Farajzadeh, 2009). However in order to improve sweep efficiency when injecting foam by this method, the injection well pressure must be raised. This could lead to the formation becoming fractured. This is the disadvantage of this method of foam injection. SAG injection on the other hand tends to cause low mobility foam to form solely at the gas-surfactant solution front, and can proceed at more modest pressures. According to Shan and Rossen (2004), SAG (foam) displacement processes at fixed injection pressure controls gravity override better than SAG processes at fixed injection rate or continuous foam injection processes.

Other studies including Zhou and Rossen (1995); Farajzadeh (2009) have also shown that when a SAG foam injection process is carried out as opposed to co-injection of surfactant and gas, the contact between water and gas in surface facilities and piping is minimised. This is particularly important when the gas, e.g. CO_2, forms an acid upon contact with water. Huh and Handy (1989) in their laboratory study also revealed this happening under certain conditions, when co-injecting surfactant and gas, while it never occurred with the SAG foam injection process. It was shown however that with the same gas flow rate, the mobility reduction factor for SAG (and hence the degree of mobility control) is lower than for co-injection foam. Nevertheless an example of a field application of foam

injection was in Snorre field in the Norwegian sector of the North Sea showed that the SAG process was employed without any major problem, while the co-injection process was hindered by operational problems that resulted in unstable injectivity (Farajzadeh, 2009).

Despite the advantages of the SAG process over the co-injection method, it is pertinent to note that the key factor for the success of a SAG process will depend on several factors such as the type of porous medium, surfactant type or choice with respect to the gas injected, physical and chemical properties of the fluids in the porous medium, etc. According to Huh and Handy (1989), in the presence of oil and at high temperatures and pressures, a properly selected surfactant should be able to generate a substantial amount of stable foam in the reservoir rock. Furthermore, surfactant adsorption on the rock should be as low as possible, as a higher surfactant adsorption causes a decrease in the surfactant concentration, thereby limiting how far the surfactant can propagate into the reservoir before its concentration will become too low for proper or effective generation of foam. According to Zhou and Rossen (1995) and Myers and Radke (2000), the major concern of SAG (foam) application as an EOR method is that when foam comes into contact with crude oil, its longevity is reduced. Several experiments including Huh and Handy (1989) and Andrianov et al. (2012) in both bulk and porous media have shown the adverse effect of oil on foam stability. Thus, in the absence of oil, foam may behave differently compared to how foam will behave in the presence of oil. The presence of oil could impact on the performance of foam in a porous medium by affecting lamellae stability, particularly as the stability of foam in porous media largely depends on how stable the foam films are in the medium (Simjoo et al., 2013). This was corroborated by the study of Almajid and Kovscek (2016). In their study on foam generation and

coalescence in the presence of oil, the authors stated that in the presence of oil, the successful formation of a lamella following snap-off near a pore throat is hindered, thereby having a negative effect on foam stability. This, the authors called "hindered generation". Through several coreflooding experiments, Schramm (1994) showed that at oil saturations above 5% to 20%, oil can have an adverse effect on foam.

Another factor that could affect the field application of foam is the wettability of the rock. Foams are not expected to be stable in porous media that are not strongly water-wet. This is because a lamella is in a high-energy state stretched across a pore body. As such, due to its surface area, if the pore wall were energetically indifferent to contact with the surfactant solution, the lamella would presumably detach and collapse. In the study of Sanchez and Hazlett (1992), it was found that in the absence of oil, surfactant solution reversed the wettability of oil-wet bead packs and stabilised foam. Other studies including Suffridge et al. (1989), Prieditis and Paulett (1992) and Kuehne et al. (1990) have also been able to create weak foams (defined in more detail later) in oil-wet rocks even in the presence of oil. However, Rossen (1996) states that, since it is impractical to displace or strip oil completely from oil-wet reservoirs, even near an injector, it would appear that foams are at best less effective in these reservoirs. Be that as it may, Lescure and Claridge (1986) found out in their experimental study of CO_2 foam flooding that on a water-wet rock, the adsorption of surfactant is likely to be greater than on an oil-wet rock. This can significantly reduce the efficiency of CO_2 foam mobility control. In addition, the authors stated that in a water-wet system, there could be faster coalescence of CO_2 bubbles. To avoid this, the amount of surfactant in the liquid phase can be increased. However, doing this can lead to the formation of micro-emulsions or rigid foams that could end up blocking the CO_2 flow pathway altogether, thereby preventing the efficient sweeping

of the region ahead of the foam. In conclusion though, Lescure and Claridge (1986), stated that foam flooding by CO_2 foam mobility control can be carried out successfully in both partially oil-wet and water-wet medium. Other factors affecting foam application in porous media has been reviewed by Farzaneh and Sohrabi (2013). For this present study, we are focussed on the interaction between gas and (surfactant) liquid during SAG processes, so we do not treat the oil explicitly as being a distinct phase. Instead oil, if present, is considered as part of the liquid phase, which can consist of both surfactant liquid and reservoir liquids. So the system can be partially oil-wet or still assumed to be a water-wet system without affecting the model we develop.

In summary, before carrying out a field application of foam, the field and its sweep efficiency problem must be characterised. In doing this, questions asked should include the following: Is there sufficient residual oil remaining to make a foam process economical? What causes the poor sweep efficiency observed: e.g. a thief zone (i.e. a thin, very high permeability layer), gravity override, fractures in the reservoir, etc.? Is injection pressure-limited? What levels of surfactant losses would be expected due to adsorption and residual oil, given the type of formation? Is the reservoir water-wet or oil-wet or mixed? Once the above questions have been answered and it is believed that there is oil that can be targeted effectively, and the process looks feasible, another issue that has to be considered is surfactant choice. To guide the choice of surfactant in the midst of several possible surfactant formulations, a simple wet-chemistry test for precipitation in reservoir brine, surfactant solubility in reservoir oil, and thermal stability at reservoir temperatures can then be used (Rossen, 1996). Having thereby selected the particular foam IOR process to be employed, we want to predict how the foam will behave in the reservoir: this is discussed in the next section.

2.4 Foam flow modelling in porous media

When choosing foam or foam displacement as an IOR method, the behaviour of foam in porous media has to be properly understood. According to Khatib et al. (1986), Falls et al. (1989) and Ettinger and Radke (1992), the behaviour of foams in porous media depends on bubble size, or foam texture which is defined by the number of foam thin films per unit volume of the porous medium. Falls et al. (1989) stated that the foam texture is in turn dependent on certain factors including capillary pressure, properties of the reservoir rock, surfactant type and concentration. From the study of Khatib et al. (1986), and Falls et al. (1988), it was discovered that higher capillary pressure could lead to foam collapse while lower capillary pressure favours foam generation and stability. Zhou and Rossen (1995), and Shan and Rossen (2004) also agreed with this.

Several methods exist for modelling the transport or displacement of foam in porous media. Three major approaches including mechanistic, empirical and semi-empirical methods are normally used (Kovscek and Radke, 1993b; Zhang et al., 2009).
A specific example of the mechanistic approach is the bubble population balance model (discussed later (Kovscek and Radke, 1993b, 1994; Shi, 1996; Zhang et al., 2009)). The empirical methods include the mobility reduction approach, the effective viscosity approach, the fixed limiting capillary pressure model, the pressure-driven growth model etc. (Kovscek and Radke, 1993b, 1994; Zhang et al., 2009; Shan and Rossen, 2004; Grassia et al., 2014). A typical example of the semi-empirical model is the fractional flow model (Dholkawala et al., 2007). This model is important to some of the empirical models (like the pressure–driven growth model (Shan and Rossen, 2004; Grassia et al., 2014)) since, as stated previously, the pressure-driven growth model relies on data from the fractional

flow model. Some of these models are discussed below.

2.4.1 Empirical models

The empirical models of foam usually deal with the alteration of gas mobility or gas viscosity in the presence of foam, either based on some hypothesis and/or field observations, conjecture or experiments. Gas mobility is then expressed empirically as a function of flow rates and/or surfactant concentration without any explicit reference to foam texture. Some specific examples of the empirical models are considered below.

2.4.1.1 Mobility reduction model

This method uses a relative permeability approach to include the effect of foam in a simulator by using a constant mobility reduction factor (MRF), commonly used in describing foam rheology in a local steady-state modelling (Ding et al., 2020). For the same water saturation, the mobility reduction factor is conceptually defined as:

$$MRF = \frac{\Delta P_{withfoam}}{\Delta P_{withoutfoam}} \tag{2.1}$$

or, alternatively

$$MRF = \frac{\Delta P_{withfoam} - \Delta P_{withoutfoam}}{\Delta P_{withoutfoam}} \tag{2.2}$$

where ΔP is the pressure drop across the porous medium. Based on the respective definitions above, a mobility reduction factor MRF value of unity (1) or zero (0) usually indicates that the injected foam is completely destroyed and the flow is equivalent to a typical two-phase flow of gas and liquid without foam. However, when the foam is finely textured and hence considered to be stronger, higher values of the MRF result (Kovscek,

1998). In other words, a very strong foam will give a very large value of MRF, while a weak foam will give a smaller value of MRF. In a chemical flood simulator (UTCHEM) developed by the University of Texas at Austin, a MRF has been incorporated empirically into the simulator (Delshad et al., 2000). In this simulator, a constant value is used to divide the gas permeability as shown below.

$$k_{rf} = \frac{k_{rg}(S_g)}{1 + MRF} \tag{2.3}$$

where S_g here denotes gas saturation. In this model, before the gas mobility is modified, a threshold surfactant concentration has to be exceeded. Due to the dynamic nature of permeability reduction, since it varies with gas velocity and surfactant concentration, there is a weakness in employing a constant mobility reduction factor MRF.

An alternative way of using the MRF approach is to carry out a tabulation of MRF values as a function of gas velocity, surfactant concentration, oil saturation and often also water saturation (or equivalently capillary pressure that depends on saturation). This approach was applied to the ECLIPSE 200 simulator (Kovscek, 1998). According to various authors including Kular et al. (1989), Mohammadi and Coombe (1992) and Mohammadi et al. (1995), in the STARS simulator, the gas mobility reduction factor MRF of foam is usually treated to be dependent on surfactant concentration, oil saturation, and gas velocity. It is mathematically represented as:

$$MRF = M\left(\frac{C_s}{C_s^{max}}\right)^{e_s}\left(\frac{S_o^{max} - S_o}{S_o^{max}}\right)^{e_o}\left(\frac{N_c}{N_c^{max}}\right)^{e_v} \text{ with } e_v < 0 \tag{2.4}$$

where C_s is the concentration of surfactant in the aqueous phase, S_o is the oil saturation,

e (with subscripts) are exponents, superscript max is the reference or maximum values of variables, M sets the scale of the mobility reduction, and N_c is capillary number, mathematically expressed as:

$$N_c = \frac{\mu v}{\sigma} \tag{2.5}$$

where μ is the viscosity of the displacing fluid, v is the Darcy or superficial velocity (for convenience, written here as if the flow is still monophasic). In single phase or monophasic flow, the superficial velocity is equal to the mean velocity of the fluid), and σ is the gas/liquid interfacial tension. Owing to Darcy's law which relates μv to $k\nabla P$, this can also be written as:

$$N_c = \frac{k\nabla p}{\sigma} \tag{2.6}$$

This definition is useful since in oil field applications, the pressure difference (and hence average pressure gradient) that is applied is generally known, even if details of the flow field are not known.

Note that the impacts of liquid velocity and capillary pressure on MRF have not been accounted for in equation (2.4), except to the extent that capillary number itself as defined by equation (2.6) influences velocity. According to Kular et al. (1989), there is no additional explicit velocity dependence on mobility reduction as long as surfactant is present and capillary pressure is low, as gas mobility remains small via a reduced gas relative permeability. This empirical approach is also used in the UTCOMP simulator developed at the University of Texas at Austin (Chang, 1990; Shi, 1996; Chang and Grigg, 1996).

2.4.1.2 Effective viscosity model

This empirical method of modelling foam in porous media simply involves the modification of the gas phase relative permeability using the effective viscosity of the gas phase, thereby reducing gas phase mobility in the presence of foam. Marfoe et al. (1987) mathematically expressed the effective viscosity in the presence of foam μ_s as a function of surfactant concentration, C_s (measured here in ppm), aqueous phase saturation S_w, effective viscosity of the gas μ_g, and gas-phase velocity v_g, and f is a function to be specified:

$$\mu_f = \mu_g\Big[1 + 0.01C_s(S_w - S_{wr})f(v_g)\Big] \tag{2.7}$$

where S_{wr} represents the residual aqueous saturation.

According to Marfoe et al. (1987), the constant 0.01 in equation (2.7) gives a five–to ten–fold increase in gas viscosity over surfactant concentrations of 0–1000 ppm (i.e. initial in-place surfactant concentration to surfactant concentration in a foam driven system). If greater reduced mobility is expected in a given system, a larger value of this prefactor can be used. Marfoe et al. (1987) set the value of $f(v_g)$ to 1, thereby eliminating any v_g dependence in equation (2.7). A more complex effective viscosity function including permeability and oil saturation was implemented by Islam and Ali (1990). This they expressed as:

$$\mu_f = \mu_g\frac{1 + D(S_w - S_{wr})f_c f_k + f_p}{1 + ES_o^2} \tag{2.8}$$

where f_c, f_p and f_k are functions of surfactant concentration, pressure gradient and

permeability, respectively, and D and E are parameters. The oil saturation S_o is also technically constant since it is assumed that the surfactant does not partition into the oil phase or that the relative permeability of the oil phase does not change in the presence of surfactant or foam. The f_c, f_p and f_k functions are normally determined by experimental observations and history matching– that is adjusting key properties of a reservoir model, say historical production data and pressures by trial and error until they closely match or fit the historic or field data (Islam and Ali, 1990).

2.4.1.3 Fixed limiting capillary pressure model

The basic idea of the fixed limiting capillary pressure model is that at a certain limiting capillary pressure (corresponding to a certain limiting liquid saturation) the mobility of the gas undergoes a dramatic change (Rossen and Zhou, 1995; Zhou and Rossen, 1995). For liquid saturations immediately below this limiting saturation, the foam collapses, meaning that gas mobility becomes high. For liquid saturations immediately above the limiting saturation though, foam survives and this causes the gas mobility to reduce suddenly and dramatically by some mobility reduction factor MRF. This model will be revisited in section 2.4.3.2.

2.4.1.4 Pressure-driven growth model

The pressure-driven growth model is simply based on the idea that the lowest overall mobility of fluids (gas and liquid together) happens around the limiting saturation mentioned above, and the total mobility at (or immediately above) this saturation is much lower than anywhere else in the flow (Shan and Rossen, 2004; Grassia et al., 2014). This means most of the pressure drop driving the flow is incurred in this low mobility region. The pressure-driven growth model is an idealisation in the limit that the entire pressure

drop happens in this region, with the rest of the domain having arbitrarily high mobility by comparison. The implication is that we only need to track the motion of the low mobility front at or near the limiting saturation, not the entire flow domain.

Having reviewed empirical models, in the next section we move onto the semi-empirical approach.

2.4.2 Semi-empirical model

The semi-empirical model most widely-used to study foam displacement is the fractional flow model (Dholkawala et al., 2007). Here, the physics of foam is mechanistically described, but then simplifying assumptions are used to develop fractional flow curves that account for the presence of foam. The fractional flow theory is explained in detail below.

2.4.2.1 Fractional flow theory

The fractional flow model is considered as a semi-empirical method because of the simplified assumptions that are generally imposed including Newtonian viscosity, one dimensional displacement, negligible gravitational impact, no physical dispersion, incompressible phases, no viscous fingering, no capillary-pressure gradients, and immediate attainment of local steady state for the bubble population (Sheng, 2011). Solutions to the fractional flow model can however still capture more complex displacement mechanisms by relaxing many of the above assumptions to some extent (Dholkawala et al., 2007). In the fractional flow model, the physics of miscible and immiscible displacements in porous media are described, and then the governing partial differential equations are solved analytically by a mathematical technique called the method of characteristics (Zanganeh et al., 2011). The Method of Characteristics (MOC) is a mathematical tool that can be

used (amongst many other applications) to analyse miscible and immiscible displacement processes in porous media by converting the governing material balance partial differential (PDE) equations into a series of ordinary differential equations (ODE), resulting in solutions that are in the form of wave propagation through the system as a function of time and space.

Buckley and Leverett (1942) first presented and solved the theory by constructing fractional flow curves theoretically by plotting water fractional flow or water cut (f_w) against water saturation (S_w). A number of studies have since then further developed the theory to account for a wide range of applications in oil recovery. Several authors including Buckley and Leverett (1942), Dake (1978), Pope (1980), Zhou and Rossen (1995), Dholkawala et al. (2007) etc. have presented fractional flow solutions for foam applications. The original fractional flow model by Buckley and Leverett (1942) (originally for oil and water) is introduced below before presenting the fractional flow models for foam which are discussed subsequently.

2.4.2.2 Assumptions and derivation of the fractional flow theory

Buckley and Leverett (1942) used the fractional-flow theory to study how an immiscible fluid-fluid displacement advances through a reservoir. They achieved this through the estimation of the rate at which an injected water bank migrates through a porous medium containing oil. Even though the study of Buckley Buckley and Leverett (1942) was based on a 1-D reservoir and an water-oil system (that is oil being the displaced fluid, while water is the displacing fluid), a proper understanding of this theory can help in extending the model to 2-D and 3-D reservoirs and also other systems including a system of gas-oil, gas-oil-water, foamed gas-water, etc. The Buckley-Leverett theory in its original form

had the following assumptions:

- The fluids in the reservoir (that is, oil and water) are incompressible, immiscible and flow through a homogeneous reservoir.
- The flow is linear (that is unidirectional) and horizontal with constant cross-sectional area and constant reservoir length.
- Water is the fluid injected into an oil reservoir. In other words, the initial conditions state that the reservoir will be oil-filled and the boundary conditions consist of water being injected at one end and oil produced at the other end.
- Capillary pressure and gravity effects are negligible. It is worthy of mention here that it is safe to neglect capillary gradient as long as the aqueous saturation is comparatively high and the capillary gradient is small. This is not the case when aqueous saturations are lower – e.g. only slightly greater than the critical water saturation S_{wcr} for produced water to appear at all (Zhang et al., 2009). From a petroleum engineering point of view, the critical water saturation for produced water to appear is slightly different from the connate water saturation and the irreducible water saturation (both defined in section 2.4.3.2). According to Harris Jr (1992), the critical water saturation is basically the maximum water saturation that a formation with a given permeability and porosity can retain without producing water. In other words, it defines a range in saturation (usually slightly below the connate water saturation but above the irreducible water saturation— defined later in section 2.4.3.2) before water will begin to flow in a reservoir.

The derivation done here follows the work of Tarek (2006) by considering the steady–state flow of two immiscible fluids (oil and water) through a tilted–rectilinear porous medium

as shown in figure 2.9.

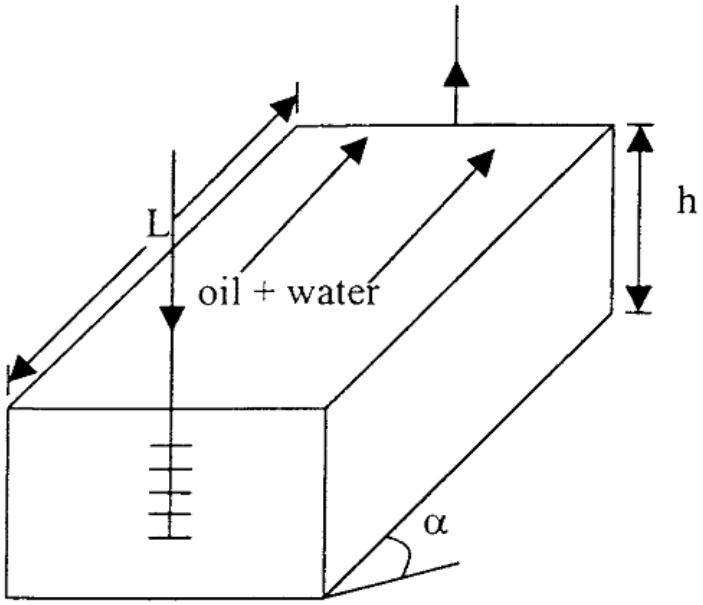

Figure 2.9: Schematic representation of oil displacement by water in a tilted-rectilinear reservoir system (Tarek, 2006).

Supposing the system is homogeneous, then Darcy's law can be applied for each fluid (oil and water) as shown below.

$$q_o = \frac{-k_o A}{\mu_o}\left[\frac{\partial P_o}{\partial x} + g\rho_o \sin(\alpha)\right] \tag{2.9}$$

$$q_w = \frac{-k_w A}{\mu_w}\left[\frac{\partial P_w}{\partial x} + g\rho_w \sin(\alpha)\right] \tag{2.10}$$

where:

q_o = oil flow rate

q_w = water flow rate

k_o = effective permeability of oil

k_w = effective permeability of water

μ_o = viscosity of oil

μ_w = viscosity of water

P_o = oil pressure

P_w = water pressure

ρ_o = density of oil

ρ_w = density of water

x = distance

A = cross-sectional area

α = dip angle; $\sin(\alpha)$ is negative for down-dip flow and positive for up-dip flow.

Rearranging equation (2.9) and (2.10) yields:

$$\frac{q_o \mu_o}{A k_o} = -\frac{\partial P_o}{\partial x} - g\rho_o \sin(\alpha) \tag{2.11}$$

$$\frac{q_w \mu_w}{A k_w} = -\frac{\partial P_w}{\partial x} - g\rho_w \sin(\alpha) \tag{2.12}$$

Subtracting the equations above yields:

$$\frac{q_w \mu_w}{A k_w} - \frac{q_o \mu_o}{A k_o} = \left(\frac{\partial P_o}{\partial x} - \frac{\partial P_w}{\partial x}\right) - g(\rho_w - \rho_o)\sin\alpha \tag{2.13}$$

However, the capillary pressure (P_c) in a system of oil and water can simply be expressed as:

$$P_c = P_o - P_w \tag{2.14}$$

Differentiating equation (2.14) with respect to the distance (x)

$$\frac{\partial P_c}{\partial x} = \frac{\partial P_o}{\partial x} - \frac{\partial P_w}{\partial x} \tag{2.15}$$

Substituting equation (2.15) into equation (2.13) gives

$$\frac{q_w \mu_w}{A k_w} - \frac{q_o \mu_o}{A k_o} = \frac{\partial P_c}{\partial x} - g \Delta \rho \sin(\alpha) \tag{2.16}$$

where $\Delta\rho = \rho_w - \rho_o$ is a density difference. The fractional flow of water (f_w) for two immiscible fluids (oil and water) is defined as the flow rate of water divided by the total flow rate (q_t) expressed as:

$$f_w = \frac{q_w}{q_t} = \frac{q_w}{q_w + q_o} \tag{2.17}$$

From equation (2.17):

$$q_o = (1 - f_w) q_t; \;\; q_w = f_w q_t \tag{2.18}$$

Thus, replacing q_o and q_w in equation (2.16) with equations (2.17) and (2.18):

$$f_w = \frac{1 + \left(\frac{k_o A}{\mu_o q_t}\right)\left[\frac{\partial P_c}{\partial x} - g \Delta \rho \sin \alpha\right]}{1 + \left(\frac{k_o \mu_w}{k_w \mu_o}\right)} \tag{2.19}$$

where:

f_w = fractional flow of water

q_t = total flow rate

A = cross-sectional area

$\Delta\rho$ = water-oil density difference

Other parameters are as defined before.

Neglecting the capillary pressure, equation (2.19) can be written as:

$$f_w = \frac{1 + \left(\frac{k_o A}{\mu_o q_t}\right)\left[g\Delta\rho \sin\alpha\right]}{1 + \left(\frac{k_o \mu_w}{k_w \mu_o}\right)} \tag{2.20}$$

Assuming as per Buckley and Leverett (1942) that water (rather than a mixture of water and gas) is injected, then for two-phase flow, the total flow rate q_t is equal to the water injection rate i_w (that is $i_w = q_t$). Also, relative permeability ratios equal effective permeability ratios (i.e. $k_{ro}/k_{rw} = k_o/k_w$), therefore, equation (2.20) can be written as:

$$f_w = \frac{1 + \left(\frac{k k_{ro} A}{\mu_o i_w}\right)\left[g\Delta\rho \sin\alpha\right]}{1 + \left(\frac{k_{ro} \mu_w}{k_{rw} \mu_o}\right)} \tag{2.21}$$

where k is the absolute permeability (that is, permeability measured in a single phase flow), and is related to the relative permeability (k_{ri}) and effective permeability (k_i) of a phase by $k_{ri} = k_i/k$ (subscript i represent either of the phases; oil or water).

For a reservoir that is horizontal (that is $\sin\alpha = 0$), it is seen that the injection rate will have no effect on the fractional flow. In that case, neglecting the effects of gravity, therefore, equation (2.21) can be simplified to:

$$f_w(S_w) = \frac{1}{1 + \frac{k_{ro}(S_w)\mu_w}{k_{rw}(S_w)\mu_o}} = \left(1 + \frac{\lambda_{ro}(S_w)}{\lambda_{rw}(S_w)}\right)^{-1} \tag{2.22}$$

where λ_{ro} and λ_{rw} denote relative mobilities (ratios between relative permeability and viscosity).

In a **water-gas system** (i.e. two phase flow of water and gas), the fractional flow

equation can be expressed similarly as:

$$f_w(S_w) = \frac{1}{1 + \frac{k_{rg}(S_w)\mu_w}{k_{rw}(S_w)\mu_g}} = \left(1 + \frac{\lambda_{rg}(S_w)}{\lambda_{rw}(S_w)}\right)^{-1} \tag{2.23}$$

The relative permeability functions are normally given by Corey's semi-empirical relations given in (Corey, 1954; Corey et al., 1956; Brooks and Corey, 1964) as:

$$k_{rw}(S_w) = k^o_{rw}\left[\frac{S_w - S_{wr}}{1 - S_{wr} - S_{gr}}\right]^{n_w} = k^o_{rw}S^{n_w} \qquad S_{wr} \leq S_w \leq 1 - S_{gr} \tag{2.24}$$

where S has been defined as $S = (S_w - S_{wr})/(1 - S_{wr} - S_{gr})$ and

$$k_{rg} = k^o_{rg}\left[\frac{1 - S_w - S_{gr}}{1 - S_{wr} - S_{gr}}\right]^{n_g} = k_{rg} = k^o_{rg}(1 - S)^{n_g} \qquad S_{gr} \leq S_g \leq 1 - S_{wr} \tag{2.25}$$

where S_w is the water saturation, S_{wr} is the residual water saturation (i.e. the water saturation achieved after an infinite number of pore volumes of displacing gas have flowed through a particular portion of reservoir rock), and S_{gr} is the residual gas saturation (i.e. the gas saturation achieved after an infinite number of pore volumes of displacing water have flowed through a particular portion of the porous medium). Meanwhile k^o_{rw} and k^o_{rg} are end point relative permeabilities (that is the relative permeability of a phase at the irreducible saturation of the other phase). The end point relative permeability values are sensitive to the wettability of the rock with the fluids in question (Honarpour et al., 1982). Also n_w and n_g are exponents of the relative permeability curves.

In the form that equation (2.23) is given, parametrically, the fractional flow curve depends on n_w, n_g and M^o, where M^o is the end point mobility ratio simply defined as the ratio

of the mobility of the displacing fluid to the mobility of the displaced fluid at various end point phase saturations. For gas displacing water or aqueous surfactant (i.e. a foamed-gas system), it is mathematically given as:

$$M^o = \frac{\lambda^o_{rg}}{\lambda^o_{rw}} \tag{2.26}$$

where λ^o_{rg} is endpoint relative mobility of gas and λ^o_{rw} is endpoint relative mobility of water, so that:

$$f_w = (1 + M^o(1 - S)^{n_g}/S^{n_w})^{-1} \tag{2.27}$$

There are other forms of mobility ratio also (Debbabi et al., 2017; Farajzadeh et al., 2019), viz. average mobility ratio ($\overline{M}$) which uses the average water saturation upstream of the displacement front ($\overline{S_w}$) relative to the mobility just downstream of it, and the shock-front mobility ratio (M_{sf}) which uses saturations upstream and downstream of the displacement front. They are both given as:

$$\overline{M} = \frac{\lambda_{rt}^{\overline{S_w}}}{\lambda_{rt}^-}; \qquad M_{sf} = \frac{\lambda_{rt}^+}{\lambda_{rt}^-} \tag{2.28}$$

where superscripts $^+$ and $^-$ represent upstream and downstream of the displacement front respectively. Here, λ_{rt} represents the total relative mobility (that is weighted sum of the relative mobilities of each phase at a given water saturation). A mobility ratio (upstream to downstream) of unity or less normally indicates a favourable or stable displacement process. Mobility here simply describes the ability of a phase to move through a permeable media when under the influence of a pressure gradient. Mathematically, as we have

seen, mobility is the quotient between phase permeability (or effective permeability), and phase viscosity. According to Lake (1989), more than just relative permeability, the mobilities are perhaps the most important factor in any injection based improved oil recovery process that determines how one fluid displaces another. When the mobility ratio (upstream to downstream) is high, it means that the displaced fluid is less mobile than the displacing phase; thus, there is the tendency of the displacing fluid to finger through the displaced phase as a result of viscous instabilities. Therefore, in improved oil recovery, a low mobility ratio equates to an improvement in displacement efficiency, vertical sweep efficiency, and areal sweep efficiency.

A typical fractional flow curve is shown in figure 2.10.

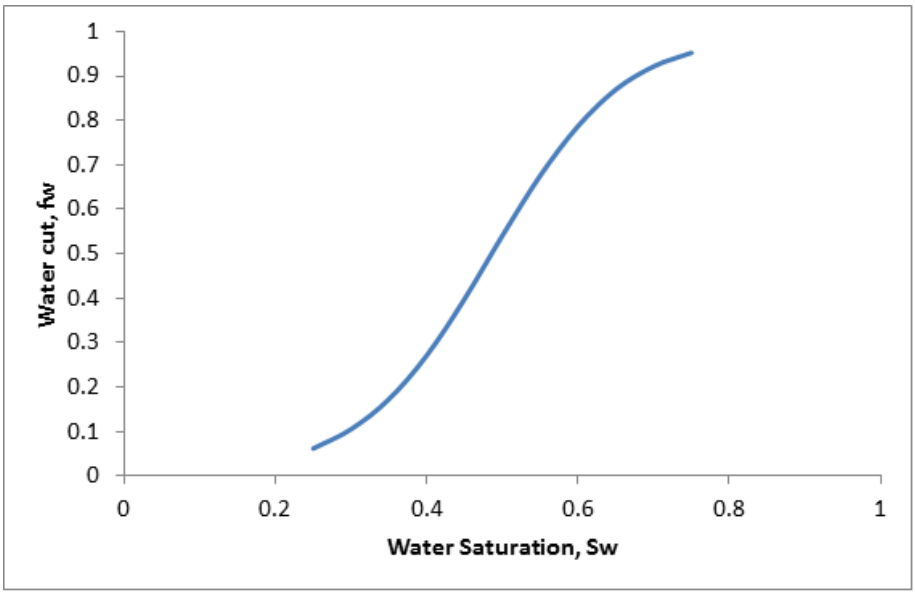

Figure 2.10: Typical fractional flow curve from the data of (Tarek, 2006). This fractional flow curve is for a water-oil system.

In the S-shaped curve above, there is an inflection point which varies with M^o. Indeed, it follows from equation (2.26) for gas displacing water, that small M^o (displacing mobility to displaced mobility) gives larger f_w (which now equals $k'_{rw}(S_w)/(k'_{rw}(S_w) + M^o k'_{rg}(S_w))$) even for modest S_w values. Here, we have defined $k'_{rg} = k_{rg}/k^o_{rg}$ and $k'_{rw} = k_{rw}/k^o_{rw}$. On the other hand, in the case of water displacing oil, we have $f_w =$

$M^o k_{rw}(S_w)/(M^o k_{rw}(S_w) + k_{ro}(S_w))$. So, high M^o (displacing mobility to displaced mobility) now gives high f_w. Generally, at favourable mobility ratios (usually $M^o \leq 1$), the fluid's injectivity declines whereas the sweep efficiency increases, while at unfavourable mobility ratios ($M^o > 1$), the fluid's injectivity increases albeit with decreasing sweep efficiency (Tarek, 2006). The injectivity of a fluid is simply the rate of the fluid's injection divided by the pressure differential between the injection well and the production well (Satter and Iqbal, 2016).

According to Tarek (2006), the phase viscosities and endpoint relative permeabilities also have a strong effect on the fractional flow curve. In foam improved oil recovery, the foam's relative mobility replaces the gas relative mobility used in a conventional gas displacement process as in:

$$f_w(S_w) = \left(1 + \frac{\lambda^f_{rg}(S_w)}{\lambda_{rw}(S_w)}\right)^{-1} \tag{2.29}$$

where as before, the λ values denote relative mobilities.

The gas relative mobility λ^f_{rg} in the presence of foam is usually modelled as a reduction in the gas phase relative permeability. One of the common foam mobility models is the one used in STARS software by the Computer Modelling Group (Computer Modeling Group, 2006). The model uses a foam mobility-reduction factor (often denoted FM, but defined in such a fashion as to scale inversely with the mobility reduction factor MRF identified earlier in the context of empirical modelling) to capture the reduction in the relative permeability of gas in the presence of surfactant. The foam mobility-reduction factor (FM) simply represents a dimensionless factor by which the gas relative permeability is reduced due to the presence of foam, relative to the gas relative permeability at the same

liquid or water saturation when foam is not present. Mathematically, the foam's relative permeability is defined by:

$$k_{rg}^{f}(S_w) = FM\, k_{rg}(S_w) \tag{2.30}$$

where the foam mobility-reduction factor (FM) is given as:

$$FM = \frac{1}{1 + f\text{mmob}\, F_1 F_2 F_3 F_4 F_5 F_6} \qquad 0 \leq F_i \leq 1 \tag{2.31}$$

The parameter $fmmob$ represent a reference mobility reduction factor which corresponds to the maximum gas mobility reduction a foam formulation can achieve. Six dimensionless coefficients F_i are normally used to scale $fmmob$. They are (F_1) which represents the effect of surfactant concentration on foam behaviour, (F_2) which represents the effect of water saturation, (F_3) which represents the effect of oil saturation, (F_4) which is a shear-thinning function, the effect of capillary number (F_5), and the effect of salinity (F_6) respectively. The F_2 function which represents the effect of water saturation on foam mobility is what is relevant in this study; albeit via mathematical modelling approach rather than a simulation as in STARS. The details of the other functions are beyond the scope of this study, but can be found in literature including Computer Modeling Group (2006) and Farajzadeh et al. (2012b). It is important to consider this function (F_2) when modelling the behaviour, particularly in the high quality (i.e. low f_w and hence low S_w) regime. This is because, in a surfactant alternating gas (SAG) injection process, a major part of the reservoir (to be specific, the near-wellbore region) operates in the high quality foam region (i.e. low S_w). This makes this assumption appropriate. Thus, in the framework of this study, the foam mobility-reduction factor (FM) is reduced to a

function of S_w only in the form:

$$FM(S_w) = \frac{1}{1 + f\text{mmob}\, F_2(S_w)} \tag{2.32}$$

In the STARS model, F_2 is given as:

$$F_2(S_w) = 0.5 + \frac{\arctan[epdry(S_w - fmdry)]}{\pi} \tag{2.33}$$

where $fmdry$ refers to the water or liquid saturation at which foam collapses and mobility reduction decreases remarkably. Meanwhile *epdry* is a factor that controls how abruptly the foam collapses at $fmdry$. Smaller values of *epdry* result in a more gradual transition, while large values result in an abruptly almost discontinuous transition between the two regimes. However, in that case, the limit at $S_w = 0$ does not yield $F_2 = 0$.

Recall that equation (2.22) corresponds to the original fractional flow theory (for water-oil displacements) and equation (2.23) is the gas-water displacement analogue. The primary use of these equations is so that provided the water saturation at any point in a reservoir is already known, then the water fractional flow or water cut (f_w) can be determined at that point. Water cut is simply defined as the ratio of the water flow rate to the total liquid flow rate. Using equations (2.22) (water-oil displacements) and (2.23) (gas-water displacements) through their dependence on water saturation only, the water fractional flow can be deduced as a function of position and time provided the water saturation is itself known. Therefore, it is relevant to determine the water saturation at any given position and given time during a displacement process.

The fractional-flow equation on its own cannot determine the water saturation at any

particular point in a reservoir at any particular time. To address this issue, Buckley and Leverett (1942) needed to develop another equation that enables the water saturation at any given time during the displacement of oil by water to be determined. The equation was developed by considering a material balance on the displacing fluid (i.e. water in the case considered by Buckley and Leverett (1942)) in a porous medium. Buckley and Leverett (1942) considered and carried out a material balance analysis on a differential element of a porous medium with differential time (dt), differential length (dx), area (A) and porosity (ϕ). This is shown in figure 2.11.

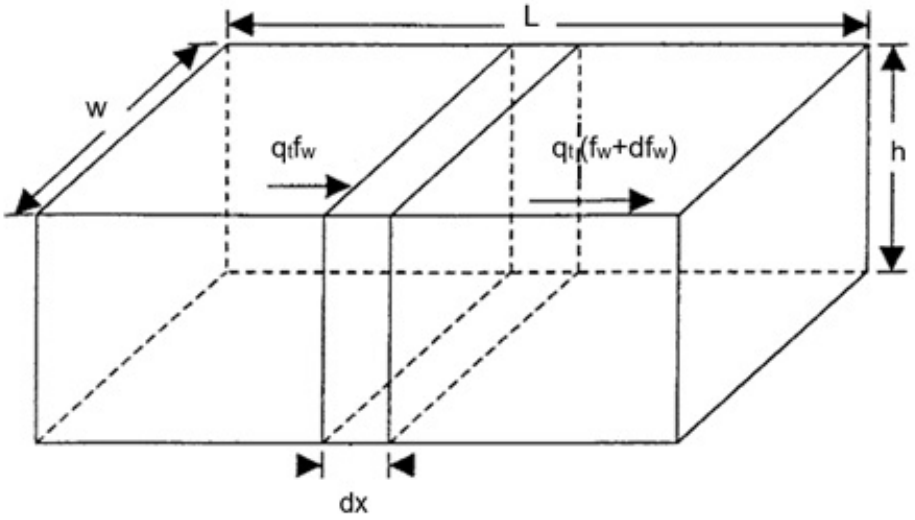

Figure 2.11: Water flow through a rectilinear differential element (Tarek, 2006).

Over a differential time period (dt), the total volume of water that enters and leaves the porous medium per cross-sectional area can be expressed as:

$$\text{volume of water entering the medium} = q_t f_w \mathrm{d}t \tag{2.34}$$

$$\text{volume of water leaving the medium} = q_t(f_w + \mathrm{d}f_w)\mathrm{d}t \tag{2.35}$$

where q_t is a total fluid flux. Subtracting equation (2.34) from equation (2.35) will give the volume of water accumulated within the medium in terms of the differential changes

of the saturation $\mathrm{d}f_w$ as:

$$q_t f_w \mathrm{d}t - q_t(f_w + \mathrm{d}f_w)\mathrm{d}t = -q_t \mathrm{d}f_w \, \mathrm{d}t \tag{2.36}$$

Let S_w be the water saturation at time 't'. Then, let us write $\mathrm{d}S_w$ as the change in water saturation between t and $t + \mathrm{d}t$. Therefore, the accumulation of water in the medium (in the slice $[x, x + \mathrm{d}x]$) per unit cross section will be:

$$\mathrm{d}(S_w \phi)\mathrm{d}x \tag{2.37}$$

where ϕ is porosity.

Equating (2.36) and (2.37)

$$\mathrm{d}(S_w \phi)\mathrm{d}x = -q_t \mathrm{d}f_w \mathrm{d}t \tag{2.38}$$

We now take the limit as $\mathrm{d}t \longrightarrow 0$, and $\mathrm{d}x \longrightarrow 0$; and also recall $q_w = f_w q_t$.

With constant porosity ϕ, equation (2.38) reduces to:

$$\frac{\partial S_w}{\partial t}\phi + \frac{\partial f_w}{\partial x} q_t = 0 \tag{2.39}$$

As stated before, fractional flow is a function of position and time through its dependence on water saturation only. Thus, in terms of a total derivative with respect to water saturation, the chain rule can be applied to expand the f_w partial derivative. With that, equation (2.39) becomes:

$$\frac{\partial S_w}{\partial t}\phi + q_t \frac{\mathrm{d}f_w}{\mathrm{d}S_w}\frac{\partial S_w}{\partial x} = 0 \tag{2.40}$$

Equation (2.39) is known as the Buckley-Leverett equation.

In dimensionless form, equation (2.40) can be expressed as:

$$\frac{\partial S_w}{\partial t_D} + \frac{\mathrm{d}f_w}{\mathrm{d}S_w}\frac{\partial S_w}{\partial x_D} = 0 \tag{2.41}$$

This dimensionless equation is obtained as follows. The derivative of dimensionless distance (x_D) with respect to physical distance here is:

$$\frac{\mathrm{d}x_D}{\mathrm{d}x} = \frac{1}{L} \tag{2.42}$$

where L is some length scale of interest. Meanwhile with respect to physical time, the derivative of dimensionless time (t_D) is:

$$\frac{\mathrm{d}t_D}{\mathrm{d}t} = \frac{q_t}{\phi L} \tag{2.43}$$

The dimensionless Buckley-Leverett equation (2.41) then results.

Therefore, the problem will be to find solutions $S_w(x_D, t_D)$ subject to the governing equation and the initial and boundary conditions:

$$S_w(x_D, 0) = S_{wI}, \qquad x_D \geq 0 \tag{2.44}$$

and

$$S_w(0, t_D) = S_{wJ}, \qquad t_D \geq 0 \tag{2.45}$$

where subscripts $_I$ and $_J$ represent initial and injection conditions respectively. These equations are general enough to cover both water injection into oil and gas injection into water.

Equation (2.41) shows a first order prototypical hyperbolic partial differential equation (PDE) with variable coefficients (Castillo et al., 2020). It represent a straightforward or one-way wave equation with saturations travelling with a finite speed of propagation from injection point to the producer. To obtain a solution, information downstream of the wave is usually not needed, hence it is generally known as an initial value problem. Saturation depends only on dimensionless position and time, i.e. $S_w = S_w(x_D, t_D)$. Indeed, equation (2.41) can be solved, as mentioned earlier, using a mathematical technique called the method of characteristics– MOC (Zanganeh et al., 2011; Wang et al., 2015). The partial differential equation is reduced to an ordinary differential equation(ODE) along a characteristic (a line of constant water saturation in the (t, x) plane), and then the solution can be integrated from some initial condition. The total derivative dS_w can be written as:

$$\mathrm{d}S_w(t_D, x_D) = \left(\frac{\partial S_w}{\partial t_D}\right)_{x_D} \mathrm{d}t_D + \left(\frac{\partial S_w}{\partial x_D}\right)_{t_D} \mathrm{d}x_D \tag{2.46}$$

At constant saturation $\mathrm{d}S_w = 0$. Rearranging equation 2.46 yields:

$$\left(\frac{\mathrm{d}x_D}{\mathrm{d}t_D}\right)_{dS_w=0} = -\left(\frac{\partial S_w}{\partial t_D}\right)_{x_D} \Bigg/ \left(\frac{\partial S_w}{\partial x_D}\right)_{t_D} \equiv v_{S_w} \tag{2.47}$$

where v_{S_w} represents the specific velocity associated with the saturation S_w, but has been normalised by the bulk fluid interstitial velocity q_t/ϕ, to make the system dimensionless. By elimination of either of the derivatives in equation (2.47) with equation (2.41) yields:

$$v_{S_w} = \mathrm{d}f_w/\mathrm{d}S_w = f_w^{'} \tag{2.48}$$

This can also be written as:

$$\left(\frac{\mathrm{d}x_D}{\mathrm{d}t_D}\right)_{S_w} = v_{S_w} = \left(\frac{\mathrm{d}f_w}{\mathrm{d}S_w}\right)_{S_w} \tag{2.49}$$

The slope of the fractional-flow curve is the derivative $\mathrm{d}f_w/\mathrm{d}S_w$.

The velocity of the moving characteristic with water saturation S_w **is the derivative** $\mathrm{d}x_D/\mathrm{d}t_D$.

Equation (2.48) shows that the specific velocity of a given saturation equals the derivative of the fractional flow curve at the same saturation. This then is the essence of the Buckley-Leverett analysis, as all saturations between the saturation at the injection condition S_{wJ} and the saturation at the initial condition S_{wI} can subsist at the origin of x_D–t_D and a given saturation has a specified velocity. Thus, a graph of saturation point or location versus time will result in a set of straight lines in the x_D–t_D plane starting from the origin as shown in figure 2.12. From equation (2.49), the position or distance of any saturation at a given dimensionless time t_D can be expressed as:

$$x_D(S_w) = t_D\left(\frac{\mathrm{d}f_w}{\mathrm{d}S_w}\right)_{S_w} \tag{2.50}$$

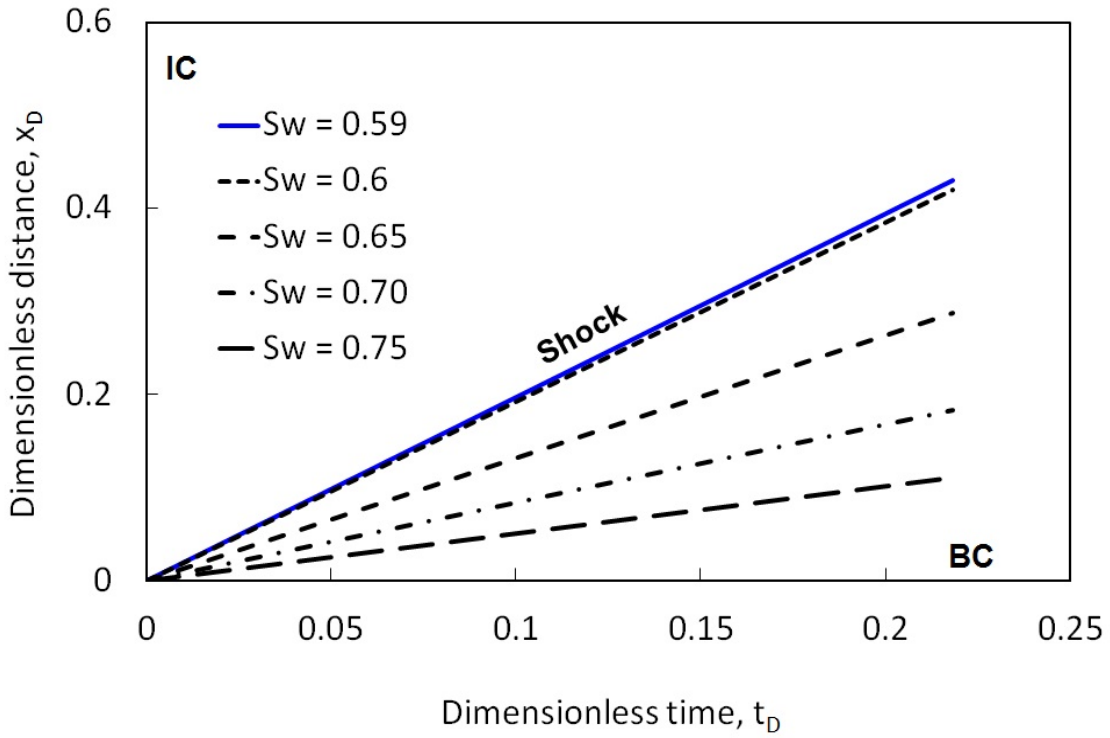

Figure 2.12: A typical dimensionless distance versus dimensionless time diagram showing characteristic lines at different water saturation S_w; reproduced from the data of (Tarek, 2006) where x_D and t_D are defined by equation (2.50). Initial condition IC: $t_D = 0$, $S_w = 0.25$. BC: $x_D = 0$, $S_w = 0.75$. Adapted from Tarek (2006).

The above example was for a system of water and oil with oil being the displaced fluid and water the displacing fluid. It was assumed that the porous medium was initially mostly saturated with oil and had a comparatively small (irreducible) water saturation, denoted S_{wr} or S_{wi}; therefore, in dimensional form, the initial condition simply means $S_w(x, t = 0) = S_{wr} = S_{wi}$ (the subscript r denotes residual and i denotes irreducible). In other words, it is also assumed here that the initial water saturation is at the irreducible water saturation. Furthermore, the boundary condition in dimensional form is $S_o(x = 0, t) = S_{or} = S_{oi}$; where S_{oi} is the irreducible oil saturation. This boundary condition simply means that water is injected at the boundary $x = 0$ into an initially oil-saturated reservoir. Fluids upstream and downstream are separated by a contact discontinuity or shock, which we discuss next.

2.4.2.3 Shock formation

As mentioned in the previous sub-section, most fractional flow curves have an inflection point; the location of which depends on the endpoint mobility ratio. It can be deduced from equation (2.48) that assuming the inflection point lies between S_{wI} and S_{wJ}, then the saturation specific velocity (i.e. velocity of the characteristics) will pass through a maximum between this range. Thus, the resulting saturation profile from the solution could yield more than one water saturation values at a given dimensionless distance x_D and dimensionless time t_D as shown in figure 2.13. Such a solution that gives rise to multiple water saturations at a particular distance and time is actually technically and mathematically valid, but non-physical. The reason why non-physical effects potentially arise is that dissipation-free conservation equations which idealise natural conservation laws by neglecting dissipative effects such as dispersion, diffusion, capillary pressure, compressibility, and thermal conductivity are often associated with hyperbolic equations (Courant and Friedrichs, 1999a). Physically the solution selects one or other of the solution branches separated by a shock (Courant and Friedrichs, 1999b). A shock is simply a discontinuity or sudden jump in liquid saturation at a position that moves over time during a displacement process. In real life, dissipative mechanisms are always present, and the shock is an idealisation of a rapid change in a variable over a small distance. Idealising in this fashion simplifies the analysis however and often helps to approximate the true behaviour of the phenomenon to a good extent.

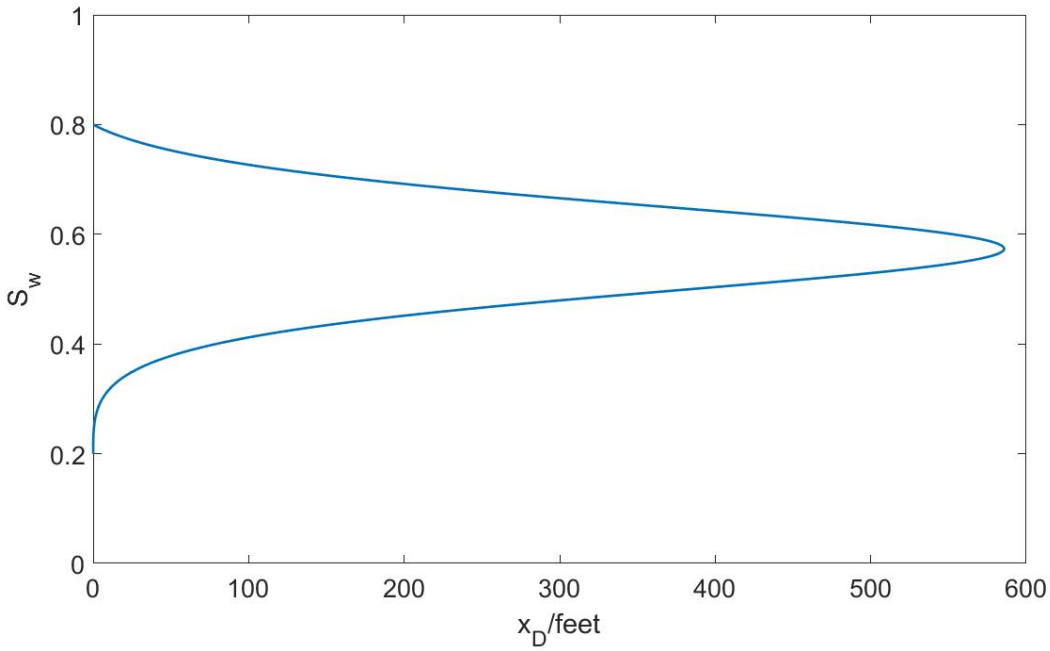

Figure 2.13: Typical shape of first calculation of saturation profile at a particular time from the data of Tarek (2006) showing anomaly (non-physical, multi-valued solution).

Figure 2.13 shows a first calculation of a solution for a saturation profile at a particular time. The solution above is not possible in reality (even though it is a mathematically valid solution of equation (2.46)) as there can only be one distinct saturation value at a given time and distance. For instance, in figure 2.13, at a distance of 200 feet, two saturations (approximately 44% and 69%) could exist. Geometrically, this double value region can be eliminated by invoking the formation of shocks by drawing a perpendicular at x_f, where x_f (to be determined later) is the distance at the saturation front as seen in figure 2.14.

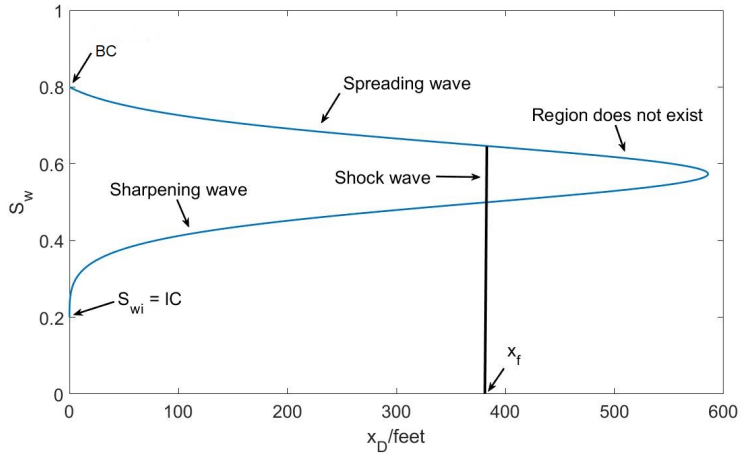

Figure 2.14: Typical saturation profile showing formation of different waves with perpendicular drawn at x_f in order to eliminate double or multiple saturation values (Hirasaki, 2009). Here, only the spreading wave and the shock appear after the perpendicular was drawn.

Once a shock has been invoked, its position has to be located on the fractional flow curve. To determine the saturation (or the leading edge of the front) at which the shock front exist, Welge (1952) recommended that from the initial water saturation, a tangent has to be drawn to the fractional flow curve as shown in figure 2.15. S_{wf} and f_{wf} gives the corresponding water saturation at the front and the water fractional flow at the front respectively at this point as demonstrated below in figure 2.15. It is pertinent to note at this point, that in fact, the method for finding the water saturation on the downstream side of the shock front by tracing a tangent to the fractional flow curve from the initial condition point, actually results from the water mass balance as is explained in the pages that follow.

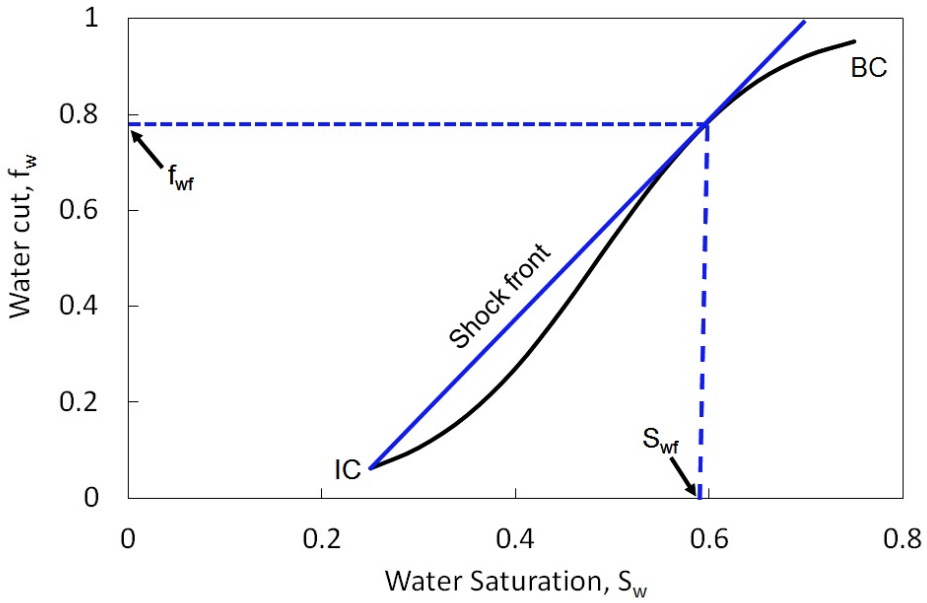

Figure 2.15: Fractional-flow curve at initial condition (IC) of 75% oil saturation, i.e. initially at irreducible water saturation for the data of Tarek (2006).

In order to determine the location, velocity, and magnitude of the shock front analytically, a water mass balance is usually performed over a control volume that contains the shock in time interval Δt. This is analogous to equations (2.34)–(2.36).

$$\begin{aligned} &\text{(Volume of water in)} - \text{(Volume of water out)} \\ = \;&\text{(Final volume of water)} - \text{(Initial volume of water)} \end{aligned} \tag{2.51}$$

$$\begin{aligned} A(f_w(S_w^+) - f_w(S_w^-))q\Delta t = [(v_{sf}(t+\Delta t) - x_1)S_w^+ + (x_2 - (v_{sf}(t+\Delta t))S_w^-]A\phi - \\ [(v_{sf}t - x_1)S_w^+ + (x_2 - v_{sf}t)S_w^-]A\phi \end{aligned} \tag{2.52}$$

where A represents cross-sectional area, S_w^+ represents the water saturation values upstream of the shock, and S_w^- represents the water saturation values downstream of the shock, while the upstream and downstream positions of the control volume in question are represented by x_1 and x_2 respectively. Solving for the shock velocity v_{sf} leads to:

$$v_{sf} = \frac{f_w(S_w^+) - f_w(S_w^-)}{S_w^+ - S_w^-} \frac{q_t}{\phi} \tag{2.53}$$

At constant flow rate (q_t) and constant porosity (ϕ), equation (2.53) reduces to:

$$v_{sf} = \frac{f_w(S_w^+) - f_w(S_w^-)}{S_w^+ - S_w^-} \tag{2.54}$$

Recall that the velocity associated with the saturation S_w is given by:

$$v_{sf} = \frac{\mathrm{d}f_w}{\mathrm{d}S_w} = f_w' \tag{2.55}$$

The shock saturation must satisfy equations (2.54) and (2.55) in order to be physically possible and join continuously on with the spreading wave (Hirasaki, 2009). In other words, the velocity derived from the fractional flow curve must equal the velocity of the shock front derived from mass balance. Equating equations (2.54) and (2.55), and taking the initial water saturation to be the downstream water saturation gives:

$$f_w'|_{S_{wf}} = \frac{f_w(S_{wf}) - f_w(S_{wI})}{S_{wf} - S_{wI}} \tag{2.56}$$

This defines water saturation at the shock front S_{wf}.

If the above equation is interpreted graphically in f_w–S_w space, it will be viewed as a straight line passing through point $(S_{wI}, f_{wI}) \equiv (S_{wI}, f_w(S_{wI}))$ which is tangent to the fractional flow curve at $(S_{wf},\ f_{wf})$ as stated on page 57 and shown in figure 2.15, with the slope of the line being the specific velocity of the shock. This is analogous to equation (2.49) which is a formula for a general characteristic, whereas equation (2.56) is a formula for a characteristic specifically at the front.

The above discussion concerned water displacing oil. Calculating the saturation profile solution for a SAG process (gas displacing surfactant solution) is similar (Castillo et al., 2020). The initial condition (IC) is usually taken to be a fully saturated porous medium with a uniform surfactant concentration, that is $S_{wI} = 1$ (assuming there is no irreducible gas present initially) and $f_w = 1$, while the gas injection condition (J) is usually taken to be at $S_{wJ} = S_{wr}$ (it's enough to say: $f_w = 0$ (assuming no irreducible water)). The fractional flow curve is then constructed using equation (2.23), but using k_{rg}^f (the relative permeability of foamed gas) instead of k_{rg}. By drawing a line through the initial point (IC) tangent to the fractional flow curve, the shock point or contact discontinuity can be found. The overall displacement will then follow a pathway along the fractional flow curve from the injection point (J) straight to the shock point (S_{wf}, f_{wf}); before jumping to the initial condition point (IC). Equation (2.48) gives the saturation velocity at each saturation along the path, while equation (2.53) gives the shock front velocity. By recognising the fact that downstream of the front, S_w is at initial conditions, saturation profile S_w vs x_D can be plotted at a given dimensionless time t_D. The above fractional flow model constitutes the main model that we will work with here. For the sake of completeness, other foam models are briefly discussed below even though the main focus of this work will be the fractional flow model.

2.4.3 Mechanistic models

The mechanistic models, though complete in principle, usually prove difficult when it comes to obtaining reliable data. These approaches are regarded as complete models in principle because they capture foam rheology, complex reservoir geology and can also be used to describe two-dimensional displacements (Zeilinger et al., 1995) (as opposed

e.g. to 1D fractional flows). Indeed some studies including Rossen et al. (1991), Zhou and Rossen (1992) and Zhou (1994) have commented that the aforementioned fractional flow method is often limited to one-dimensional displacements, assuming local equilibrium and incompressible phases, and with such limitations, cannot model 2D phenomena like gravity override or fingering. All these and other limitations are overcome in the mechanistic model. Some examples of the mechanistic models are discussed below.

2.4.3.1 "Population balance" model

This model is based on quantifying the relationship between mobility and foam texture, and including mechanisms involved in the creation and destruction of the lamellae (thin liquid films) which in turn determine texture; and then applying a "population balance" to the lamellae. This method is fully described by Walsh and Lake (1989), Friedmann et al. (1991), Chang et al. (1990), Kovscek et al. (1993), and Kovscek and Radke (1994). This model is related to another model worth mentioning; the **"implicit texture"** model which is a special case of the population balance model assuming an equilibrium population of lamellae. The implicit texture model incorporates the effect of foam texture in a porous medium by introducing a gas mobility reduction factor (Shi, 1996; Farajzadeh et al., 2015; Lotfollahi et al., 2016) (see also section 2.4.2.2). According to Shi (1996), the texture is not represented explicitly, only its effect on mobility is retained. As alluded to above, the model assumes that between the process of foam creation and destruction, there is a local equilibrium (LE). According to Lotfollahi et al. (2016), the implicit texture model that manages to incorporate a sudden change in foam texture and other foam properties close to a given water saturation can be re-cast as a local equilibrium (LE) version of a corresponding population balance model with a lamellae destruction function

that increases abruptly in the neighbourhood of some limiting capillary pressure, with capillary pressure being a function of water saturation. Furthermore, the relationship between steady state foam texture (even if not obtained explicitly) and water saturation or capillary pressure in the implicit texture model is essentially the same as that of the population balance model (Lotfollahi et al., 2016). Thus, the implicit texture model can indeed be said to be a special case of the population balance model.

Despite its potential, the population balance model has however been described as a cumbersome method by Shi (1996). This is because there are many parameters involved when using this method. In addition, a large numbers of parameters could be different in different processes. Thus, these parameters can only be obtained from exhaustively large quantities of experimental data, which in most cases are bound to produce significant uncertainties. Another issue with the population balance method was that it was not easy to separate the rates of lamellae generation and destruction during history matching of coreflood results, because an increase in generation rate was equivalent to a decrease in destruction rate (Zhou and Rossen, 1994).

2.4.3.2 "Fixed-P_c*" or "fixed limiting capillary pressure" model

Another approach as discussed in several literature references including Holm (1968), Friedmann et al. (1991), Rossen et al. (1994), Zhou and Rossen (1995), Rossen (1996) and Zhang et al. (2009); this approach, already alluded to in the context of empirical models, is known as the **"fixed-P_c*"** or fixed limiting capillary pressure model. This method is centred around the relationship between foam texture, foam mobility and capillary pressure. According to this model, for every so called strong foam (defined shortly), a certain value of capillary pressure exists at which the strong foam suddenly

transitions to a so called weak foam (again defined shortly). In other words, there is a certain value of the capillary pressure at which moving lamellae break in porous media. Amongst other things, this then would imply a need to incorporate capillary pressure within an expression for breakage rate of lamellae within a population balance model. The references mentioned above defined a strong foam as one in which the liquid films (or lamellae) that constitute the foam are stable enough to survive as they transit from from pore to pore; while a weak foam is one in which the lamellae do not even advance from pore to pore, but rather break and form again at fixed positions. Alternatively, strong and weak foams can be defined in terms of the discontinuity or continuity of the gas flow paths for a foam within a porous medium, because, for a given volume of porous media containing foam, there exists a continuous gas foam when there is at least a single continuous flow path along the length of the porous medium that is not interrupted by the presence of a foam lamella. On the other hand, there exists a discontinuous gas foam when there is at least a single foam lamellae along each and every gas flow path in the porous medium volume. This means that in porous media, for gas to flow through a discontinuous gas foam, the gas must propagate, mobilise or possibly even break or burst at least one foam lamella. From the above, when a discontinuous gas foam occurs, a strong foam can be said to exist, while a weak foam can be said to exist when a continuous gas foam occurs. Figure 2.16 shows a schematic diagram of the two different types of foam explained.

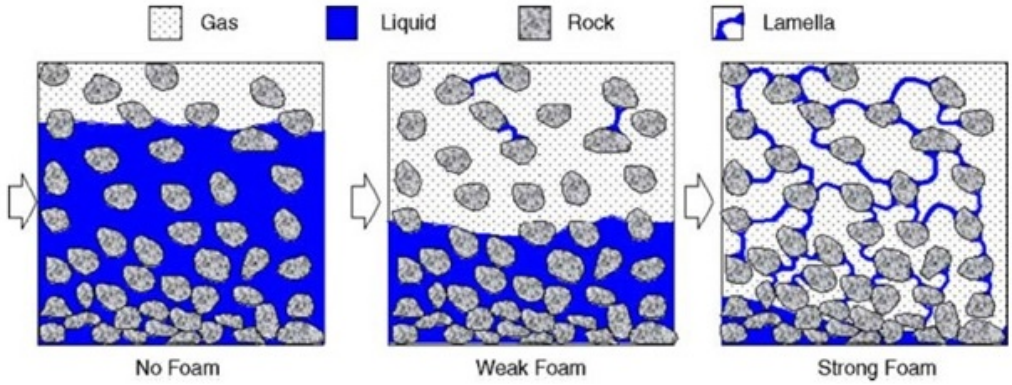

Figure 2.16: Concept of weak and strong foams within a porous medium (Dholkawala et al., 2007).

As stated before, the fixed-P_c* model involves three interrelated quantities viz. foam texture, foam mobility and capillary pressure. The value of the capillary pressure at which a strong foam suddenly or abruptly changes to a weak foam is called the limiting capillary pressure. In other words, the lamellae cannot be sustained beyond this point, thereby foam becomes unstable (Khatib et al., 1986; Kovscek and Radke, 1993b; Farajzadeh et al., 2016). It is noteworthy to mention that this value should not be mistaken for another value of capillary pressure known as the critical capillary pressure (for foam collapse); defined as the value of the capillary pressure at which *static* lamellae break in porous media. Instead the limiting capillary pressure may be somewhat lower than the critical capillary pressure (Shi, 1996). The greatest emphasis in this method was on the dominant role capillary pressure has in controlling foam texture and gas mobility, as the stability of lamellae is dependent on the capillary pressure in porous media (Zhou, 1994). In addition, according to Kovscek and Radke (1994), the primary mechanism for foam destruction in porous media is due to capillary suction. The model described above can be explained with the simple relationship between water saturation (S_w) and capillary pressure (P_c) which is often represented by the capillary-pressure function $P_c(S_w)$, as shown in figure 2.17.

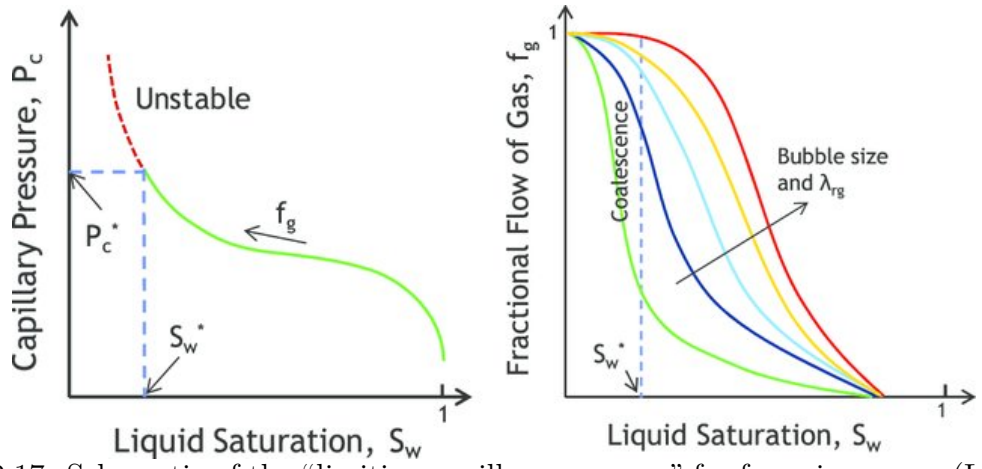

Figure 2.17: Schematic of the "limiting capillary pressure" for foam in porous (Lotfollahi et al., 2016). Fractional flow of gas f_g (which is $1 - f_w$, where f_w is the fractional flow of water) is also shown. In figure 2.17b, if S_w were to reduce at fixed bubble size, f_g would initially grow following one of the curves shown corresponding to specified bubble size. However once S_w* is reached, bubble size would not remain fixed, and the system would cross from curve to curve with bubble size increasing.

The figure above shows that the capillary pressure is a monotonic function of liquid saturation. As such, if the capillary pressure during foam displacement process does not exceed the limiting capillary pressure value, because of the stability of the lamellae (the region below the unstable zone in figure 2.17), then the liquid saturation must be greater than or equal to the liquid saturation corresponding to P_c* (that is the limiting water saturation S_w*). Then supposing that gas and liquid are flowing as a foam of constant bubble size (shown by the figure on the right hand side with the curves representing fractional flow curves for different bubble sizes) at a given gas velocity, as the gas fractional flow is raised, the liquid saturation declines until it reaches the limiting value S_w* at the limiting capillary pressure (P_c*). A further increase in the gas fractional flow causes the foam texture to coarsen so as to keep the capillary pressure from rising above the limiting capillary pressure. In other words, approaching the limiting capillary pressure from lower capillary pressure P_c (that is approaching S_w* from higher S_w), bubble size increases, gas mobility rises and gas fractional flow in the porous medium increases (Lotfollahi et al., 2016).

With respect to foam quality, Shi (1996) stated that foam can remain at a fixed water saturation over a wide span of foam qualities and flow rates. Foam quality in this context simply means the flowing volume fraction of gas in the foam, and is usually expressed as shown in equation (2.57) below. According to Zhou and Rossen (1995), there are cases when the limiting capillary pressure (P_c*) is not dependent on the gas and liquid flow rates. In cases like this, according to Zhang et al. (2009), the aqueous limiting saturation (S_w*) and aqueous mobility (λ_w*) at this saturation are constants which do not depend on the gas-liquid flow rates and pressure gradient. They further pointed out that at the aqueous phase limiting saturation (S_w*), foam quality equals the fractional flow of gas which can vary even with the value of S_w fixed at S_w*. This they expressed mathematically in terms of the gas mobility (which is simply the ratio of the gas phase's effective permeability to the gas phase's viscosity) as shown in equation (2.58). Bernard et al. (1965), Friedmann and Jensen (1986) and Holm and Garrison (1988) in their various studies also found that foam does not affect the relative permeability-water saturation function $k_{rw}(S_w)$. Therefore $k_{rw}(S_w)$ is nearly constant over this same set of flow rates. The equation we have is:

$$f = \frac{q_g}{q_w + q_g} \tag{2.57}$$

where:

f = foam quality

q_g = gas volumetric flow rate

q_l = liquid volumetric flow rate

$$\lambda_g = \lambda_w * \frac{q_g}{q_w} = \lambda_w * \left(\frac{1 - f_w}{f_w}\right) = \lambda_w * \left(\frac{f}{1 - f}\right) \text{ at } S_w = S_w * \tag{2.58}$$

where:

λ_g = gas mobility

λ_w* = aqueous phase limiting mobility

q_g = gas flow rate

q_w = water flow rate

f_w = water cut or fractional flow of water

f = foam quality

S_w = water saturation

S_w* = aqueous phase limiting saturation

Equation (2.58) shows that at the limiting capillary pressure (P_c*), gas mobility is a function of foam quality (f) and limiting water saturation (S_w*) for foam collapse only, since λ_w* = $\lambda_w(S_w$*).

Furthermore, in a porous medium more generally, foam quality can either be described as low quality or high quality. On the one hand, in the low quality flow regime, there is not much dependence of the pressure gradient on the liquid flow rate. Instead, in this flow regime, shear thinning occurs depending on the total flow rate (Dharma, 2013). Also, in the region of low quality foam in a porous media, water saturation is allowed to change with changing quality while bubble size is fixed (Rossen and Wang, 1999; Alvarez et al., 2001). On the other hand, the dependence of the pressure gradient on the gas flow rate is limited in the high quality flow regime. Here, water saturation remains at the water saturation corresponding to the limiting capillary pressure and capillary pressure remains at the "limiting capillary pressure" (Dharma, 2013). The studies of Khatib et al. (1986),

Rossen and Wang (1999) and Alvarez et al. (2001) showed that both regions of foam quality in media are governed by different mechanisms; while the high quality regime is dominated by coalescence of bubble near the limiting capillary pressure, the low-quality foam region is governed by bubble trapping and mobilisation.

Rossen et al. (1994) summarised the fixed-P_c* model as a form of the population balance model at local equilibrium, as has already been alluded to earlier. In other words, the fixed-P_c* model is a form of the equilibrium population balance for strong foams under certain conditions; mainly where the dominant factor on foam texture and gas mobility is the capillary pressure. Essentially, it is a local equilibrium at steady state between the lamellae generation and collapse. Be that as it may, unlike the population balance model where parameters have to be obtained from extensively large experimental data sets, here S_w* can be determined by a few experiments in the limiting capillary pressure regime.

It can be said that the fixed-P_c* model applies best to strong foams with capillary pressures up to the fixed limiting pressure, at low flow rates typical of EOR compared to primary recovery processes with high flow rates that could destroy lamellae and weaken foam (Rossen et al., 1991). In other words, it describes foam at steady state including subsequent to the time of foam generation or at the leading edge of an advancing foam front (Zhou and Rossen, 1995). The whole essence of the model is that as long as capillary pressure is low and surfactant is present, foam greatly reduces gas mobility (Rossen and Zhou, 1995; Shi, 1996). The study of Shi (1996) showed that the transition between low mobility gas with foam and higher mobility gas in the absence of foam happens over a narrow set of water saturations close to the limiting water saturation S_w* which corresponds to P_c*. (Rossen and Zhou, 1995) and (Shi, 1996) in their studies stated that one implication of the limiting capillary pressure model is that foam with capillary pressure

approaching the limiting capillary pressure P_c* will preferentially divert flow from high to low permeability layers (i.e. from low to high capillary pressure layers) assuming the layers are isolated from each other by an impermeable layer, thereby not allowing for fluid cross flow. Hence, foam will partially plug the high permeable layer, while diverting flow into the low permeable layer. This was corroborated by Yaghoobi and Heller (1996) who studied CO_2 foam in short composite cores composed of sand and sandstone (two parallel porous media) and found out that there was CO_2 diversion to the low permeable part of the porous media, and a delay in CO_2 breakthrough from the high permeable region.

On the contrary, if the layers are in capillary equilibrium and fluid cross flow is allowed, foam can divert flow into the high permeability layer, contrary to the usual objectives of a foam displacement process (Kovscek et al., 1997). This assertion concurs with the work of Bertin et al. (1999) who studied the effect of cross flow in heterogeneous porous media and reported as seen under CT scan images used in their study, that when the layers are in capillary communication, foam fronts move at identical rates in each porous medium. Therefore, in this case, rather than gas diverting into the low permeable layer, the reverse might happen as gas mobility is balanced. Thus, high flow resistance due to foam causes gas to divert into an adjacent layer of high permeability.

The fixed-P_c* model has some limitations though. Rossen et al. (1991), Zhou and Rossen (1994), and Shi (1996) stated that, by treating the model as a local equilibrium model, the model failed to describe slow generation or slow coalescence processes of foam that might be dependent on flow rates. Shi (1996) showed that, for foam that conforms to the fixed-P_c* model, if S_w<S_w*, gas mobility in the presence of foam is equal to gas mobility in the absence of foam and foam collapses; however if S_w>S_w*, gas mobility is reduced

greatly.

Using the fixed-P_c* model, Zeilinger et al. (1995) and Shi (1996) in their respective studies represented the effect of foam on gas mobility as a function of the reduction in gas relative permeability k_{rg} below its foam-free value k^o_{rg}. As stated previously, the transition between low mobility gas with foam and higher mobility gas in the absence of foam can be considered to happen over a narrow domain of water saturations ($\pm\epsilon$) close to the limiting water saturation S_w*. This then represents a **"progressive collapse"** model (Shan and Rossen, 2004) which generalises the original fixed-P_c* model (which strictly speaking would have $\epsilon \to 0$).

Thus, the relative permeability functions can then be expressed as:

For $S_w <(S_w{}^* - \epsilon)$ or for surfactant concentration less than some threshold value required for foaming ($C_s <C^o_s$)

Then

$$k^f_{rg} = k^o_{rg} \tag{2.59}$$

In other words, no foam is formed or generated if the water saturation S_w is less than (S_w*$-\ \epsilon$) or the surfactant concentration C_s is less than C^o_s.

For (S_w*$-\ \epsilon$)$\leq S_w \leq$ (S_w*$+\ \epsilon$) and $C_s \geq C^o_s$,

Then

$$k^f_{rg} = \frac{k^o_{rg}}{\left[1 + \frac{(R-1)(S_w - S_w{}^* + \epsilon)}{2\epsilon}\right]} \tag{2.60}$$

Here, the reduction of gas relative permeability increases linearly with S_w, up to some maximum factor $R \gg 1$.

For $S_w >(S_w{}^*+ \epsilon)$ and $C_s \geq C^o_s$

Then

$$k_{rg}^{f} = \frac{k_{rg}^{o}}{R} \tag{2.61}$$

Here, there is full strength permeability reduction achieved with a permeability reduction factor R. Equations (2.59)–(2.61) are continuous at $S_w = S_w* \pm \epsilon$, but unfortunately their derivatives are not continuous at those points. This however can be rectified by replacing (2.59)–(2.61) by a smoothed function that essentially has the same effect. This can be achieved via an arctan function (effectively what is done in equations (2.32)–(2.33)) or else via a hyperbolic tangent (see equation (3.2) within the published paper contained within chapter 5). The data presented in chapter 4 of this work used the arctan function.

In the absence of foam, Shan and Rossen (2004) fitted the relative permeability to the data of Persoff et al. (1991) with the following functions:

$$k_{rw} = 0.2\left(\frac{S_w - S_{wr}}{1 - S_{gr} - S_{wr}}\right)^{4.2} \tag{2.62}$$

$$k_{rg}^{o} = 0.94\left(\frac{1 - S_{gr} - S_w}{1 - S_{gr} - S_{wr}}\right)^{1.3} \tag{2.63}$$

where:

k_{rw} = relative permeability of water

S_w = water saturation

S_{wr} = connate or residual water saturation (i.e. the lowest water saturation in situ the porous medium. This may be different from the irreducible water saturation, S_{wi} which is the lowest water saturation that can be achieved in a porous medium by displacing the

water by oil or gas, although for the most part we will treat them as being synonymous)

S_{gr} = residual gas saturation

k_{rg}^{o} = gas relative permeability in the absence of foam

k_{rg}^{f} = gas relative permeability in the presence of foam

S_w = water saturation

$S_w{}^*$ = water saturation at the limiting capillary pressure (i.e. $S_w = S_w{}^*$ at $P_c{}^*$)

C_s = concentration of surfactant in the aqueous phase

C_s^o = threshold surfactant concentration for foam

ϵ = a parameter in the fixed-$P_c{}^*$ model (or more precisely in the progressive collapse generalisation thereof) for gas mobility with foam. It represents the range of saturation values over which foam collapse occurs.

R = a parameter in the fixed-$P_c{}^*$ model for gas mobility with foam. It represents the maximum mobility reduction factor in a foam IOR process.

Studies including Zhou and Rossen (1992), Shi (1996), etc. have shown that the particular value of the R is not important as long as it is sufficiently large; then practically all f_w values fall in the transition zone represented by equation (2.60); the exact R values affects only the high f_w portions of the fractional flow curve which is not usually involved in most IOR processes (Zhou and Rossen, 1992).

The set of equations above (equation (2.59)–(2.61)) represent, as mentioned earlier, another foam rheology model which actually is just a modification/generalisation of the fixed-$P_c{}^*$ model and is termed the **"progressive collapse"** model (Shi, 1996; Rossen and Wang, 1999; Shan and Rossen, 2004). According to Rossen and Wang (1999), if ϵ approaches zero (and also typically R is large), then this model reduces to the fixed-$P_c{}^*$

model. This model basically considers the near vertical drop in $f_w(S_w)$ as S_w falls below S_w*, the drop moreover being substantial when R is large. Here, the fractional flow curve with foam approaches the foam-free curve progressively until the curves meet. Two particular cases of this modification were studied by Shi (1996) and Shan and Rossen (2004). The first case is the 2% progressive-collapse model (here, $\epsilon = 0.01$) in which over a 2% range in S_w, foam coarsened progressively with a moderate mobility bank as seen in the dimensionless distance-time diagram in figure 2.18a. There is another version of this model in which over a 10% (here, $\epsilon = 0.05$) range in S_w, foam collapses too but in this case, the collapse is not as rapid as in the previous model; now foam collapses more gradually with lower mobilities behind the foam bank as shown in figure 2.18b. The major difference between these two modifications of the fixed-P_c* model, is that here the region where foam collapses extends over a bigger region of space and time than that of the fixed-P_c* model (Shan and Rossen, 2004).

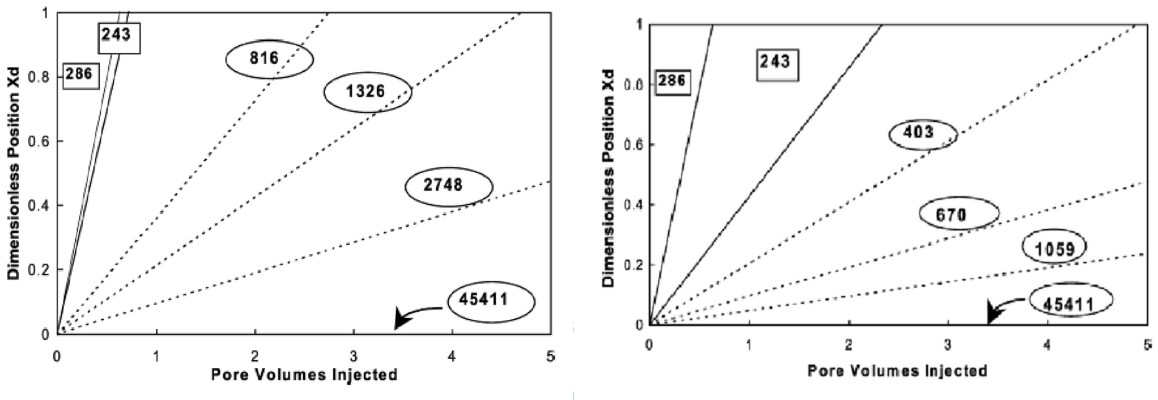

(a) 2% progressive-collapse model (b) 10% progressive-collapse model

Figure 2.18: Dimensionless distance-time diagram corresponding to two cases of the progressive-collapse model (Shan and Rossen, 2004). Characteristic lines are shown and numbers labelling the lines are overall (gas plus liquid) relative mobilities in $(\text{Pa.s})^{-1}$.

The lines drawn through the origin are the characteristic lines which represent waves that are moving from the injection point, while the wave velocity corresponds to the slope of the lines. The numbers in the boxes represents the total relative mobility (in units of

$(Pa.s)^{-1}$) for a constant state region which is represented by the solid lines. The numbers in the circles represents the total relative mobility for a single characteristic in the region of spreading wave, which is represented by the dotted lines. The relative permeability curves and fractional flow curves constructed from the above set of equations are shown in figures 2.19 and 2.20. Also, the fractional flow curve for this model is shown in figure 2.21.

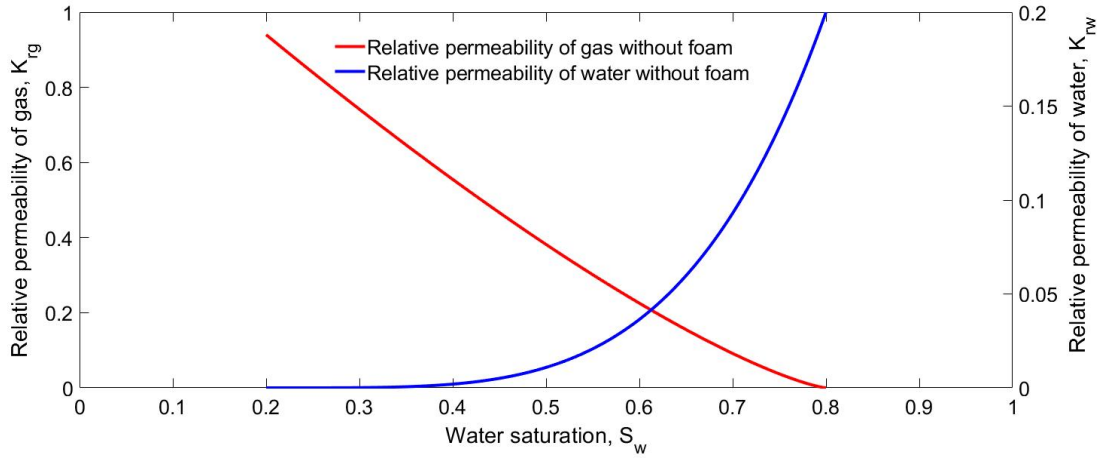

Figure 2.19: Relative permeability curve without foam for the progressive collapse model based on the data of Persoff et al. (1991), defined by equations (2.62) and (2.63); with $\epsilon = 0.01$, $S_w{}^* = 0.37$, $R = 18500$.

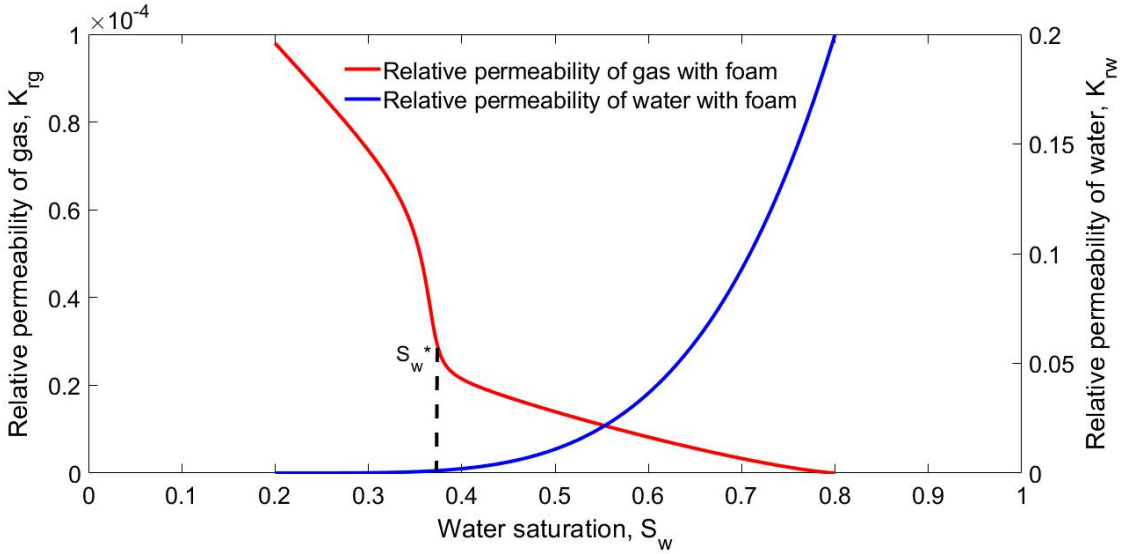

Figure 2.20: Relative permeability curve with foam for the progressive collapse model based on the data of Persoff et al. (1991), defined by equations (2.59)–(2.61); with $\epsilon = 0.01$, $S_w{}^* = 0.37$, $R = 18500$, showing drastic reduction of the relative permeability of the gaseous phase in the presence of foam. Worth mentioning here is that at $S_w = S_w{}^* = 0.37$, gas mobility will fall sharply as the relative permeability of gas falls sharply too while the relative permeability of water is still very low around that area.

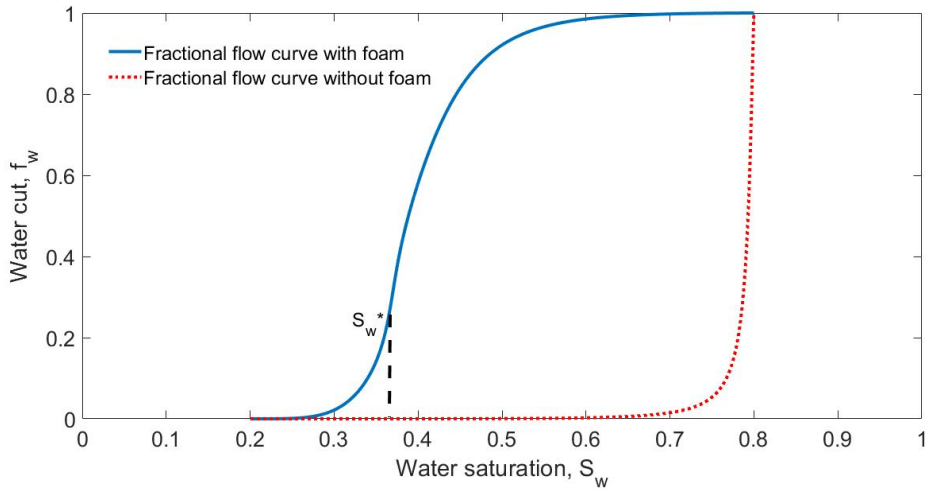

Figure 2.21: A fractional flow curve for the progressive collapse model based on the data of Persoff et al. (1991) using the relative permeability data from figures (2.19) and (2.20), equations (2.24) and equations (2.59)–(2.63) with $\epsilon = 0.01$, $S_w{}^* = 0.37$, $R = 18500$, $\mu_g = 0.018$ cp and $\mu_w = 1.2$ cp. After $S_w{}^*$, f_w only increases quite gradually as the relative permeability of water is still very low around $S_w = S_w{}^* = 0.37$.

The relative permeability reduction for the gaseous phase in the presence of foam means that the mobility of the gas phase would be reduced because mobility is a function of viscosity and relative permeability only. In the system of interest here, the porous medium was initially saturated with surfactant. From the injection point, gas then displaces liquid to reduce water saturation. As figure 2.21 shows, the fractional flow curve at any given f_w shifts towards smaller values of S_w due to gas mobility being lower due to foam.

So far we have reviewed the fixed-$P_c{}^*$ model and its generalisation to progressive collapse (which are the main models we will work with here). According to Zhou and Rossen (1994) however, fractional flow methods predict that a foam that obeys the fixed-$P_c{}^*$ model in particular would collapse when a gas is injected into a core filled with surfactant. This is because the foam is created, dries out and collapses in a shock front of negligible width between injected gas (J) and previously injected surfactant solution (I). The problem with the fixed-$P_c{}^*$ model in particular is that at very low values of f_w which are typical of a successful IOR process, the model does not result in a fractional flow curve that is

smooth at those low values of f_w. Attempts to address this issue led to another model by Fisher et al. (1990) discussed below.

2.4.3.3 Fisher model

Using the data of Lee and Heller (1990), Fisher et al. (1990) proposed a different way of studying foam displacement processes in porous media as opposed to the local equilibrium method used in the description of the fixed-P_c* model. The authors used steady state foam phase mobilities which can directly be measured from core flood experiments. According to Fisher et al. (1990), phase mobilities in the absence of foam can be expressed as:

$$\lambda_{rw} = \frac{0.72}{\mu_w}\left(\frac{S_w - S_{wr}}{1 - S_{wr}}\right)^{2.0} \tag{2.64}$$

$$\lambda^o_{rg} = \frac{1}{\mu_g}\left(\frac{S_g - S_{gr}}{1 - S_{wr}}\right)^{2.0} \tag{2.65}$$

where:

λ_{rw} = aqueous phase relative mobility

μ_w = aqueous phase viscosity

λ^o_{rg} = gaseous phase relative mobility in the absence of foam

μ_g = gaseous phase viscosity

S_w = aqueous phase saturation

S_g = gaseous phase saturation

S_{wr} = connate saturation of aqueous phase = 0.15 [as used in Fisher et al. (1990)]

S_{gr} = residual gas saturation (assumed to be zero here)

Recall here that for a phase, j, mobility can be expressed as:

$$\lambda_j(S_j) = \frac{k_j(S_j)}{\mu_j} = \frac{k k_{rj}(S_j)}{\mu_j} = k\lambda_{rj}(S_j) \tag{2.66}$$

where λ_j is the absolute phase mobility, k is the absolute permeability, k_{rj} is the relative permeability of the phase, μ_j is the viscosity of the phases, k_j is the effective permeability of the phase and λ_{rj} is the phase relative mobility.

Fisher et al. (1990) also defined the total relative mobility as the total superficial velocity divided by the product of permeability and pressure gradient. It is inversely proportional to the effective viscosity of foam. Mathematically, it can be expressed as:

$$\lambda_{rt} \equiv \left(\frac{u_g + u_w}{k\nabla p}\right) = \frac{u_w}{f_w\, k\, \nabla p} = \frac{k_{rw}}{\mu_w f_w} \tag{2.67}$$

or

$$\lambda_{rt}(S_w) = \lambda_{rw}(S_w) + \lambda_{rg}(S_w) \tag{2.68}$$

where λ_{rw} and λ_{rg} are the relative mobilities of the liquid and gaseous phase respectively at given water saturations. Note that there is a difference between the total relative mobility defined here and the total absolute mobility which is the product of the total relative mobility and permeability.

In SAG processes, both total relative mobility and total absolute mobility are (like gas relative permeability) affected by the presence of foam (in a way we will detail shortly). In a typical SAG process, water saturation declines towards the injection well during gas injection, and consequently the total relative mobility increases as shown in figure 2.22; the increase being possibly quite substantial if foam is present.

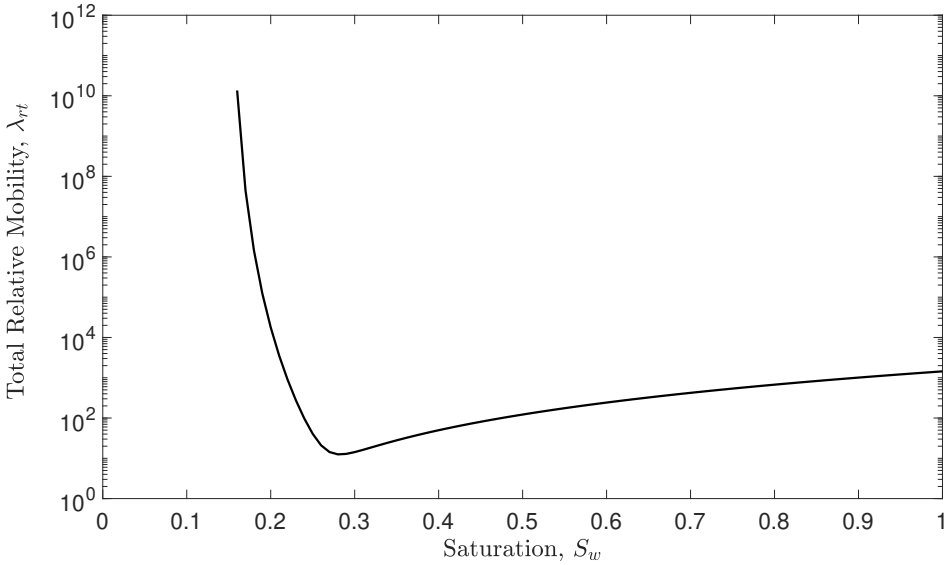

Figure 2.22: Total relative mobility of foam in units of cp^{-1} against water saturation showing increase in mobility towards the injection point (low S_w). Modified from Leeftink et al. (2015). Leeftink et al. (2015) used the STARS model shown in equation (2.33), but here the Fisher model has been used with parameters corresponding to 0.5% surfactant concentration. Both models show the same qualitative relationship between the total relative mobility and water saturation.

So far, our discussion of equations (2.64)–(2.68) has been cast in terms of mobilities. In the absence of foam (as in equation (2.64)), these equations can also be recast in terms of relative permeability using Corey's semi-empirical relative permeability functions which provide smooth functions that are differentiable and can be fit to lab data (Castillo et al., 2020). For a two phase flow of water and gas, Corey's relative permeability functions are as given in equations (2.24) and (2.25).

In the presence of foam, the aqueous phase mobility remains unchanged, as such the relative permeability of the liquid will be unchanged too. It is only the relative permeability of the gaseous phase that will change. Fisher et al. (1990) expressed this as:

$$k_{rg}^{f} = \mu_g \lambda_{rg}^{f} = \mu_g \lambda_{rg}* \left[\frac{\lambda_{rw}*}{\left(\frac{k_{rw}(S_w)}{\mu_w} \right)} \right]^{n} \tag{2.69}$$

where:

$\lambda_{rw}*$ = adjustable parameter in Fisher model for aqueous phase relative mobility

$\lambda_{rg}*$ = adjustable parameter in Fisher model for gaseous phase relative mobility

n = adjustable parameter in Fisher model

μ_w = aqueous phase viscosity

λ_{rg}^f = gaseous phase relative mobility in the presence of foam

μ_g = gaseous phase viscosity

k_{rw} = relative permeability of the aqueous phase

S_w = saturation of the aqueous phase

k_{rg}^f = relative permeability of gas in the presence of foam

In the original Fisher et al. (1990) model, the adjustable parameters; λ_{rg}^*, λ_{rw}^* and n are functions of the gas superficial velocity, but Shi (1996) ignored that dependence and instead assumed the parameters to be constant at the given values in table 2.1. The effect of the model is that when S_w increases meaning that $k_{rw}(S_w)$ likewise increases, the value of k_{rg}^f falls. This reflects strong foam being able to form for increasing S_w. Note moreover that, if for a certain liquid saturation $S_w = S_w{}^*$, the liquid relative mobility λ_{rw} happens to equal the adjustable parameter $\lambda_{rw}*$, then the gas relative mobility λ_{rg} necessarily equals the other adjustable parameter $\lambda_{rg}*$.

Table 2.1: Fisher model foam parameters at different surfactant concentration.

Parameters/surfactant concentration	0.02%	0.50%
$\lambda_{rw}*$	9.74 cp^{-1}	0.117 cp^{-1}
$\lambda_{rg}*$	9.74 cp^{-1}	0.117 cp^{-1}
n	4	1

Figure 2.23 shows fractional flow curves for the Fisher model for surfactant concentration C_s in the aqueous phase of 0.5% and 0.02%, i.e. for the data in table 2.1.

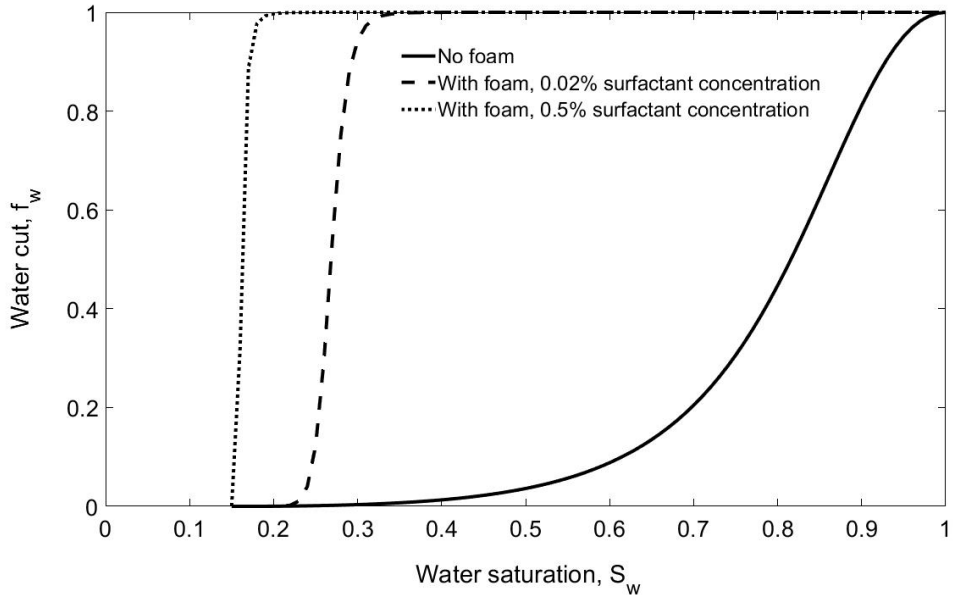

Figure 2.23: A typical fractional-flow curve for Fisher model for different surfactant concentrations based on the data of Fisher et al. (1990) using equations (2.24), (2.64), (2.65) and (2.69); with $\mu_g = 0.05$ cp and $\mu_w = 0.5$ cp.

In summary, the physical content of the Fisher model is that at a certain liquid or water saturation, the relative permeability of gas with foam equals the relative permeability of gas without foam. However, as liquid or water saturation grows and hence relative permeability of water grows, the relative mobility of gas with foam falls.

Having considered the various foam models above, it is important to state that for the purpose of this study, the focus shall be on the semi-empirical model of which the most common one is the fractional flow model: this is what has been developed in the chapters to follow. In addition, it is also pertinent to state that from all the methods discussed above, at present, there is still no model that has been universally accepted as the best model or approach, as each method has its limitations. For instance, on the one hand, the semi-empirical approaches are usually limited by knowledge of the parameters that are needed to describe foam rheology and mobility. On the other hand, the mechanistic ap-

proaches, though complete in principle usually prove difficult when it comes to obtaining reliable data (Zhang et al., 2009).

Despite the limitations with each of the approaches, there are some common grounds among all of them. For instance, it is generally accepted that foam should not be treated as a separate phase when modelling foam displacement in porous media, but instead foam modifies the behaviour of the gas phase (Zhou and Rossen, 1995). Also, there is an agreement on the treatment of water mobility as a function of water saturation both in the absence and presence of foam (Khatib et al., 1986). In other words, the mobility of the liquid phase does not change even when foam is present; it is only the mobility of the gas phase that changes as the presence of foam does not change the water phase relative permeability. Another agreement across all approaches is that foam texture controls gas mobility in foam (Falls et al., 1989).

For the purpose of this work, instead of using the Fisher et al. (1990), the fractional flow curve that was used to solve the main problem that this study aims to address was constructed on the basis of a smoothed version of the progressive collapse model which is itself based in turn on the limiting capillary pressure model. The way to incorporate this model into a system that admits a flow reversal is considered in the following chapters.

Chapter 3

Foam flow for reversed flow condition and a time-varying boundary condition

The foam flow discussed in the previous chapter only considered displacement in one direction. In other words, the previous chapter considered when the dispersed gaseous phase (that is gas within foam) displaces the residual oil left behind by natural drive and other primary oil recovery methods. It is also possible to envisage a reverse case in which the liquid phase (partly oil, but usually containing a significant amount of water plus some surfactant), whose mobility has been shown by several studies including Bernard et al. (1965), Nguyen et al. (2000), Bernard and Holm (2001) and Eftekhari and Farajzadeh (2017) to be unaffected by foam injection, is now somehow pushing the invading fluid back; hence flow reversal is occurring. This could happen at depth on a foam front, for example, if the gas injection pressure declines, an injection well is shut in, or alternatively as a new injection well comes on-line downstream of the foam flow.

Usually when gas is injected into a well, it will spread out horizontally and vertically. Gas higher up spreads faster than gas lower down (since the motion of gas lower down is opposed by a bigger hydrostatic pressure) (Grassia et al., 2014). The deepest that the gas can reach is where there is a balance between the hydrostatic pressure and the injection pressure. Then if the injection pressure is reduced a little (in some cases reduced

almost to zero), deep down (i.e. the lowest that the gas managed to reach originally), the hydrostatic pressure will eventually outweigh the gas injection pressure, thereby causing the liquid to push up on the gas. Higher up though (where the hydrostatic pressure is less), gas is still being pushed forward and is displacing liquid as is expected in a SAG process, although the motion of the gas will still be slower than before, because the injection pressure is less. This is in line with the basic knowledge of fluid flow, because for any fluid to flow in the right direction, the discharge pressure has to be greater than the receiving pressure (DeNevers and Silcox, 1991; Schobeiri, 2010). If the direction of the pressure difference is switched, then back flow or reversed flow is expected to occur. So, in the system of interest here, whether or not flow reversal occurs at a point on the foam front depends on the depth being considered. In addition, when flow reversal happens, the injector can effectively be used as a producer. In other words, in the midst of the displacement process, the injection conditions have been changed. This scenario has been illustrated with the schematic in figures 3.1 and 3.2. The simplest model one can write for this situation is: $q_t(t > t_r) = -q_t(t < t_r)$, where '$t_r$' is the instant in time at which reversal takes place, 'q_t' is total fluid flow rate and 't' is any arbitrary time other than 't_r'. Hence, foam displaces water up to 't_r', then water starts displacing foam for $t > t_r$.

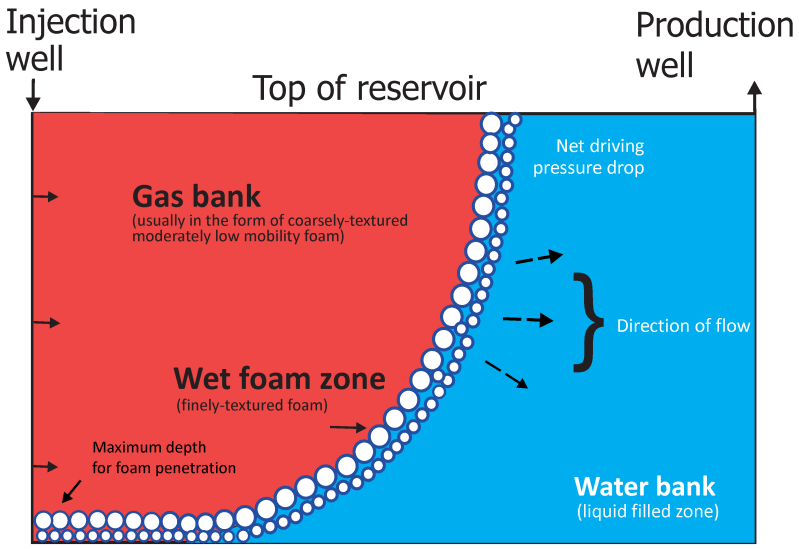

Figure 3.1: Schematic diagram of a typical SAG process before flow reversal. Gas injection produces a narrow foam front of finely-textured low mobility foam which separates downstream liquid (mostly surfactant solution) from upstream injected gas (usually in the form of coarsely textured foam). The pressure difference (net driving pressure drop) between the injection pressure and the hydrostatic pressure (where hydrostatic pressure is a function of the reservoir's depth) is what drives the motion of the foam front, hence, there is a certain depth at which the pressures balance which gives the maximum depth for foam penetration. There is a direct proportionality between the speed of the foam front and the pressure difference, while the speed is lower at the bottom of the front and greater at the top of the front). Adapted from Mas-Hernandez (2016); Eneotu and Grassia (2020).

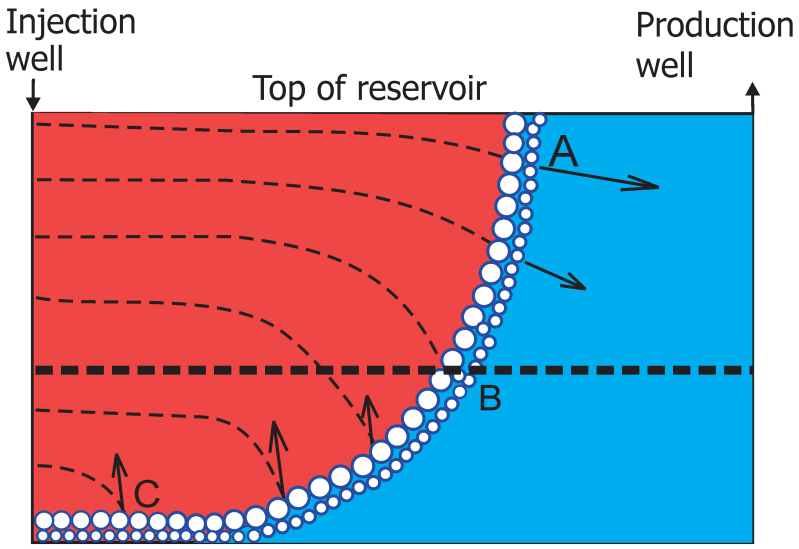

Figure 3.2: Schematic diagram of a SAG process depicting flow reversal. At the beginning, flow advances in the forward direction following the paths shown by the dashed curves. Then at a point in time, that certain depth at which the pressures balances (i.e. injection pressure and hydrostatic pressure) shown by the bold dashed line shifts higher up. This is an indication that the injection pressure has been reduced. When this happens, there will be flow reversal in part of the domain as follows. Flow at the depth corresponding to the location (marked B) where pressures balance is realised will stop moving entirely. Flow in the region below (marked C) below the depth corresponding to pressures balance will move in a reverse direction, while flow in the region well above (marked A) above the depth corresponding to pressure balance will continue to move in the same direction as normal; although the net driving pressure and flow velocity is now reduced. Adapted from Mas-Hernandez (2016); Eneotu and Grassia (2020).

Before addressing the flow reversal problem described above, the work of Hirasaki (2009) on the application of fractional flow with a time-varying boundary condition has been considered below. The reason this work is relevant is that if we impose a flow reversal during a SAG process and simultaneously change the direction in which we measure spatial coordinates, effectively what we have done is switch a high gas saturation boundary condition (upstream in the original flow) to a high liquid saturation boundary condition (upstream in the reversed flow). Moreover, unlike the initial condition for the original forward flow (which is spatially uniform) the initial condition that we "inherit" at the instant of flow reversal exhibits complex variation of liquid saturation with spatial po-

sition. The same feature is seen in the work of Hirasaki (2009): the "initial" condition inherited at the instant when the boundary condition is changed can exhibit complex spatial variation of liquid saturation. The two problems (i.e. the flow reversal one we aim to solve and the time-varying boundary condition one solved by Hirasaki (2009)) are distinct physically and mathematically, but there are analogies between them. It is important to emphasise here though, that the work of Hirasaki (2009) does not involve a flow reversal, but merely a change of boundary condition, but even so, the analogies apply. Some of the results of Hirasaki (2009) time-varying boundary condition problem have been explained in the next section.

3.1 Application of fractional flow theory to time-varying boundary condition

The foam flows considered previously were all with constant initial conditions and boundary conditions which resulted in saturation changes (waves) originating from the origin of the (x_D, t_D) plane with trajectories of constant saturation. The question is, what will happen if there is a step change in the boundary condition, say at some time t_1? In other words, what happens if during injection, the injection conditions were changed in the midst of the displacement; e.g. changing from an injection condition giving a spreading wave to one giving a shock?

As a first sight, this question appears very complex, because generally speaking, during fluid displacement in porous media, the solution can be represented by a set of "characteristic" lines (i.e. lines of constant liquid saturations in a distance-time plot) which are only launched from the origin in the x_D, t_D plane when constant initial and bound-

ary conditions are considered, but under more general conditions, "characteristics" can collide in the time–distance plane, in which case they set up a new fractional-flow problem where the rearward characteristic in effect represents an injection condition and the forward characteristic represents an initial condition (Rossen et al., 1994). Then, the resulting solution propagates possibly with a discontinuity present until it becomes complicated by other effects e.g. merging with another discontinuity. This is in agreement with the study of Courant and Friedrichs (1999b). In their work, the authors stated that ordinarily if the beginning of a fluid flow is of a simple nature, a fairly complete analysis of subsequent stages of the motion characterised by the interaction of initial elementary waves originating from a state of rest and contact discontinuities can be achieved, but that in many cases, the system moves initially in elementary waves, separated from each other, and that what happens shortly afterwards is that such waves become reflected, meet or overtake one another.

Hirasaki (2009) considered this complex case (that is a case of change in boundary condition only, albeit without flow reversal or a change in flow direction) and found out that, when the boundary condition differs from the initial condition but later is changed back to the same condition as the initial condition at time $t = t_1$ say, there is a spreading wave (i.e. a wave that upon propagation, neighbouring saturation values become more far apart) from the new boundary condition (BC) to a certain liquid saturation value say $S_w = S_{w1}$ (see figure 3.4). Then a shock also goes from S_{w1} to the old boundary condition (BC) as shown in figure 3.3. This shock, the author called "back shock" in order to differentiate it from the "front shock" further downstream as shown in figure 3.4. The front shock goes from the initial condition IC to a S_w value on the fractional flow curve (see figure 3.3), typically higher than S_{w1} but lower than the original BC.

As time evolves, the lowermost S_w value on the back shock increases (to a value S_{w2} say greater than S_{w1}) and the uppermost S_w value on the back shock decreases (it falls below the old BC) as shown in figure 3.3. In other words, the (low) saturation S_w upstream of the back shock rises with time and the (high) saturation S_w downstream of it falls. The speed of the back shock increases. This follows because as the back shock travels, the saturation of the old boundary condition is no longer relevant since the back shock overtakes the slower waves. This is possible because the velocity of the back shock is greater than the velocity of the wave at the saturation of the old boundary condition which is actually zero here (as can be observed in figure 3.4). Once we know the (high) saturation downstream of the back shock we also know the (lower) saturation upstream of it, as this is given by matching the shock speed to the speed of the upstream characteristic. The back shock moves sufficiently quickly that it eventually catches up with the front shock, meaning the two shocks merge into a single one. Downstream of the single shock, S_w is at the initial condition IC value. Upstream it inherits the S_w values that were upstream of the back shock. The single shock can be tracked over time and the S_w values upstream of it fall as time evolves. In the limit of arbitrarily long times (long after time t_1) a state is restored in which S_w is uniformly close to the initial condition, i.e. at very long times it is as if the period up to time t_1 (when the BC and IC differ) never actually took place.

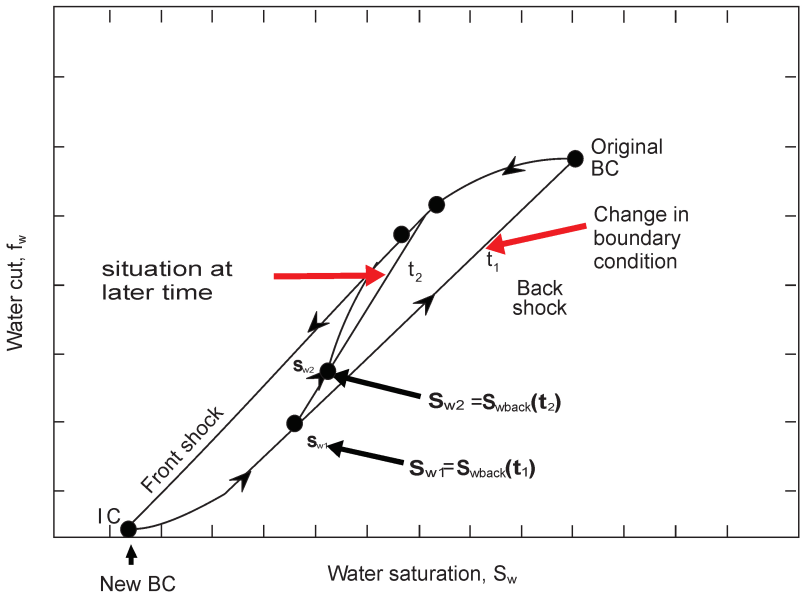

Figure 3.3: Fractional-flow curve for a change in boundary condition. There is a spreading wave from the new BC to S_{w1} (upstream of the back shock when it first appears). There is also a front shock going from an initial saturation to a value that is higher up. Furthermore, there is a back shock that goes from an S_{w2} value at t_2 to a value less than the original BC. Overtime, the jump in saturation across the back shock decreases and the two shocks become close together as shown in figure 3.5 and eventually become one. (Adapted from (Hirasaki, 2009)).

A dimensionless distance–time diagram (see figure 3.4) shows the change in the velocity of the back shock as a trajectory with changing slope. There is a continual change in the velocity and saturation behind the back shock as the back shock encounters different saturations ahead of it. A succession of short straight line segments where the slope and saturation behind the shock is re-calculated once the back shock encounters the next increment in saturation immediately ahead of it can be used to calculate the back shock numerically (Hirasaki, 2009).

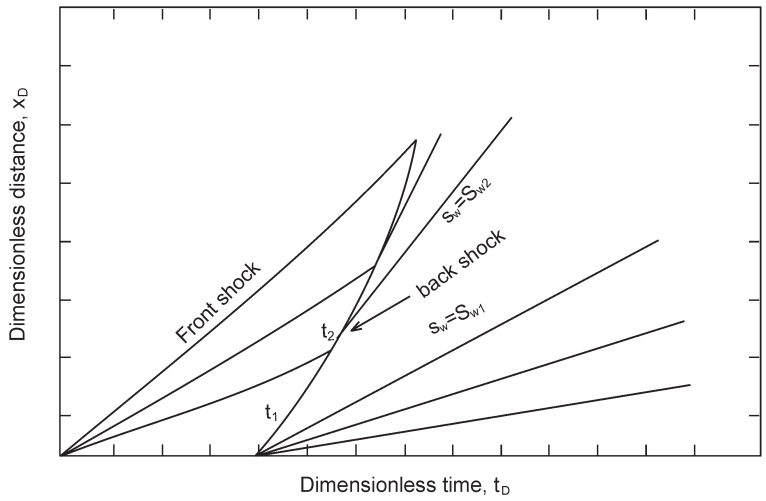

Figure 3.4: Distance-time diagram for a change in boundary condition. The trajectory of $S_w = S_{w2}$ is tangent to the trajectory of the back shock at $t = t_2$. Saturation equals initial saturation downstream of the front shock but is higher upstream of the front shock, and even higher still downstream of the back shock. There is a low saturation upstream of the back shock (Adapted from (Hirasaki, 2009)).

The saturation profile in figure 3.5 (at some fixed time) shows a continuous increase in the saturation behind the back shock before a jump to a higher saturation value, and then a continuous decrease to a certain saturation value, and finally jumping back at the front shock to the initial condition value. According to Hirasaki (2009), this happens because the back shock eats into the original waves and creates new saturation values behind it. This new saturation value upstream of the back shock has equal velocity as the back shock itself at the time the saturation value in question appears (meaning on figure 3.4, the characteristic is tangent to the shock), and this situation continues until the front shock is overtaken by the back shock. Thereafter, as we have said only one shock exists, and the saturation ahead of (i.e. downstream of) it equals the initial condition (IC). There will however be a continuous change in the saturation behind the shock as well a change in the velocity of this shock. As we have mentioned also, in the limit of arbitrarily long times, the system asymptotes back to a uniform saturation state.

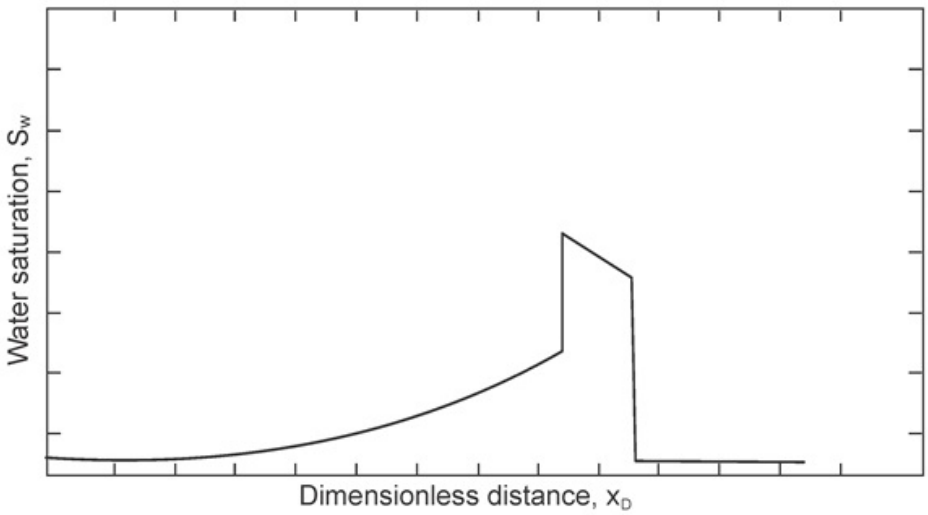

Figure 3.5: Saturation profile for a change in boundary condition (Adapted from Hirasaki (2009)).

3.2 Relevance of Hirasaki's work

Section 3.1 on Hirasaki's work was considered in this study because, it is somewhat analogous to the problem that this study aims to solve. The difference between Hirasaki's work and this work is that while Hirasaki (2009) considered just change in boundary condition without a change in flow direction, this study has attempted to consider a case that involves change in flow direction or flow reversal. In other words, Hirasaki (2009) only considered a variable boundary condition (and hence a non-trivial initial condition taken at the instant the boundary condition is varied), while this research considers a non-trivial initial condition caused by change in flow direction (i.e. flow reversal). If however we change the sense of the coordinate system at the instant as we reverse the flow, we also in effect change the upstream boundary condition, since what was formerly downstream has now become upstream. The procedures employed in solving a flow reversal problem are described in the section and subsections to follow. The solution to the flow reversal problem considered in this thesis is then explained in the next chapter.

3.3 How to approach a flow reversal problem

To solve the flow reversal problem posed above, the data of Shi (1996) (see table 3.1) and the relative permeability functions in equations (2.59)–(2.63) were used. First (see section 3.3.1), fractional flow curves were constructed, and shock states for flow in both directions viz. before flow reversal, and from the point of flow reversal onward, were constructed on these curves (as seen in figure 3.6). The fractional flow curves were obtained using the fractional flow equation (2.24) and the relative permeability functions as given by the fixed-P_c* model (or more precisely the progressive collapse variant thereof) via equations (2.59)–(2.63) were used. Using the Buckley-Leverett equation and the method of characteristics shown in equation (2.41), a dimensionless distance–time (x_D–t_D) diagram (see section 3.3.2) was then constructed for normal foam injection without flow reversal as shown in figures 3.7 and 3.8. Note that the time at which flow reversal occurs was set to equal one dimensionless time unit. The shock was then tracked (section 3.4 and section 4.1) and liquid saturations S_w were determined (sections 4.2–4.3).

3.3.1 Consideration of fractional flow curves

For a SAG (foam IOR) displacement process when gas is injected following the injection of surfactant solution, the injection condition (J) is at $f_w = 0$ and hence at $S_w = S_{wr}$, and the initial condition (IC) (assuming this is the first slug of gas) would be at $S_w = 1$ (Ashoori and Rossen, 2010; Rossen et al., 2011). In this study however, it was assumed that this is not the first slug of gas (albeit there was a very large slug of surfactant after any prior gas injection took place so the surfactant slug extends an arbitrarily large distance downstream), so the initial condition (IC) is at $S_w = 0.8 = 1 - S_{gr}$. Both points

are on the foam fractional flow curve as seen in figure 3.6. For simplicity, the presence of an oil phase has been ignored here. In other words, oil even if present, is assumed to be included in the aqueous or liquid phase, since our main interest here is in describing interaction between gas and surfactant liquid at the foam front.

Table 3.1: Data used for flow reversal problem

Water saturation (S_w)	$0.20 \leq S_w \leq 0.80$
Connate water saturation (S_{wr})	0.2
Irreducible water saturation (S_{wi})	same as S_{wr} here
Limiting water saturation (S_w*)	0.37
Residual gas saturation (S_{gr})	0.2
Gas phase viscosity (μ_g)	0.018 cp
Liquid phase viscosity (μ_w)	1.2 cp
Parameter in model for gas mobility with foam (ϵ)	0.01
Parameter in model for gas mobility with foam (R)	18500

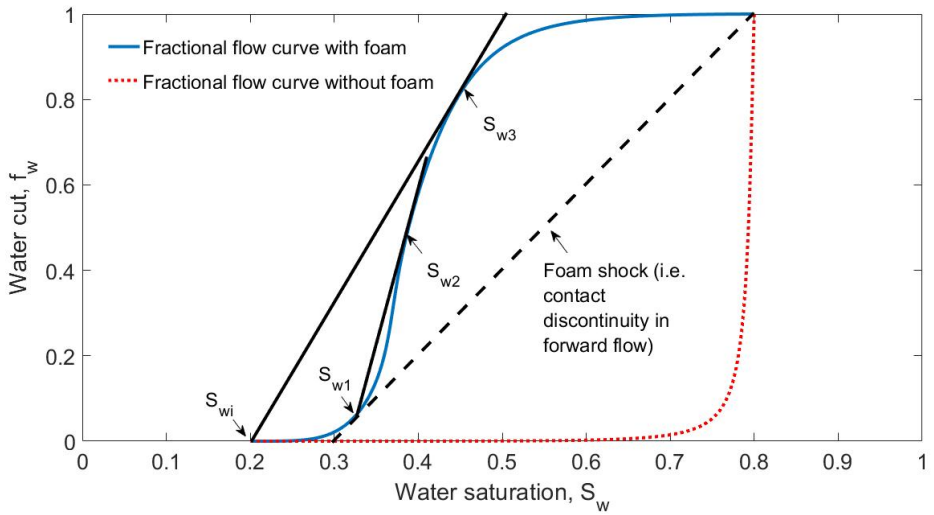

Figure 3.6: Fractional flow curve with/without foam, based on the data of Persoff et al. (1991) showing the shock graphically. $\mathrm{d}f_w/\mathrm{d}S_w$ does not increase continuously from the injection condition $f_w = 0$ or $S_w = S_{wr} = 0.2$ to the initial condition $S_w = 0.8$. Rather, at a small value of f_w, a shock goes from the initial condition (IC) to a point of tangency to the fractional flow curve. Also, for S_w values greater than S_w*, the increase in f_w turns out to be quite gradual. Around that region, it is believed that the relative permeability of water is still very low as seen in figure 2.20, and 'f_w' can only increase significantly with increasing 'S_w'

.

Initially, before flow reversal, a straight line tangent has been drawn from the initial condition ($S_w = 1 - S_{gr}$) to the fractional flow curve. This gives the point $S_{w1} \approx 0.32$ on

figure 3.6. Another point of tangency can be drawn between the injection condition S_{wr} (connate water saturation or analogously S_{wi} irreducible saturation) and the fractional flow curve. The value of the water saturation (S_{w3}) obtained at this particular point of tangency (for these data, $S_{w3} \approx 0.45$) turns out to represent the final state of the shock, long after flow reversal. This is by analogy with the findings of Hirasaki (2009) discussed in section 3.1: long after the flow reversal has occurred, the final state should be as if no initial forward flow ever took place.

During forward flow though, it is the point S_{w1} (for these data, $S_{w1} \approx 0.32$) not S_{w3}, that is relevant. At the instant of flow reversal, there has to be a continuous variation of S_w from the original injection condition up to S_{w1} (which corresponds to a relatively low f_w) but then a shock appears upstream of this ("upstream" in this context refers to upstream in the sense of the flow direction *after* flow reversal). To capture a flow reversal situation completely along with this upstream shock, another point of tangency has been drawn from the relatively low f_w at S_{w1} to a higher f_w value on the fractional flow curve as shown in figure 3.6. The liquid saturation value (S_{w2}) obtained at this point of tangency (for these data, $S_{w2} \approx 0.396$) represents the saturation upstream of the foam shock front, at least at the instant of flow reversal. Upon flow reversal when we start pushing water into gas (instead of vice versa), it is expected that upstream we might encounter water or liquid saturations that can be anything from $1 - S_{gr}$ (where S_{gr} is residual gas saturation) down to a value S_{w2} at the shock front, which exceeds the value (S_{w1}) downstream of the shock. The slope of the line joining S_{w1} and S_{w2} on the fractional flow curve gives the speed of the shock, and by construction it has the same speed as a characteristic with liquid fraction S_{w2}.

As the shock starts to move, it encounters both at its downstream end and at its upstream

end a different set of liquid saturations (i.e. characteristics with different slopes). With this, it is expected that there will be time-varying liquid saturations on either side of the shock – on both the high saturation side and the low saturation side of the shock. As we will see, it turns out that S_w decreases with time on the low saturation side of the shock, but increases with time on the high saturation side: on the low saturation side in fact S_w at the shock falls with time from S_{w1} towards S_{wr} whereas on the high saturation side immediately upstream of the shock S_w rises from S_{w2} towards S_{w3}. Moreover, away from the shock itself S_w varies continuously (with x_D at any specified t_D) from $1 - S_{gr}$ down to the S_w on the high saturation side of the shock, and also from S_w on the low saturation side of the shock down to S_{wr}.

3.3.2 Constructing dimensionless distance-time diagrams

Using equation (2.50), a dimensionless distance versus dimensionless time (x_D–t_D) diagram before flow reversal has been constructed as seen in figure 3.7. This now needs to be modified discarding any S_w values that exceed S_{w1} as these are not relevant to forward flow: this is done in figure 3.8. Note that distance as used here and also throughout the thesis with respect to the (x_D–t_D) diagram is actually the position in the 1-D space, which translates into a curvilinear position in the 2-D space when considering the associated pressure-driven growth model (see chapter 5).

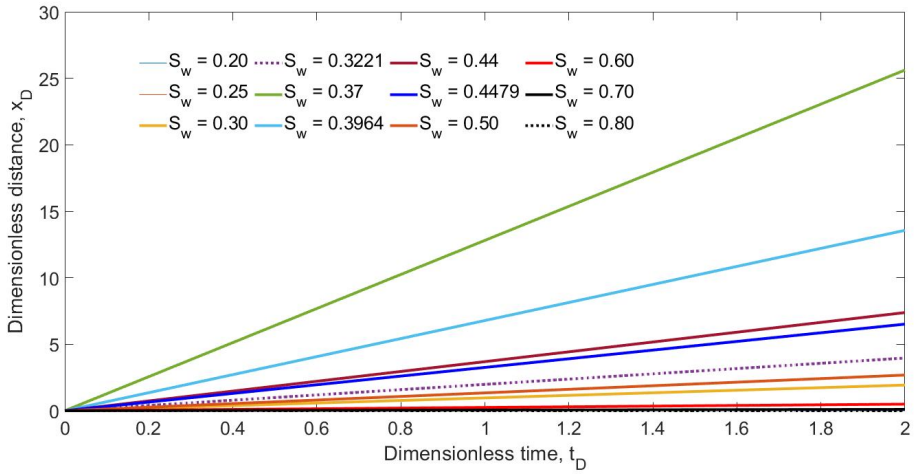

Figure 3.7: x_D–t_D diagram showing characteristic fan (for pushing gas into water initially) before flow reversal. Initial condition IC: $t_D = 0$, $S_w = 0.8$. Boundary condition: $x_D = 0$, $S_w = 0.2$. At $S_w = 0.3221$, there is a contact discontinuity (i.e. the liquid saturation value at which S_w jumps to $1 - S_{gr}$). x_D–t_D diagrams showing characteristics with comparatively lower and higher saturations are shown in figures 3.8 and 3.9 respectively.

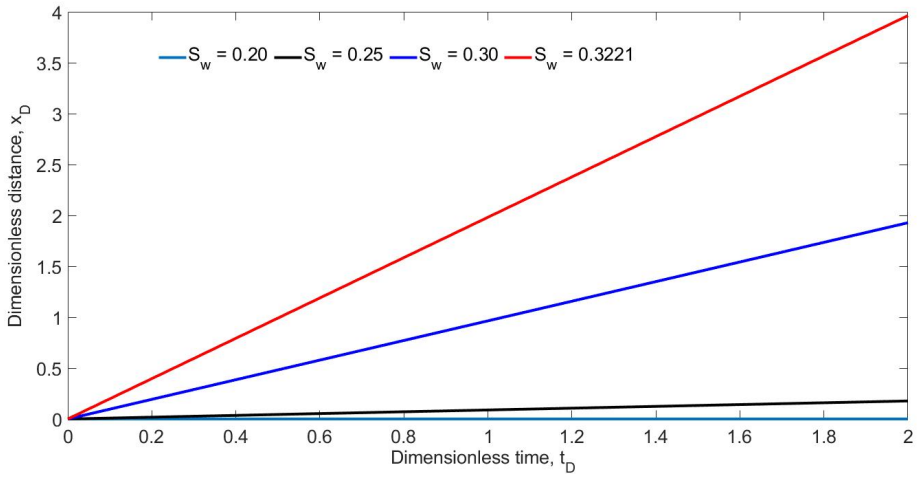

Figure 3.8: x_D–t_D diagram before flow reversal showing characteristics immediately upstream of the shock with low S_w values (that is, foamed gas with a small amount of water).

This now needs to be matched with what happens after flow reversal. We know that after flow reversal comparatively high liquid saturations become relevant. Hence in figure 3.9, an analogous x_D–t_D diagram corresponding to high saturations has been drawn.

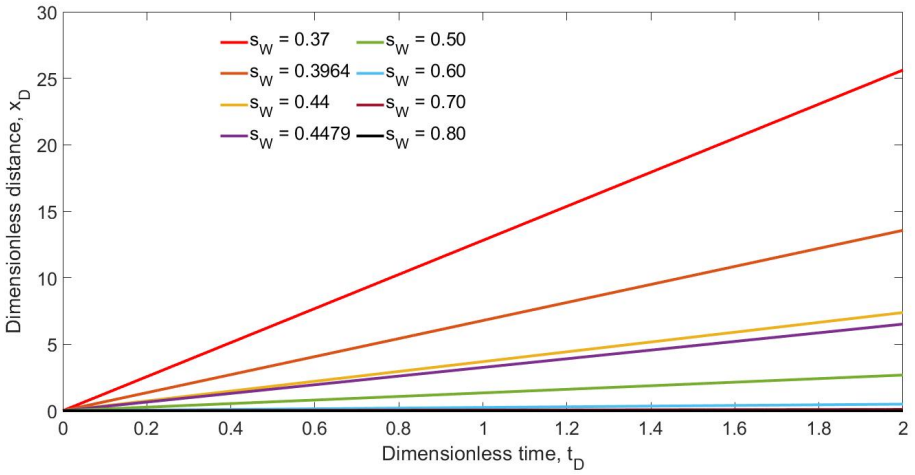

Figure 3.9: x_D–t_D diagram showing characteristics with high 'S_w' (that is water with a small amount of foamed gas, or in other words pushing water into foamed gas, rather than pushing foamed gas into water). In reality, none of these high S_w values are needed to solve the forward flow problem. They are only needed to solve the backward (reversed) flow problem. This is because in forward flow there is a constant discontinuity between $S_w = 0.3221$ and $S_w = 0.8$.

.

The imposition of flow reversal can be viewed as flipping the direction of the coordinate system of the x_D–t_D diagram (so that the positive x_D and negative x_D axes now correspond to backward or reverse flow and forward flow respectively). This now gives a new initial condition corresponding to the process of injecting water into foamed gas with a small amount of water.

In the problem of interest here, a characteristic fan similar to what is seen in figure 3.9 is now expected but with a number of modifications. Firstly, it should no longer be initiated at $x_D = t_D = 0$, but instead at $t_D = 1$ (the instant of flow reversal) and at whatever x_D value the shock itself initiates, specifically at $x_D = -f'_w(S_{w1})$. Secondly, only values of S_w between S_{w2} and $1 - S_{gr}$ are relevant: values of S_w smaller than S_{w2} are not relevant in this particular fan.

Thus, in the problem of interest here, in the coordinate system we choose, equation (2.50) can be expressed prior to flow reversal as:

$$x_D(S_w) = -f'_w(S_w)t_D; \qquad t_D < 1 \tag{3.1}$$

Then, to represent a reflection of the characteristics from the above equation, post-flow reversal, equation (3.1) becomes:

$$x_D(S_w) = -f'(S_w)(2 - t_D) = f'(S_w)(t_D - 2); \qquad t_D \geq 1 \tag{3.2}$$

The characteristic fans for both functions $t_D < 1$ and $t_D \geq 1$ are shown in 3.10.

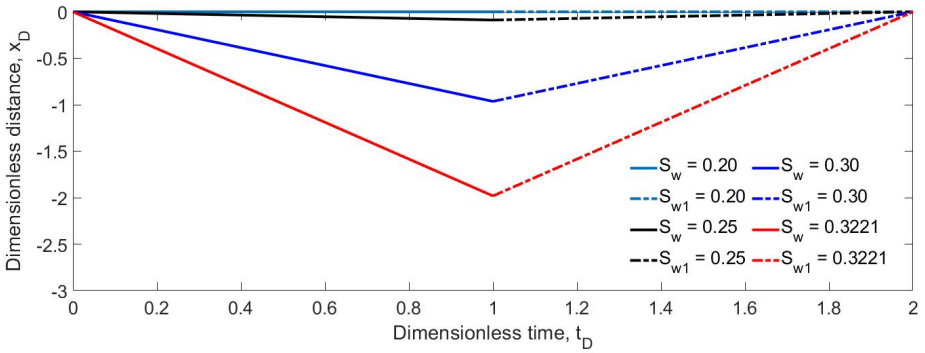

Figure 3.10: x_D–t_D diagram up to and beyond the instant of flow reversal showing characteristics initially upstream of the forward moving shock (low S_w) and its reflected characteristics, which are downstream of the reverse moving shock. Here S_w is $S_{w1} = 0.3221$ at the contact discontinuity. The S_w values here represent the saturation values that correspond to the original characteristic fan, whereas the dashed lines indicate reflected characteristics of the same S_w values.

.

Similarly, for the characteristic upstream of the shock (i.e. the high saturation side of the shock), equation (2.50) can be expressed as:

$$x_D(S_w) = -f'_w(S_{w1}) + f'_w(S_w)(t_D - 1) = -f'_w(0.3221) + f'_w(S_w)(t_D - 1); \qquad t_D \geq 1 \tag{3.3}$$

Notice that for these high saturation characteristic, the equation above has not been considered for $t_D < 1$. This is because, this fan only appears after the time of flow

reversal which is at $t_D = 1$. The characteristics for the function expressed in equation (3.3) which represent the high saturations appearing after the instant of flow reversal have been added to figure 3.11. The overall solution to the flow reversal problem will ultimately depend on the interaction between the two characteristic fans obtained from equations (3.1)–(3.3). It is in order to understand this interaction, that the two fans have been superimposed as shown in figure 3.11.

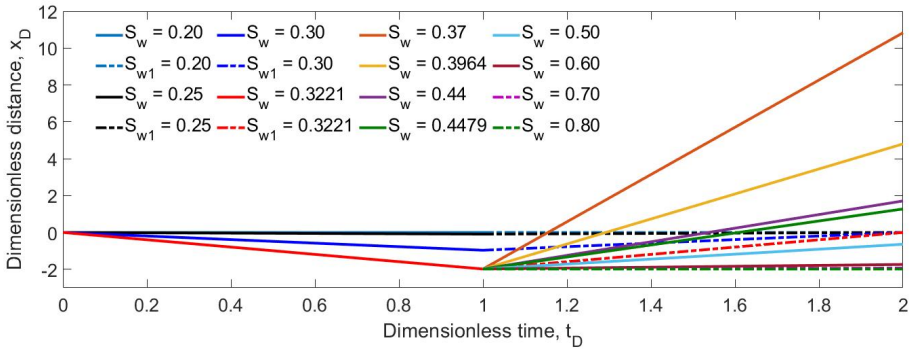

Figure 3.11: $x_D - t_D$ diagram showing the interaction between the two fans.

It can be seen from figure 3.11 that in the region in which the two fans overlap, there could be at any (x_D, t_D) value, two liquid saturation values: one for each fan. The smaller saturation values (from $S_w = 0.20$ to $S_{w1} = 0.3221$) represent the saturation values upstream of the forward-propagating shock, while those shown with dashed lines represent the reflection of the same set of saturation values (downstream of the flow reversed shock). Then the higher saturation values (from $S_w = 0.37 \equiv S_w{}^*$ or strictly speaking from $S_{w2} = 0.3964$ up to 0.80) represent the saturation values upstream of that shock. In reality S_w cannot be double valued at all (x_D, t_D) values in the domain, only at a well defined locus of x_D vs t_D values corresponding to a shock. From the above, if the position of the shock is known at any instant in time, the characteristic fans ahead of and behind the shock can be used to figure out water saturations either side of the shock. On the other hand, if the water saturations either side of the shock are known, we can also predict the instantaneous migration velocity of the shock as explained next.

3.4 Shock migration in a reversed flow condition

As stated in the previous section, if the position of the shock is known at any instant in time, the characteristic fans ahead of and behind the shock can be used to figure out water or more generally liquid saturations either side of the shock. Then using Rankine-Hugoniot condition or integral mass balance (Rankine, 1870; Courant and Friedrichs, 1948; Bedrikovetsky, 2013), how fast the shock moves, and thereby where the shock is at a later time can also be determined. The Rankine-Hugoniot jump condition is a mathematical equation that describes the relationship between the states on both sides of a shock wave in a one-dimensional fluid flow. In its simplest form as applicable to this work, it is analogous to equation (2.54) and can be rewritten as:

$$\frac{\mathrm{d}x_D}{\mathrm{d}t_D} = \frac{f_w(S_w^+) - f_w(S_w^-)}{S_w^+ - S_w^-} \tag{3.4}$$

where $\mathrm{d}x_D/\mathrm{d}t_D$ is the shock speed, $f_w(S_w^+)$ is the fractional flow of the high liquid saturation value, $f_w(S_w^-)$ is is the fractional flow of the low liquid saturation value, S_w^+ and S_w^- are the high and low liquid saturation values respectively. An algorithm can now be obtained for propagating the shock and solving the flow-reversed system.

3.4.1 Algorithm for calculating shock position and speed

The algorithm is summarised in figure 3.12. The starting point is via the construction of the x_D–t_D diagram. To do this, fractional flow curves are first constructed (see figure 3.6). The saturation at the shock and fractional flow is determined by solving for a point of tangency to the f_w curve for a line passing through the point $(S_w, f_w) = (0.8, 1)$. The liquid saturation S_{w1} at the point of tangency represents the saturation at the shock front

for forward flow. Then a line is drawn from this point to find another point of tangency on the fractional flow curve (at S_{w2}). The saturations at either end of this latter line gives the liquid saturations across a shock at the instant of flow reversal. As stated previously, the two liquid saturations either side of this shock, correspond to a low liquid saturation side and a high liquid saturation side. Construction of the x_D–t_D diagram then shows characteristic fans for forward and reversed direction superimposed on each other as seen in figure 4.1.

Then, to locate the position of the shock at any instant of time, an initial time (dimensionless time t_D in this case) at which flow reversal takes place is first chosen. The corresponding position (x_D coordinate) of the shock is then read off from the x_D–t_D diagram. Once, that is known, the liquid saturations on either side of the shock can be determined: if we know where the shock is in x_D–t_D space we can determine the liquid saturations on the characteristics passing through that point. The speed of the shock can then be calculated using equation (2.54) or equivalently equation (3.4). To update the position of the shock for both liquid saturations on either side of shock (i.e. low liquid saturation and high liquid saturation values), equations (3.2) and (3.3) can be used respectively, and the process is repeated again.

The algorithm changes after x_D crosses over $x_D = 0$. The shock has now propagated at least as far during the reverse flow phase as it propagated during the initial forward flow. In that case, the liquid saturation downstream of the shock becomes the connate water saturation S_{wr} and remains at that value. It is then only necessary to find S_w on the upstream side of the shock. The final S_w value at the upstream side of the shock in the long time limit can be obtained by solving for the point of tangency to the f_w curve passing through the point $(S_w, f_w) = (0.2,0)$.

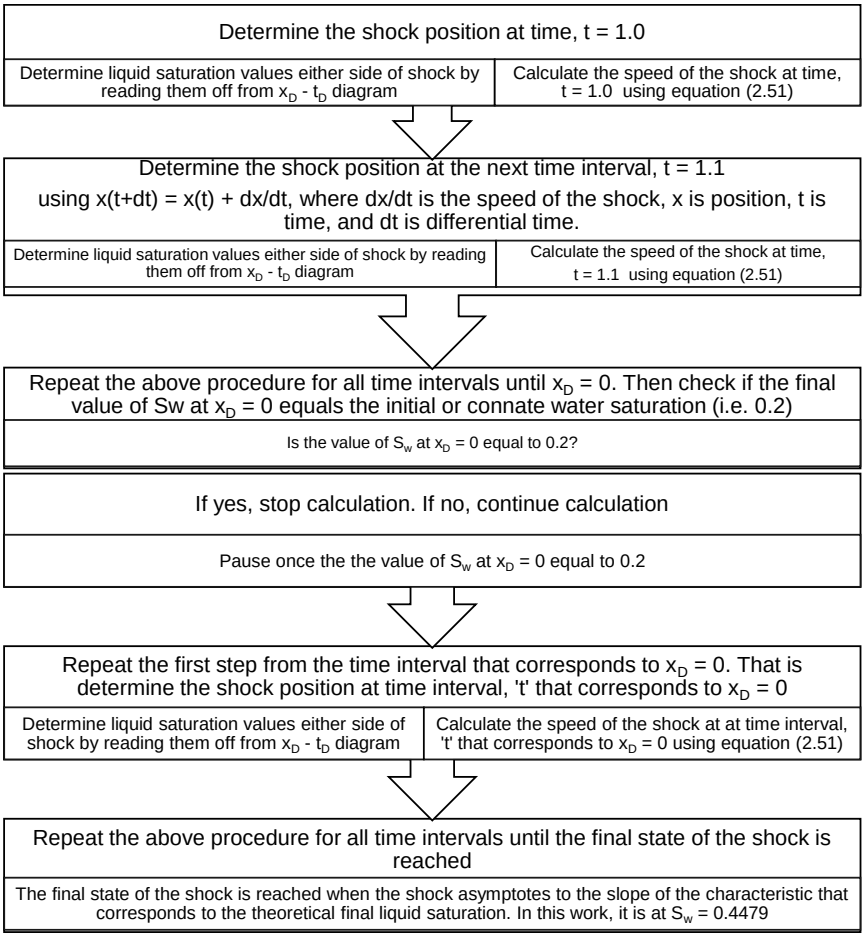

Figure 3.12: Algorithm for determination of shock position, liquid saturation values either shock of shock, and shock speed. The algorithm was implemented in MATLAB.

As stated above, the algorithm undergoes a change once the shock position reaches $x_D = 0$. After this point, it is expected that the saturation value downstream of the shock (low saturation value) will be equal to the connate water saturation (i.e. $S_w = 0.2$). Figure 4.1 shows an x_D–t_D diagram with the position of the shock and its migration determined up to $x_D = 0$. **Table A.1** shows the results up to $x_D = 0$ as calculated by MATLAB. Figure 4.2 shows an x_D–t_D diagram with the position of the shock determined from $x_D = 0$ to later time and final state of the shock. **Table A.2** shows the results from $x_D = 0$ to final state of shock as calculated by MATLAB. The final saturation on the high liquid saturation side of the shock turns out to be $S_{w3} = 0.4479$. Results obtained from the

algorithm described above are presented in the next chapter.

Chapter 4

Results and Discussion

This chapter discusses the results of this work, highlighting key features of what the results indicate.

4.1 Shock propagation

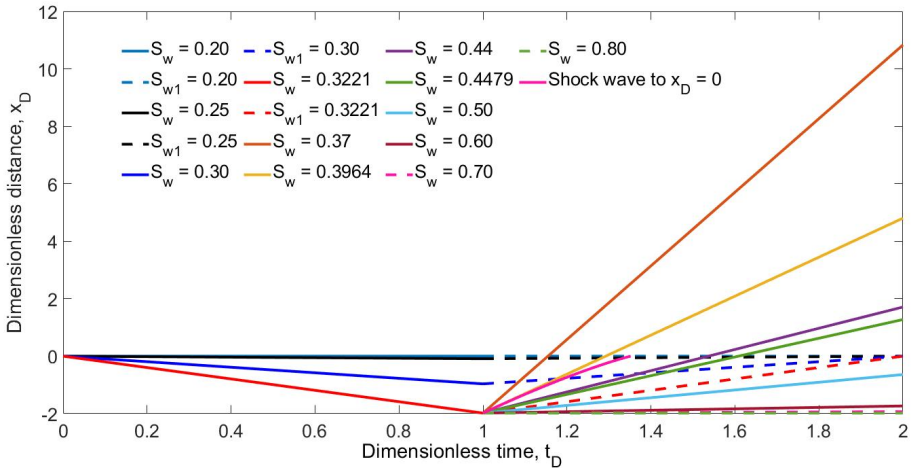

Figure 4.1: x_D–t_D diagram showing shock position up to $x_D = 0$. After flow reversal (at time $t_D = 1$), ahead of the shock, there will be low S_w values (that is foamed gas with a small amount of water; initially $S_w = 0.3221$ there). Behind the shock, there will be high S_w values (that is water with a small amount of foamed gas; initially $S_w = 0.3964$ there). As the shock evolves with time, the spatial domain of varying liquid saturations behind the shock (i.e. upstream) will increase while the spatial domain ahead of it and the set of saturations ahead of it also (i.e. downstream) will decrease.

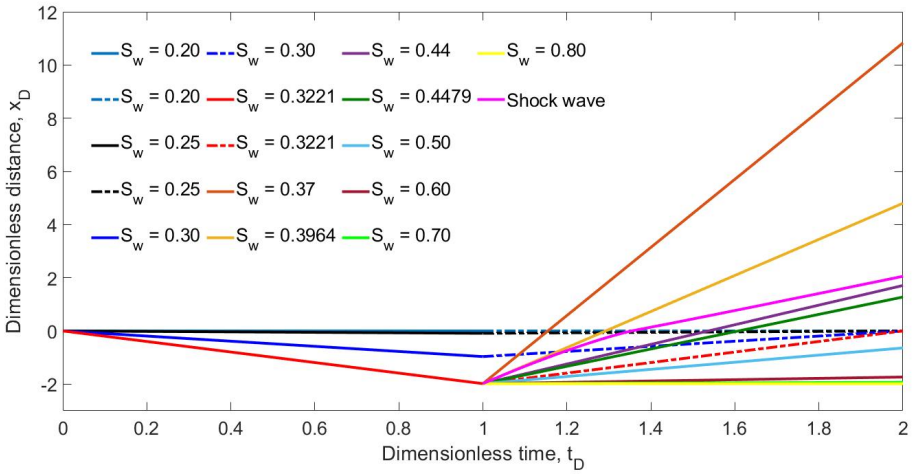

Figure 4.2: x_D–t_D diagram showing shock position up to the final state of the shock when the shock asymptotes to the slope of the characteristic that corresponds to the theoretical final liquid saturation (i.e. $S_w = 0.4479$).

Figures 4.1 and 4.2 show dimensionless distance versus dimensionless time (x_D–t_D) diagrams for a flow reversal process for the domain up to $x_D = 0$ (that is when the shock reaches the position, $x_D = 0$ in the 1-D space) and also beyond $x_D = 0$. They both show that the upstream liquid or water saturation on the shock at the instant of flow reversal starts at a liquid saturation of $S_w = 0.3964$ at a distance of $x_D = -1.9820$, while the downstream liquid saturation on the shock at the instant of flow reversal at the same distance starts at a liquid saturation of $S_w = 0.3221$. These values can also be seen in **figures 4.3** and **4.4** respectively that shows how the saturations associated with the shock evolve over time.

The physical implication of the shock crossing $x_D = 0$ is that it (the shock) has now managed to backtrack and cover the actual distance the forward flow (i.e. the flow before flow reversal) actually covered. In our system this $x_D = 0$ crossover happens at a time of $t_D = 1.354$ and is an indicator that going forward there would be a change in the system with respect to how S_w varies with x_D. This change can be determined by examining the characteristic lines shown in figures 4.1 and 4.2 at some fixed times. The results

will yield saturation profiles at any fixed time as shown in figures 4.6. It is noteworthy to mention here that it is actually at the same time that the shock crosses $x_D = 0$, that the low saturation side of the shock also falls to the irreducible water saturation mentioned above. This happens at a t_D of 1.354 as stated above. The corresponding liquid saturation at the upstream of the shock at this particular time is ≈ 0.4110.

This situation of a foam front propagating backwards further than it originally moved forwards is potentially relevant if the system is extended to 2-dimensions (2-D) where one well extracts, and others inject. As will be discussed in Chapter 5, in a 2-D system or geometry, a point near the bottom of a foam front moves forwards and downwards a little under the action of the driving pressure and stops when the driving pressure is balanced by hydrostatic pressure.
If the driving pressure is then reduced, the point moves backwards and upwards, coming to rest at a different height at which the reduced driving pressure balances hydrostatic pressure. If the amount of original forward motion is small, because the point was near the bottom of the original front, the distance it moves backwards and upwards can exceed the original forward motion.

As the shock moves over time, the values of water or liquid saturations behind the shock (i.e. upstream) increases, while the water saturation ahead (i.e. downstream) of the shock decreases until it reaches an irreducible water saturation; in this study $S_w = 0.2$ (see **figure 4.5**). In other words, as the shock migrates, it encounters downstream of it foam with less and less water. This makes sense as the shock is moving towards a gas filled region downstream. It can be seen in **figure 4.3** that around the point at which $x_D = 0$, there is a fairly sharp change in the slope of (i.e. speed of) the shock.

Furthermore as the shock propagates and passes $x_D = 0$, the S_w value on the high saturation side of the shock keeps increasing over time, but the shock itself never quite reaches a speed, i.e. a slope in **figure 4.3** as high as the speed/slope of characteristics immediately behind the shock. After the shock passes $x_D = 0$, there will be only gas with irreducible liquid ahead of the shock and whilst far enough behind the shock there will be uniform aqueous phase (or more specifically aqueous phase with irreducible gas). Eventually, the long time state of the shock will be more or less the same state we would obtain if water had been injected into foamed gas from the outset without any initial period of injecting foamed gas into water as the shock asymptotes to the slope of the characteristic that corresponds to the theoretical final S_w value on the high saturation side of the shock of 0.4479.

4.2 Evolution of saturations associated with the shock

Figure 4.3 shows the evolution of saturation (S_w vs t_D) for the range of saturation values that occur immediately behind the shock (i.e. the high saturation values). **Figure 4.4** is a zoomed out view.

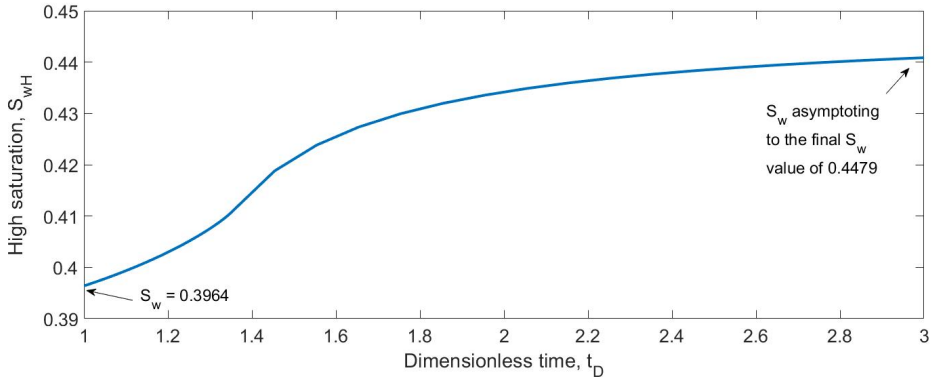

Figure 4.3: Saturation evolution for S_w values on the high saturation side of the shock, starting at the initial value on the shock $S_w = 0.3964$, evolving over time and approaching the final liquid saturation value ($S_w = 0.4479$) asymptotically as can also be seen in the x_D-t_D diagram in figure 4.9.

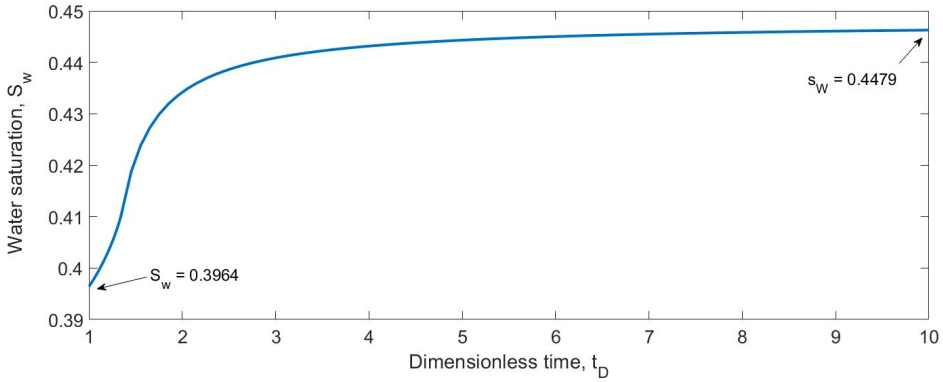

Figure 4.4: Zoomed out view of figure 4.10 showing S_w values asymptoting to the final S_w value of 0.4479.

Figure 4.5 shows a saturation profile (S_w vs t_D) for the range of saturation values immediately downstream of the shock (i.e. the low saturation values). Starting from a value 0.3221, over time S_w falls to 0.2, and then remains fixed at that value.

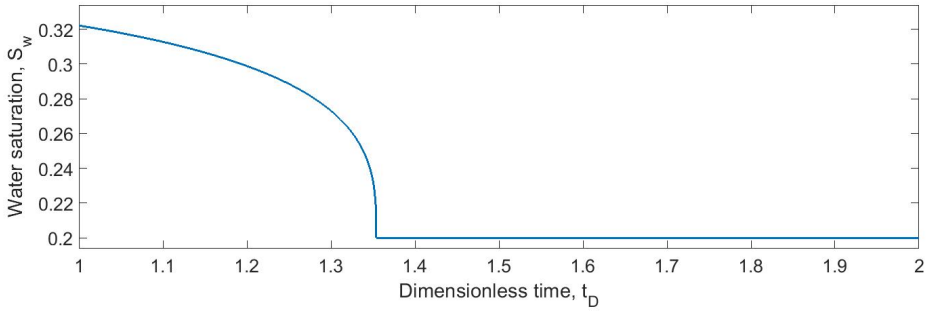

Figure 4.5: Saturation evolution for S_w values on the low saturation side of the shock starting at the value of S_w for the contact discontinuity (i.e. $S_w = 0.3221$) before falling to the initial water saturation of 0.2 and remaining there over time.

.

Figures 4.3–4.4 and 4.5 show the evolution of saturation with time for the range of saturation values upstream (high saturation values) and downstream (low saturation values) of the shock respectively. Saturation values upstream of the shock grow over time, but change slowly at first. This is because in the x_D–t_D plane, the shock starts off parallel to the characteristic immediately upstream of it, and it is only as the shock direction in the x_D–t_D plane itself starts to change that the shock manages to cross any of the upstream characteristics (and it is only by crossing those characteristics that the upstream S_w manages to grow).

The value of S_w upstream of the shock increases further as it approaches the time at which $x_D = 0$, after which it continues to increase, but at a lesser rate and approaches the final liquid saturation value asymptotically as can be seen in **figure 4.4**. Also, the saturation values downstream of the shock migrate to lower saturations as the shock moves. In addition, on the approach to $S_w = 0.2$ (irreducible saturation), there is a fairly abrupt change in this downstream S_w with time as seen in **figure 4.5**. This follows since, via equation (3.2), characteristics obey $x_D = f'_w(S_w)\,(t_D - 2)$, and there is a significant domain of S_w values with $f'_w(S_w)$ very small (see figure 3.6) and hence with x_D very close to zero: despite the significant variation in S_w, given that we are considering a domain in which x_D values are all very small, the shock moves through it very rapidly. Saturation profiles at selected times have been plotted below.

4.3 Saturation profiles at various times

Figure 4.6 shows saturation profiles S_w vs x_D at specific times viz. $t_D = 1.2$ and $t_D = 1.6$ respectively.

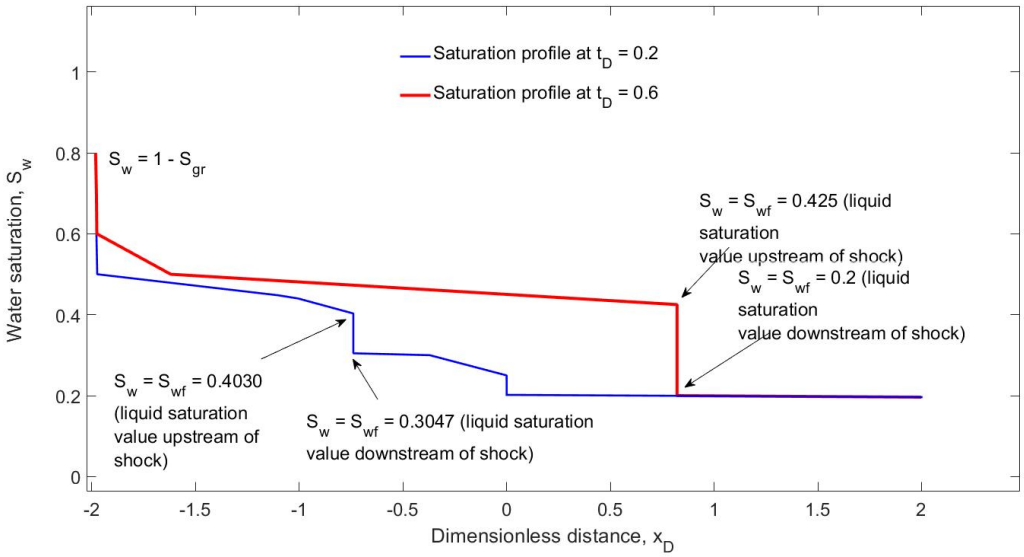

Figure 4.6: Saturation at specific times, $t_D = 1.2$ and $t_D = 1.6$

.

Figure 4.6 show saturation profiles S_w vs x_D at $t_D = 1.2$ and $t_D = 1.6$ respectively. The profiles represent how the saturation profile behaves at a time ($t_D = 1.2$) even before the shock reaches $x_D = 0$ (that is at a time corresponding to $x_D < 0$), and at a time ($t_D = 1.6$) after the shock has crossed $x_D = 0$ (that is $x_D > 0$). These were constructed by extracting data at any given time from figures 4.1–4.5. In the former case (that is $t_D = 1.2$), as the shock moves towards $x_D = 0$, the liquid saturation (S_w) falls continuously from 0.8 down to about 0.4, then jumping at the shock (specifically from $S_w = 0.403$ on the upstream of the shock and $S_w = 0.3047$ on the downstream side) at x_D value of -0.7393 to a S_w just above 0.3 before continuously falling to 0.2. The final approach to $S_w = 0.2$ is very steep, albeit not actually a shock.

As for the latter case ($t_D = 1.6$), as the shock moves past $x_D = 0$ (that is $x_D > 0$), the liquid saturation (S_w) versus position x_D behaves as follows. At $t_D = 1.6$, S_w falls continuously from 0.8 down to about 0.43, then jumps at the shock (i.e. from $S_w = 0.425$ on the upstream of the shock to $S_w = 0.2$ on the downstream side) at an x_D value of 0.8214 to $S_w = 0.2$.

A graph of the shock velocity against dimensionless time is shown in figure 4.7.

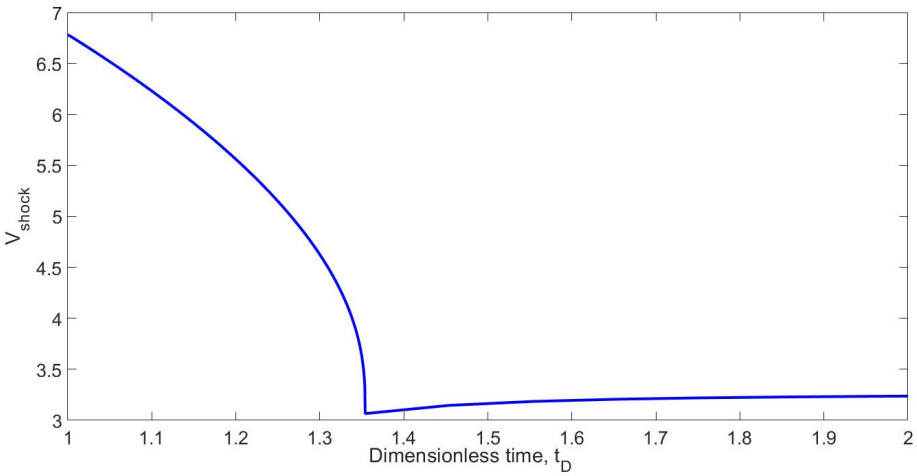

Figure 4.7: Velocity time graph for the shock. The velocity was high at first, falls, and subsequently rises slightly.

Figure 4.7 shows a strong deceleration of the shock up to the time at which the dimensionless distance x_D equals zero (i.e. between $t_D = 1$ and $t_D = 1.354$), and a slight acceleration of the shock just after that point. The acceleration is just slight though. This is because there is a limit to which it can accelerate as the system asymptotes to a certain liquid saturation value (in this case $S_w = 0.4479$) at which with the speed of the shock equals the speed of a characteristic corresponding to $S_w = 0.4479$. Note that except at the instant of flow reversal, the shock can no longer be determined as a point of tangency to the fractional flow curve, but rather is the result of characteristics colliding with the shock from both behind and in front.

On the one hand, the deceleration is caused by the liquid saturation on the downstream (low saturation) side of the shock decreasing over time. In a f_w vs S_w plot such as figure 3.6, the slope of the line joining the high and low saturation ends of the shock (which corresponds to the velocity of the shock) therefore must decrease. On the other hand, the subsequent acceleration occurs once the S_w value at the low saturation end of the shock has reached the irreducible saturation S_{wr} (0.2 in our system) and stays fixed at that value. The liquid saturation on the upstream (high saturation) side of the shock manages to increase though; at this point, the only relevant fan is the one on the upstream (high saturation side) of the shock, and the shock migrates from characteristic to characteristic within this fan. In this case, in a f_w vs S_w plot such as **figure 3.6**, the slope of the line joining the high and low saturation ends of the shock now increases with time.

The final velocity of the shock in the limit as $t_D \to \infty$ corresponds to the liquid or water saturation value at which $f'_w(S_w) = f_w(S_w)/S_w$, so becomes tangent to the fractional flow curve again. In addition, for $t_D \to \infty$, the original forward flow prior to flow reversal will

no longer have an effect on the solution as the reversed flow has gone on for long enough time that any initial forward flow is now negligible.

This completes the presentation of the set of results from fractional flow with flow reversal. In the next chapter we discuss and analyse these results.

To summarise, the understanding gained from analysing the 1-D fractional flow results under flow reversal, as has been done here, has been implemented in a published article (see chapter 5). As that article explains, proper understanding of the 1-D flow reversal results enables us to extend the models of flow reversal towards higher dimensions (2-D or even 3-D). Note that (as mentioned in chapter 5) the article was implemented with a different set of fractional flow parameter values from those used here, so the numerical values reported differ, although the general findings match up.

Chapter 5

Published Paper

This chapter is a paper published by the Royal Society Publishing in *Proceedings of the Royal Society A*; Volume 480, Issue 2250, 20200573, published 16 December 2020 (https://royalsocietypublishing.org/doi/10.1098/rspa.2020.0573). It presents an extension to higher dimension (2-D in this case). Note that the parameter values used here differs slightly from the ones used in the thesis.

In the published paper, slightly different parameters (different from those in equations (2.59)–(2.63), in figures 2.19–2.21 and Table 3.1) in the thesis, were chosen. On the one hand, the particular parameters chosen in the thesis are not too far from Brooks and Corey (1964) and also agree with the data of Persoff et al. (1991). On the other hand, the parameters in the published manuscript were chosen to be a bit simpler than those in the rest of the thesis, without quite such big mobility contrasts for either water or for the difference between un-foamed gas and foamed gas as water saturation varies, making it easier to see on a graph how much fractional flow f_w deviates from zero (or one) when water saturation S_w (or more generally liquid saturation S_l) is close to zero (or one).

Note that equations (3.2)–(3.3) of the thesis (or equivalently equations (4.8)–(4.9) in the published paper) imply also that dx/dS_l depends on d^2f_w/dS_l^2, so dS_l/dx is proportional to $(d^2f_w/dS_l^2)^{-1}$: the value of dS_l/dx can be seen as the slope of a S_l vs x plot, at any

given time. For the values chosen in the published paper, this quantity $(d^2 f_w/dS_l^2)^{-1}$ has a well defined finite limit as either $S_l \to 0$ or $S_l \to 1$. For the parameters used in the thesis, $(d^2 f_w/dS_l^2)^{-1}$ is not so well behaved in those limits, and that impacts on the shape of the S_l vs x profiles in figure 4.6.

Some other subtleties in the published paper are flagged up below. Regarding the parameter ϵ, which measures the ratio between thickness of a low mobility foam front and front displacement distance; in a 1-D fractional flow system, it certainly occurs that the thickness of the finely textured flow front is proportional to displacement distance: that follows from the characteristic lines (lines of constant S_l) being straight in the $x-t$ plane, and mobility being a function of S_l. This carries over to a 2-D system provided the front is thin. In 2-D system, the situation is actually a bit more complicated – if the foam front ceases to be thin, it is then difficult to define through exactly what distance points near the front have displaced.

Finally, it is important to note here that the $(1 - S_{l,fwd})/(1 - f_{l,fwd})$ term in equation (4.24) of the published paper comes from the non-dimensionalisation (see equation (4.3) of the published paper). The scale for the non-dimensionalisation has been based on the forward flow phase, so, that factor arises naturally when one compares reverse and forward flow.

PROCEEDINGS A

rspa.royalsocietypublishing.org

Research

Check for updates

Article submitted to journal

Subject Areas:
Mathematical modelling, Applied mathematics

Keywords:
Pressure-driven growth, Fractional-flow theory, Foam improved oil recovery, Flow in porous media, Flow reversal, Method of characteristics

Author for correspondence:
P. Grassia
e-mail: paul.grassia@strath.ac.uk

THE ROYAL SOCIETY PUBLISHING

Modelling Foam Improved Oil Recovery: Towards a Formulation of Pressure-Driven Growth with Flow Reversal

M. Eneotu[1], P. Grassia[1]

[1] Department of Chemical and Process Engineering, University of Strathclyde, James Weir Building, 75 Montrose Street, Glasgow G1 1XJ, UK

The pressure-driven growth model that describes the 2-D propagation of a foam through an oil reservoir is considered as a model for surfactant-alternating-gas improved oil recovery. The model assumes a region of low mobility, finely-textured foam at the foam front where injected gas meets liquid. The net pressure driving the foam is assumed to reduce suddenly at a specific time. Parts of the foam front, deep down near the bottom of the front, must then backtrack, reversing their flow direction. Equations for 1-D fractional flow, underlying 2-D pressure-driven growth, are solved via the method of characteristics. In a diagram of position vs time, the backtracking front has a complex double fan structure, with two distinct characteristic fans interacting. One of these characteristic fans is a reflection of a fan already present in forward flow mode. The second fan however only appears upon flow reversal. Both fans contribute to the flow's Darcy pressure drop, the balance of the pressure drop shifting over time from the first fan to the second. The implications for 2-D pressure-driven growth are that the foam front has even lower mobility in reverse flow mode than it had in the original forward flow case.

1. Introduction

During oil and gas production, typically only a fraction of the oil available in a reservoir can be extracted under the reservoir's own pressure. After that, fluids must be injected into the reservoir to displace the remaining oil, the direction of displacement then being from an injection well towards one or more production wells. Although various different choices of injection fluids can

be made [1–5] (e.g. water injection, steam injection, carbon dioxide injection, polymer injection, etc.), one promising candidate displacing fluid is foam [6–9], the injection process then being termed "foam improved oil recovery" or foam IOR.

One of the reasons why foam works so effectively in applications such as these is that it tends to have very low mobility [8] when moving through porous media such as oil reservoirs. This low mobility helps to suppress so called "fingering instabilities" [10] that would arise when higher mobility fluids are injected. Such fingering instabilities are undesirable in the context of foam IOR since they cause injected fluid to flow along a small selection of high permeability preferred flow paths bypassing much of the reservoir fluid originally in place. Using a low mobility injection fluid such as foam avoids this situation by allowing oil to be displaced more uniformly [11], even to the point that foam is diverted preferentially into low permeability strata which have previously been left unswept [12–14]. Indeed, as the fluid present with the lowest mobility, foam tends to control the flow of all the other reservoir fluids. It then follows that if the flow of foam can be controlled, the evolution of the entire displacement process to recover oil can also be controlled.

In view of this, it is unsurprising that there have been many studies trying to understand and/or model [15–26] how foam behaves when flowing through porous media. Models cover the full range of scales from small scale, i.e. motion of individual foam films within individual pore spaces [27–33] to larger scale, i.e. foam front displacement through a porous medium as a whole [18,19,23,24,26] up to a very large scale, i.e. an entire reservoir [20,34–39]. The smaller scale models mentioned above incorporate a high level of geometric microstructural detail. Larger scale models are unable to include all this small scale detail. Nevertheless processes occurring at one scale still manage to feed information into models at a yet larger scale.

This work is concerned with a particular reservoir scale model called "pressure-driven growth" [40–42] and a porous medium model that underlies it (so called "fractional-flow theory" [43–46]) and which feeds information to it. Pressure-driven growth in particular is used to describe a specific type of foam IOR, namely surfactant-alternating-gas or SAG [34,37,38,40,47], in which slugs of liquid surfactant solution are injected into a reservoir alternating with slugs of gas: foam is formed in situ as the injected gas meets the surfactant solution. Pressure-driven growth can be considered in 2-D (one vertical and one horizontal coordinate) or 3-D (one vertical and two horizontal coordinates): we treat the 2-D formulation here, since the generalisation of the pressure-driven growth model to 3-D is straightforward [40]. The underlying fractional flow meanwhile is formulated in 1-D.

Pressure-driven growth (in 2-D) has been used to describe a number of foam IOR scenarios in reservoirs including effects of reservoir heterogeneity [48] and anisotropy [49,50], the influence of surfactant migrating downward through a reservoir [51], and also the effect of an increase in injection pressure used to drive the foam along [52]. There is however a scenario that pressure-driven growth has not yet tackled successfully, namely a *decrease* in net driving pressure moving the foam along, net driving pressure here being the difference between an injection pressure and a pressure downstream of the displacing foam.

Although in oil recovery terms it is best to keep injection pressure as high as possible [52], a decrease could conceivably still occur for a number of scenarios e.g. a reduction in performance of a pump delivering injection fluids to foam IOR or else a deliberate reduction in injection pressure to prevent fracturing rock. A well might also need to be shut in (i.e. injection ceased): the seal placed on a such a well would need to withstand a pressure high enough to prevent the shut-in well from collapsing, but even so, not quite so high as the pressure that would have been needed to continue injection outwards from it. It is also conceivable (albeit again not necessarily desirable in oil recovery terms) that net driving pressure for foam could decrease, not due to a decrease in injection pressure upstream, but rather due to a rise in pressure downstream, close to a production well say. This could happen e.g. if an additional injection well were to be brought online in a neighbouring part of the reservoir, driving fluids towards that same production well, and leading to changes in an overall pressure field.

In scenarios like these, over much the flow domain, foam continues to displace reservoir fluids from the original injection well towards the original production well, albeit less rapidly than before. However there is an effect of hydrostatic pressure which must be taken into account: foam is less dense than fluids present in the reservoir downstream (e.g. oil, water, previously injected slugs of surfactant solution) and this density difference produces a hydrostatic pressure field [40]. As a result, there is a certain "neutral" depth at which the hydrostatic pressure (downstream) balances injection pressure (upstream) leading to zero net driving pressure: foam cannot penetrate any deeper than this [41]. If injection pressure falls and/or downstream pressure rises, this maximum penetration depth (or "neutral" depth) shifts upwards. Foam that penetrated down to the original neutral depth now has an unbalanced hydrostatic pressure pushing it back upwards: i.e. foam at depth must undergo a flow reversal, even though foam higher up continues propagating in the original flow direction.

In scenarios of injection continuing at a reduced net driving pressure, the reverse flow at depth on the foam front will generally be less than the forward flow higher up, although for a shut-in well mentioned earlier (i.e. no net injection), the reverse flow at depth and forward flow higher up must balance. Either way, flow reversal is the phenomenon we model here. Outright reversal can be viewed as an extreme case of a more general change in direction of flow due to a change in the driving pressure field. We need to understand such flow direction changes, and flow reversal in particular, in order to know how the totality of fluids distribute in this system, even though admittedly in oil recovery applications, the flow-reversed part of the front at depth should contain rather less oil than the forward flowing part that we continue to recover higher up. This follows because (as mentioned earlier) it is advantageous to inject at as high a pressure as possible [52], meaning that, by design, foam already penetrates rather deeper than the majority of oil is likely to be present. Hence shifting the "neutral depth" upwards a little does not change this situation.

In the context of pressure-driven growth, flow reversal is known to be numerically challenging to model. The reason is that pressure-driven growth is well-behaved numerically when a foam front that is displacing through the reservoir is convex (seen from the direction towards which it is advancing, see e.g. the front sketched in Figure 1(a)) but is ill-behaved numerically for parts of the front that are concave [41]: concavities can focus down into sharp corners at which the front reorients significantly over a small distance. If however the flow direction of at least part of the foam front reverses as we envisage here, an originally convex section of front switches to being concave (viewed from the new direction towards which it is now advancing, see Figure 2(a)).

Fortunately strategies exist for regularising the numerical behaviour of concave fronts within pressure-driven growth [41], and these can be invoked here. There is however an even more fundamental issue that we face. As has been mentioned, the pressure-driven growth model was formulated [40] based on an underlying fractional-flow theory, which informs the pressure-driven growth model, i.e. feeds parameters to it. However the formulation as it currently stands [40,41] assumes forward-directed fractional flows. A complete reformulation of pressure-driven growth turns out to be required for a situation with an initial forward flow followed by a flow reversal: carrying out this reformulation is the main novel contribution that the present work achieves. This is done, as one might expect, by returning to fractional-flow theory, obtaining novel solutions for the equations governing that theory under flow reversal, and then obtaining parameters to feed back into pressure-driven growth. A key result from doing this will be that a flow-reversed foam front is much less mobile than the original forward flowing front was.

The rest of this work is laid out as follows. Section 2 sets the geometrical context of the study and outlines the main findings to be presented. Section 3 provides parameter values to use in foam IOR models, including a base case parameter set. Section 4 presents governing equations and works through an example, presenting results to illustrate the system behaviour: the results build towards the reformulation of pressure-driven growth incorporating flow reversal conditions. Section 5 then concludes the work. The supplementary material explores the extent to which model results are sensitive to chosen parameter values, varying with respect to the base case.

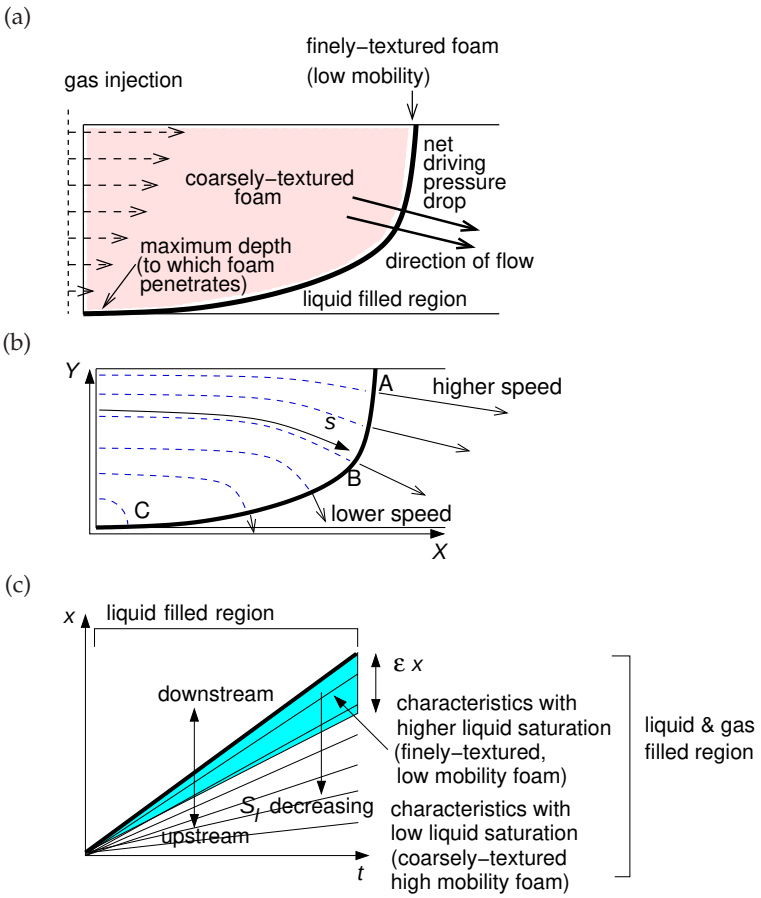

Figure 1. (a) Schematic sketch of 2-D pressure-driven growth. Gas injection causes a foam front to propagate, with finely-textured, low mobility foam at the front separating liquid (downstream) from coarsely-textured foam (upstream). The direction of propagation is normal to the front, and the speed of propagation depends on a net pressure difference (the difference between an upstream injection pressure and a downstream hydrostatic pressure). There is a "neutral" depth at which these two pressures balance, hence giving the maximum depth to which foam can penetrate. (b) Coordinate system (X, Y) for pressure-driven growth showing the current front shape for some arbitrary time τ. Different points on the front have followed different trajectories (dashed curves) to reach their current location (the variable s measures the path length on each trajectory, and the thickness of the front is assumed to be εs for some given $\varepsilon \ll 1$). The height of a point above the neutral depth determines its current speed (indicated by arrows), so that e.g. point A is moving faster than B, whereas point C (which has nearly reached the neutral depth) is barely moving. (c) Sketch of 1-D fractional flow x-t diagram (the variable x here is the 1-D analogue of the path length variable s in 2-D pressure-driven growth, and t is time). A foam front (bold line) separates liquid downstream from liquid and gas (i.e. foam) upstream. In the upstream liquid and gas filled region, a fan of characteristics appears (each characteristic line of fixed liquid saturation S_l and with specified slope). The lowest mobilities in the fan correspond to S_l values close to the front (shaded region), the width of this region at any time t being a fraction ε of the distance x through which the front has propagated.

2. Context and findings of the present study

The 2-D pressure-driven growth model [40,41] involves tracking elements on a foam front executing curved trajectories, with different elements (e.g. points A, B and C in Figure 1(b)) displacing through different path lengths s. Pressure-driven growth only attempts to track finely-textured foam formed in situ located at the front itself [40]. This has a specific liquid saturation,

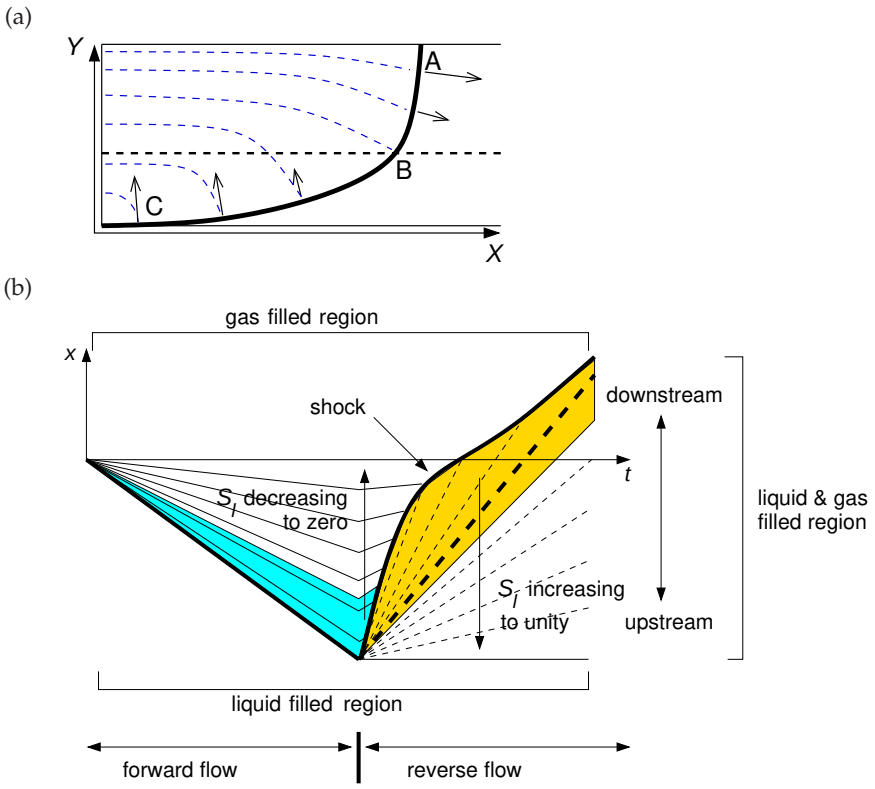

Figure 2. (a) Schematic sketch of pressure-driven growth admitting flow reversal. Initially pressure-driven growth proceeds in a forward direction, with points on the front following the paths indicated by the dashed curves. At a certain time, the injection pressure driving the flow is reduced, meaning that the "neutral" depth at which injection pressure balances hydrostatic pressure (indicated by a bold dashed line) shifts higher up than before. Points that are even higher up than this (e.g. the point labelled A) continue moving in much the same direction as before, albeit with a reduced net driving pressure and hence a reduced velocity. Points at the neutral depth (point B) cease moving altogether. Points even lower down (point C) move in the reverse direction from before: these are the points of interest here. (b) x-t diagram illustrating the predictions of fractional-flow theory under a forward flow followed by reverse flow: the sign convention adopted here is that forward flow corresponds to the negative x direction and reverse flow corresponds to the positive x direction. A characteristic fan appears during the forward flow phase, and this fan is reflected at the instant of flow reversal. However at the instant of flow reversal, a second characteristic fan appears. This corresponds to a different set of liquid saturations S_l (typically higher S_l values than the original fan). The two fans meet across a shock. On both fans there are certain subsets of S_l values that have low mobility (shown as shaded regions here). The bulk of the pressure drop occurs across these low mobility regions.

with saturation governing texture [43]: a minimum liquid saturation is required for foam to resist capillary collapse and thereby preserve a fine texture. Based on its fine texture, foam at the front is also expected to have low mobility, as it is the foam films that reduce mobility [19]. However moving back or forward from the foam front along the 2-D curved paths indicated in Figure 1(b), we encounter a different set of liquid saturations, and hence a different set of textures and mobilities. The mobility, or more specifically a quantity to be defined later called total relative mobility $\mathcal{M}_{\rm tot}$, is a function of liquid saturation S_l here, this function then capturing in an implicit fashion [24,26,53] the link between mobility and foam texture as well as that between texture and liquid saturation. The distribution of liquid saturations (and hence distribution of relative mobilities) moving back or forward along the 2-D curved paths, is assumed to be the same as

what would result from 1-D fractional-flow theory [43–46] using a "straightened out" 1-D path displaced through the same path length. This is illustrated in Figure 1(c), using now x to denote the 1-D spatial coordinate (as opposed to the 2-D path length s). Fractional-flow theory yields a so called fan of characteristic lines, giving the spatial distribution of S_l (and hence the spatial distribution of $\mathcal{M}_{\rm tot}$) for any specified front displacement x (or equivalently, for any specified time t, since we can use the 1-D fluid flux to relate x and t). Given the 1-D front location x, the 1-D fractional-flow theory can be used to identify a region adjacent to the front at which liquid saturations give low mobilities (low $\mathcal{M}_{\rm tot}$), the extent of this region being denoted εx in Figure 1(c). This information is then fed into 2-D pressure-driven growth.

The above discussion however, whether for 2-D pressure-driven growth or 1-D fractional flow, only concerns forward flows. What happens in 2-D under a possible reverse flow is illustrated in Figure 2(a). Points A, B and C in Figure 2(a) (analogous to points already shown in Figure 1(b)) behave differently after a reduction of injection pressure say. As mentioned earlier, the "neutral" depth at which the front does not displace moves higher up than before (to the bold dashed line in Figure 2(a)), so is above where the bottom of the front was originally. Point A remains above the new neutral depth so continues moving in the same direction as originally, albeit with a lesser speed due to the net driving pressure being reduced. Point B however finds itself exactly at the new neutral depth, so ceases to move altogether. Point C however is now below the neutral depth, so undergoes reverse flow: 1-D fractional flow incorporating reverse flow must then be used to find the mobility associated with a point such as C. This is what the present work achieves. Note that (unlike in 1-D) there is no requirement in a 2-D model, for a point such as C to retrace exactly the same (X, Y) positions during reverse flow that it passed through during forward flow. Indeed the 2-D model that we will develop does not require paths to be retraced: the 1-D fractional flow information that feeds into mobility of the 2-D model be will formulated in terms of distances travelled in forward and reverse flow, rather than full details of the 2-D layout of a trajectory.

Although we will present our detailed model and results in due course, it is useful to state in advance the main findings to be obtained. These are summarised schematically in Figure 2(b).

Supposing that the forward flow mode is now considered to proceed in the negative x direction (a contrast from Figure 1(c)), the reverse flow mode in Figure 2(b) proceeds in the positive x direction. The characteristic pattern during the forward flow phase is the same as in Figure 1(c), apart from the sign change for x. Upon flow reversal, we will find that the characteristic fan is reflected and starts to close up on itself in the x-t plane as Figure 2(b) shows. The size of the low mobility region (the shaded region on the reflected fan) should then be proportional to the difference between the distance propagated during the forward and reverse flow phases.

This is however not the full story. A second characteristic fan in Figure 2(b) appears at the instant of flow reversal, corresponding to different set of liquid saturations, typically higher saturations than those in the original fan. This new fan also has (see shaded region) a set of saturations with low mobility (albeit different mobility from that in the original fan). Moreover the spatial extent of this low mobility region starts out small and grows over time, whereas the extent of the low mobility region in the reflection of the original fan is now shrinking over time.

Which of the two low mobility regions ultimately accounts for the bulk of the pressure drop for a given imposed fluid flux (and thereby which of them ultimately determines the flux for a given imposed driving pressure difference) depends on how their mobilities and spatial extents compare. It turns out moreover that, taken separately, the two fans would occupy overlapping regions in the x-t plane. The system resolves this overlap as Figure 2(b) shows, by introducing a shock, with the reflected original fan being downstream of the shock and the new fan being upstream of it. Since the flow has reversed, the sense of what is meant by "downstream" and "upstream" has of course switched, i.e. gas is downstream now and liquid is upstream.

All of these features will be revealed by the 1-D fractional flow analysis to follow. Ultimately the 1-D fractional-flow theory will enable us to set up a 2-D pressure-driven growth model accounting for forward and reverse flow. Here however our aim is merely to set up the 2-D model in a well-posed fashion consistent with 1-D fractional flow. Solution of the 2-D model

μ_l/μ_g	$S_{l,*}$	$S_{l,\epsilon}$	R_f
10	0.37	0.02	185

Table 1. Set of parameter values to be used in base case calculations.

itself (incorporating reverse flow effects) is left for future work. Our purpose in the sections that follow is to show an actual calculation illustrating the principles for forward and reverse flow outlined above and as sketched in Figure 2(b). Before we can do that however we need to specify the parameter set with which we work: this is done in the next section.

3. Parameter set for fractional flow

This section defines the parameters needed to set up 1-D fractional-flow theory, and is laid out as follows. Section (a) specifies so called relative permeabilities, whilst section (b) specifies liquid and gas viscosities and also relative mobilities of liquid and gas. Both of the above sections assume the absence of foam, the effect of foam being considered in section (c). Fractional flow itself and total relative mobility are introduced in section (d).

(a) Relative permeabilities

The main parameters we require are relative permeabilities of liquid ($k_{r,l}$) and of gas (in the first instance in an unfoamed system, and denoted $k^0_{r,g}$). Both of these are functions of liquid saturation S_l, and, describe the flow of each phase through a given porous medium under multiphase flow conditions, relative to what would occur for single phase flow.

Typically [54] there is some irreducible liquid saturation at which no liquid can no longer flow, thereby setting a minimum level for S_l. Likewise there is an irreducible gas saturation and this sets a maximum level for S_l. Here, in the interests of simplicity, we assume these irreducible saturations are negligible, so that S_l can in principle cover the full domain $0 \leq S_l \leq 1$. This assumption is not too restrictive: even when irreducible saturations are non-negligible, it is possible to replace S_l by an "effective" liquid saturation [54] that does cover the domain 0 to 1. The theory with negligible irreducible saturations is thereby recovered.

Following [54,55] we assume power law relations for $k_{r,l}$ and $k^0_{r,g}$. For simplicity, we will assume throughout most of this work quadratic relations which illustrate behaviour

$$k_{r,l} = S_l^2, \quad k^0_{r,g} = (1 - S_l)^2. \tag{3.1}$$

It is possible to consider different powers, as has done by [35] based on data of [56]. The effect of considering different powers will be considered in the supplementary material.

(b) Viscosities and relative mobilities

We also require viscosities of liquid μ_l and gas μ_g phases, or more specifically (when we express the system in dimensionless form) the ratio between these viscosities. Relative mobilities of the liquid and (unfoamed) gas phases are respectively $\lambda_{r,l} \equiv k_{r,l}/\mu_l$ and $\lambda^0_{r,g} \equiv k^0_{r,g}/\mu_g$. Data provided by [40] for a SAG process suggests (unfoamed) gas is between one and two orders of magnitude less viscous than aqueous liquid (surfactant solution in the case of SAG). In this context it is worth remembering that oil reservoirs tend to be at elevated temperatures and pressures compared to surface conditions, and that can impact on the liquid-to-gas viscosity ratio. In what follows we assume that the ratio μ_l/μ_g is equal to 10 throughout (see Table 1).

(c) Effect of foam upon gas flow

So far we have considered a system without foam. In the presence of foam, liquid relative permeability $k_{r,l}$ and liquid relative mobility $\lambda_{r,l}$ are considered to be unchanged whereas gas relative permeability $k_{r,g}$ is reduced [40], possibly quite substantially. Viscosities μ_l and μ_g are assumed unchanged. Supposing that foam reduces gas relative permeability alone is a convenient assumption, albeit a simplification, given that in general foam could produce an increase in gas apparent viscosity in addition to a decrease in relative permeability. However the effect of foam increasing apparent viscosity is similar to the effect of foam decreasing relative permeability: in both cases relative mobility of gas $\lambda_{r,g} \equiv k_{r,g}/\mu_g$ decreases, typically quite substantially.

Data for effects of foam upon $k_{r,g}$ are available from [56] and a number of studies [23,26,35,43, 44,57] have fit parameters to such data. Studies typically define three parameters: R_f a maximum mobility reduction factor (a value in excess of unity); $S_{l,*}$ a liquid saturation at which a so called limiting capillary pressure is reached; and $S_{l,\epsilon}$ a range of liquid fractions about $S_{l,*}$ over which foam collapse occurs. Here we represent the foamed $k_{r,g}$ in terms of these parameters as

$$k_{r,g} = k^0_{r,g}\left(1 + (R_f - 1)\frac{(1 + \tanh((S_l - S_{l,*})/S_{l,\epsilon}))}{2}\right)^{-1}. \tag{3.2}$$

We choose (see Table 1) $S_{l,*} = 0.37$ in line with [43] and also $S_{l,\epsilon} = 0.02$ corresponding to a 2% progressive collapse [40] either side of $S_{l,*}$. It is clear from equation (3.2) that $k_{r,g}$ falls from $k^0_{r,g}$ for S_l less than about $S_{l,*} - O(S_{l,\epsilon})$ (the foam undergoes capillary collapse as it dries out in this regime [23,25] so becomes coarsely-textured and comparatively mobile) to a smaller value $k^0_{r,g}/R_f$ for S_l greater than about $S_{l,*} + O(S_{l,\epsilon})$ (so called strong foam [43,58] with fine texture and low gas mobility).

Other functional forms are possible [24] in lieu of equation (3.2). For instance [23,26,57] have used an $\arctan$ form rather than a $\tanh$ form, but the effect is the same: $k_{r,g}$ falls smoothly from $k^0_{r,g}$ to $k^0_{r,g}/R_f$ as S_l increases through $S_{l,*}$. Meanwhile [35,43,44] have assumed a straight line relation between $k^0_{r,g}/k_{r,g}$ and S_l over the domain $S_{l,*} - S_{l,\epsilon} \le S_l \le S_{l,*} + S_{l,\epsilon}$ with constant $k^0_{r,g}/k_{r,g}$ either side of this domain. This is slightly less convenient because the function $k_{r,g}$ is not smooth at $S_l = S_{l,*} \pm S_{l,\epsilon}$. This is the reason we choose a smooth function like equation (3.2).

Typically R_f values are very large, up to the order of tens of thousands [23,26,44,57] meaning that gas in foam is much less mobile than unfoamed gas. For example [43] used $R_f = 18500$. We will present some results with that R_f value later on towards the end of this work (see also supplementary material). For the most part however we will illustrate calculations with a smaller value $R_f = 185$ (see Table 1). Although not on the order of tens of thousands, this is still much larger than unity, so foam is still having a very significant effect on reducing the mobility of gas.

(d) Definition of fractional flow and total relative mobility

If a pressure gradient ∇p is applied, the superficial liquid flow down that pressure gradient is $-k\lambda_{r,l}\nabla p \equiv -(kk_{r,l}/\mu_l)\nabla p$ whilst superficial gas flow is $-k\lambda_{r,g}\nabla p \equiv -(kk_{r,g}/\mu_g)\nabla p$. The fraction of flow that is liquid f_l is therefore

$$f_l = \frac{\lambda_{r,l}}{\lambda_{r,l} + \lambda_{r,g}} = \frac{k_{r,l}/\mu_l}{k_{r,l}/\mu_l + k_{r,g}/\mu_g} \tag{3.3}$$

with $1 - f_l$ being the fraction of flow that is gas. Equation (3.3) can also be written as $f_l = k_{r,l}/(\mu_l \mathcal{M}_{\rm tot}) = k_{r,l}/M_{\rm tot}$ where $\mathcal{M}_{\rm tot}$ denotes the total relative mobility

$$\mathcal{M}_{\rm tot} = \lambda_{r,l} + \lambda_{r,g} = k_{r,l}/\mu_l + k_{r,g}/\mu_g, \tag{3.4}$$

with dimensionless analogue $M_{\rm tot} \equiv \mu_l \mathcal{M}_{\rm tot} = k_{r,l} + (\mu_l/\mu_g)k_{r,g}$.

Plots of f_l and $M_{\rm tot}$ vs S_l are given in Figure 3, for cases both without and with foam. In Figure 3(a), f_l without foam increases gradually from 0 to 1 as S_l increases. With foam the increase in f_l is more abrupt, and happens around $S_l = S_{l,*}$. Meanwhile $M_{\rm tot}$ without foam (see

Figure 3(b)) tends to decrease with increasing S_l although there is a small increase close to $S_l = 1$. By construction $M_{\rm tot}$ takes the value μ_l/μ_g (equal to 10 for our data) at $S_l = 0$ and equals unity at $S_l = 1$. With foam, $M_{\rm tot}$ falls abruptly in the neighbourhood of $S_{l,*}$, attaining (see Figure 3(c)) $M_{\rm tot}$ values much smaller than are achieved at either $S_l = 0$ or $S_l = 1$. As section 2 states, the basis of the pressure-driven growth model is that finely-textured, strong foam with sufficient liquid saturation to avoid capillary collapse has much lower mobility than either low liquid saturation foam (which has already collapsed to a coarsely-textured state) or pure liquid. One issue we will return to later however is that it is not clear whether the system necessarily selects the set of liquid saturations needed for this low mobility condition to be realised, at least not as long as forward flow conditions (i.e. gas pushing into liquid) persist.

4. Governing equations and illustrative example

Having specified a parameter set, we now formulate and solve models, which we do as follows. Sections (a)–(b) present respectively the standard 2-D pressure-driven growth and 1-D fractional-flow theory in forward flow mode. Sections (c)–(d) then consider 1-D fractional-flow theory after reverse flow is imposed. Sections (e)–(f) relate 1-D fractional flow fluxes to driving pressures in the case of forward and reverse flows. Finally section (g) uses results from all the foregoing sections to derive equations describing 2-D pressure-driven growth under flow reversal.

(a) Pressure-driven growth: Forward flow case

In the first instance we consider pressure-driven growth in forward flow mode. A net driving pressure difference ΔP is imposed across a low mobility foam front of thickness εs, with s denoting the distance the front has displaced and ε being the ratio between front thickness and front displacement ($\varepsilon \ll 1$ here). The implication (already suggested in section 2 in the context of discussing Figure 1) is that any pressure drop occurs across a thin region of extent much smaller than the distance the front has displaced, albeit with the size of the region εs assumed proportional to the displacement distance s: in [41], a value $\varepsilon = 0.01$ was assumed for instance. We use P to denote pressure here (instead of p used earlier) to make a distinction between pressure-driven growth and fractional-flow theory. The pressure gradient at the front is $\nabla P = -(\Delta P/(\varepsilon s))\boldsymbol{n}$ where $\boldsymbol{n}$ is the front normal for an element of front.

Darcy's law then implies that the superficial gas flux at the front is $(k\lambda_{r,g}\Delta P/(\varepsilon s))\boldsymbol{n}$ where k is the permeability of the medium and $\lambda_{r,g} \equiv k_{r,g}/\mu_g$ is the relative mobility of (foamed) gas. The value of $\lambda_{r,g}$ depends on liquid saturation at the front S_l. We denote this saturation $S_{l,\rm fwd}$ to remind us that it is the saturation at the front in forward flow.

The foam front position $\boldsymbol{X}$ versus time τ is now assumed to propagate at the interstitial velocity of the gas, and hence for a medium of porosity ϕ becomes [41]

$$\frac{{\rm d}\boldsymbol{X}}{{\rm d}\tau} = \frac{k\lambda_{r,g}\Delta P}{(1 - S_{l,\rm fwd})\phi\varepsilon s}\boldsymbol{n}. \tag{4.1}$$

Again the choice of notation $\boldsymbol{X}$ and τ (instead of x and t used earlier) is deliberate to highlight the difference between pressure-driven growth and fractional flow.

Using the definitions from section 3(d) it is possible to express fractional flow of liquid f_l as $\lambda_{r,l}/\mathcal{M}_{\rm tot}$ and fractional flow of gas $1 - f_l$ as $\lambda_{r,g}/\mathcal{M}_{\rm tot}$. It then follows that

$$\frac{{\rm d}\boldsymbol{X}}{{\rm d}\tau} = \frac{k\mathcal{M}_{\rm tot,fwd}\Delta P}{\phi\varepsilon s}\frac{(1 - f_{l,\rm fwd})}{(1 - S_{l,\rm fwd})}\boldsymbol{n} \equiv \frac{q}{\phi}\frac{(1 - f_{l,\rm fwd})}{(1 - S_{l,\rm fwd})}\boldsymbol{n} \tag{4.2}$$

where $q \equiv k\mathcal{M}_{\rm tot,fwd}\Delta P/(\varepsilon s)$ is (by Darcy's law) the magnitude of the total fluid flux (liquid and gas taken together), and where $\boldsymbol{q} \equiv q\,\boldsymbol{n}$ is the vector flux. Moreover $\mathcal{M}_{\rm tot,fwd}$ and $f_{l,\rm fwd}$ are specifically total mobilities and fractional flow at the saturation $S_l = S_{l,\rm fwd}$.

Note that ΔP and hence q here depend on where we are on the front. To compute ΔP, the injection pressure driving the front denoted $P_{\rm inj}$ is opposed by a hydrostatic pressure, which

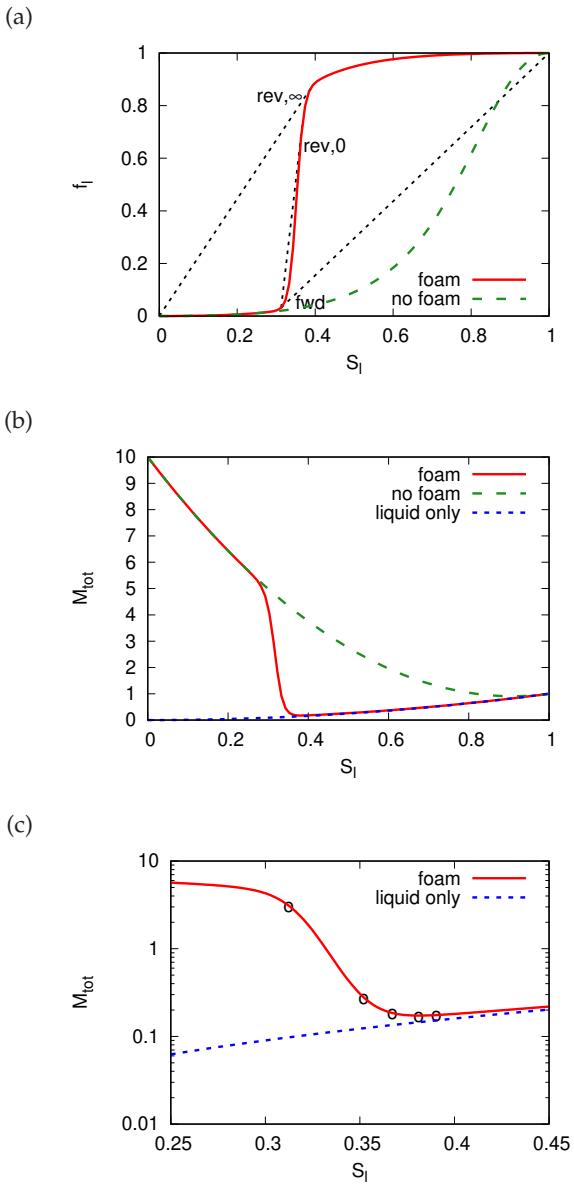

Figure 3. (a) Fractional flow curve f_l vs liquid saturation S_l, comparing the case with foam and the no foam case. In the case with foam, three lines are constructed on the fractional flow curve which are (from right to left), a line joining $(S_{l,\mathrm{fwd}}, f_l(S_{l,\mathrm{fwd}}))$ to (1,1); a line joining $(S_{l,\mathrm{fwd}}, f_l(S_{l,\mathrm{fwd}}))$ to $(S_{l,\mathrm{rev},0}, f_l(S_{l,\mathrm{rev},0}))$; and a line joining (0,0) to $(S_{l,\mathrm{rev},\infty}, f_l(S_{l,\mathrm{rev},\infty}))$. (b) Total mobility curve M_{tot} vs liquid saturation S_l comparing the case with foam and the no foam case. Also shown is the mobility of liquid $\lambda_{r,l}$ suitably non-dimensionalised ($\mu_l \lambda_{r,l} \equiv f_l M_{\mathrm{tot}}$ i.e. the contribution to M_{tot} coming from the liquid). (c) Zoomed view of total mobility curve on log scale. The circled points correspond (from left to right) to mobilities at S_l values $S_{l,\mathrm{fwd}}$, $S_{l,\mathrm{infl}}$, $S_{l,\mathrm{rev},0}$, $S_{l,\mathrm{min\ mob}}$, $S_{l,\mathrm{rev},\infty}$.

grows with depth with a gradient $\Delta\rho\, g$ where $\Delta\rho$ is the density difference between liquid and gas, and g is gravity acceleration. We now make both $\boldsymbol{X}$ and s dimensionless on a scale $P_{\rm inj}/(\Delta\rho\, g)$ (physically a maximum penetration depth or "neutral" depth for forward flow), whilst ΔP is made dimensionless on the scale $P_{\rm inj}$. Meanwhile time τ is made dimensionless on a scale

$$\tau_{\rm scale} = \frac{\phi\varepsilon P_{\rm inj}}{k\mathcal{M}_{\rm tot,fwd}\Delta\rho^2 g^2}\frac{(1-S_{l,\rm fwd})}{(1-f_{l,\rm fwd})}. \tag{4.3}$$

For compactness of notation we use the same symbols $\boldsymbol{X}\equiv(X,Y)$, s, ΔP and τ to denote both dimensional and dimensionless variables: note that from here on, we work primarily with equations in terms of dimensionless variables, although we revisit dimensional variables briefly in sections (e) and (g) below. The (dimensionless) model becomes

$$\frac{\mathrm{d}\boldsymbol{X}}{\mathrm{d}\tau} = \frac{\Delta P}{s}\boldsymbol{n}. \tag{4.4}$$

If the origin of the vertical coordinate $Y=0$ is placed at the maximum penetration depth of the foam front, then the solution domain extends from $Y=0$ to $Y=1$, and in dimensionless variables $\Delta P = Y$. Meanwhile s is updated according to $\mathrm{d}s/\mathrm{d}\tau = (\mathrm{d}\boldsymbol{X}/\mathrm{d}\tau).\boldsymbol{n}$. This now constitutes the (dimensionless) 2-D pressure-driven growth model for forward flow. In order to consider how the model might need to be modified in the presence of forward and reverse flow, we need first to examine analogous 1-D fractional flow models.

(b) Fractional-flow theory: Forward flow

Fractional-flow theory in 1-D is described by the Buckley-Leverett equation [59]

$$\partial(S_l\phi)/\partial t + \partial(qf_l)/\partial x = 0 \tag{4.5}$$

where S_l is liquid saturation, ϕ is porosity (assumed constant and uniform here), t is time, q is total flux of fluids (liquid and gas together; q is necessarily spatially uniform for incompressible fluids in 1-D), f_l is the fractional flow of liquid, and x is 1-D spatial coordinate. Physically equation (4.5) is nothing more than a conservation equation for liquid in the pores, and we consider it, in the first instance, in a forward flow mode with gas pushed into liquid. This can be solved by the method of characteristics [60]. As already alluded to, there will be a fan of characteristics in the x-t plane: S_l is constant along each characteristic. The slope of each characteristic line will be $(q/\phi)\mathrm{d}f_l/\mathrm{d}S_l$. Finding the solution therefore requires knowledge of the functional form of f_l vs S_l.

For the specific functional forms given in (3.1)–(3.3), Figure 3(a) plots f_l vs S_l in cases both with foam and without. In both cases, we see that f_l is small when S_l is small and f_l is close to unity when S_l is large. The main feature of interest in Figure 3(a) is that in the case of foam there is a sharp rise in f_l close to a certain S_l value, corresponding to the saturation $S_{l,*}$ above which foam films survive, but below which capillary suction causes foam films to collapse.

In 1-D fractional flow in forward flow mode, if gas is pushed into initially pure liquid (i.e. $S_l = f_l = 1$ initially) there must, at some location, be a boundary between a pure liquid region (downstream) and a region partly filled with gas (upstream). The Rankine-Hugoniot condition [60] tells us that this boundary propagates with a velocity $(q/\phi)\Delta f_l/\Delta S_l$ where Δf_l and ΔS_l are jumps in f_l and S_l at the boundary. The value of S_l immediately adjacent to this boundary must however be determined by matching with the speed of the corresponding characteristic which is $(q/\phi)f_l'(S_l)$. This then defines an equation for a so called contact discontinuity [60]

$$f_l'(S_{l,\rm fwd}) = (1-f_l(S_{l,\rm fwd}))/(1-S_{l,\rm fwd}). \tag{4.6}$$

The value $S_l = S_{l,\rm fwd}$ corresponding to this forward flow contact discontinuity is indicated on Figure 3(a). Comparing with equation (4.2) indicates that 2-D pressure-driven growth, at least in forward flow mode, is doing nothing more than capturing this contact discontinuity.

Returning to the 1-D fractional flow case, in the problem of interest we set up our coordinate system such that during forward flow $q<0$, so characteristics actually have negative slope. This

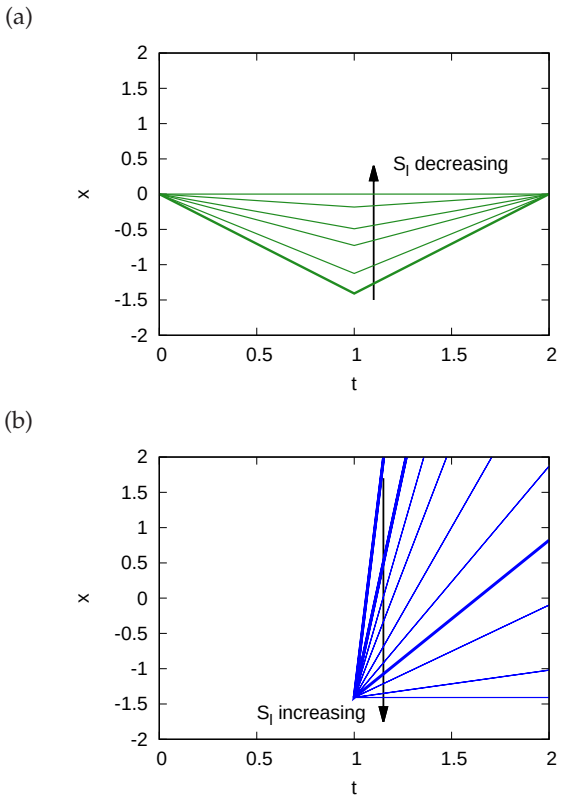

Figure 4. Characteristic fans during forward and reverse flow which occupy overlapping regions of the x-t plane. (a) Characteristic fan that appears during the forward flow phase corresponding to a set of low liquid saturations $0 \leq S_l \leq S_{l,\mathrm{fwd}} \equiv 0.3124$. The S_l values plotted (from bottom to top) are $S_l = S_{l,\mathrm{fwd}} \equiv 0.3124$, 0.31, 0.305, 0.3, 0.28 and 0, these values have been chosen to give a reasonable spacing between adjacent characteristics making the plot easier to view. All these characteristics are reflected after flow reversal at $t = 1$. (b) New characteristic fan that appears after flow reversal, originating from location $(x, t) = (x_{s,\mathrm{switch}}, t) = (-1.4083, 1)$ and corresponding to higher liquid saturations. The S_l values plotted are (top to bottom) $S_{l,\mathrm{infl}} \equiv 0.3520$ (shown as a thicker line), $S_{l,\mathrm{rev},0} \equiv 0.3672$ (again a thicker line), 0.3713 (the significance of this value is explained in Figure 6), 0.375, 0.38, 0.385, $S_{l,\mathrm{rev},\infty} \equiv 0.3904$ (thicker line), 0.4, 0.5 and 1. Again S_l values are chosen arbitrarily to give reasonable spacing between adjacent characteristics.

is as shown in Figure 2(b) (a sketch) and Figure 4(a) (an actual computation using data from equations (3.1)–(3.3)). The only S_l values admitted in the characteristic fan are those that have slopes of magnitude less than or equal to the slope of $S_{l,\mathrm{fwd}}$, i.e. only S_l values less than or equal to $S_{l,\mathrm{fwd}}$ are admitted. This is what Figure 2(b) and Figure 4(a) show. Note also (see Figure 3(c)) that the mobility M_{tot} at $S_{l,\mathrm{fwd}}$ is substantially lower than the mobility of pure gas at $S_l = 0$, albeit (for the present parameter values at least) still higher than M_{tot} of pure liquid at $S_l = 1$.

(c) Fractional-flow theory: Reverse flow

So far all we have done is review theories for conventional forward flow. Now we suppose that at a certain time t_r flow is reversed, so that q switches from negative to positive. We assume that the fractional flow curve (Figure 3(a)) curve is unchanged in forward and reverse flow. Even this is by no means certain however, since liquid invading a body of gas might cause a significant part of the gas to become trapped [61,62]. What we will discover however is that even assuming the same fractional flow curve, forward and reverse flow do not lead to the same mobility, since the

system can select different saturations (and hence different mobilities) according to whether flow is forward or reversed.

Assuming that the fractional flow curve remains unchanged as we have stated, it is clear that the slope of any given characteristic line is also reversed and this is what Figure 4(a) indicates: the characteristic fan that was produced originally is reflected and starts to close up on itself. For simplicity, we suppose that q has the same magnitude before and after the flow reversal, meaning the fan closes at the same rate as it originally opened. This simplifying assumption will not impact our ability to relate flow-reversed 1-D fractional flows to 2-D pressure-driven growth, since the information communicated between the different models concerns distances that fronts propagate, rather than propagation rates. Nevertheless finding the flow-reversed reflection of the original characteristic fan is not the full solution of the problem, as we will argue in what follows.

Before proceeding, it is convenient to make x dimensionless on the scale $t_r|q|/\phi$ and t dimensionless on the scale t_r. Note that these scales which are relevant for 1-D fractional flow differ from those which arise naturally 2-D pressure-driven growth in section (a), and we deliberately used distinct notation $\boldsymbol{X}$ and τ in 2-D to highlight the difference. The dimensionless equation for 1-D fractional flow (for compactness of notation, using the same symbols x and t as before) now becomes

$$\partial S_l/\partial t + \partial f_l/\partial x = 0 \tag{4.7}$$

with the flow reversal happening at dimensionless time $t = 1$. At this time, the boundary between pure liquid (which after flow reversal, is now considered upstream) and liquid and gas (downstream) is found at a dimensionless location $x = -f_l'(S_{l,\mathrm{fwd}})$.

In addition to the characteristic fan already mentioned above, a second characteristic fan appears now originating at $(x,t) = (-f_l'(S_{l,\mathrm{fwd}}), 1)$. This is sketched in Figure 2(b) and computed in Figure 4(b). The new fan has rather larger S_l values than before. Noting that f_l vs S_l exhibits an inflection point at some value $S_l = S_{l,\mathrm{infl}}$, the original fan corresponds to S_l values strictly less than $S_{l,\mathrm{infl}}$, whilst the new fan corresponds to S_l values greater than $S_{l,\mathrm{infl}}$. Note that, as Figure 2(b) and Figure 4 indicate, whereas S_l decreases moving upward through the original fan (the slope $f_l'(S_l)$ decreases in this direction), S_l actually increases moving downward through the new fan (again $f_l'(S_l)$ decreases in this direction).

It is clear from the regions plotted in Figure 4(a)–(b) that the two fans overlap. Any (x,t) location in the overlap region has in principle two distinct S_l values, one corresponding to each fan. However it is only usually possible to have two distinct S_l values at a single location if a shock is present. Thus as sketched in Figure 2(b) a shock divides the (x,t) plane into regions allocated to each fan, and only at the shock itself is S_l double valued.

If a shock is at a given location $x = x_s(t)$, then the two S_l values associated with it (denoted $S_{l,\mathrm{low}}$ and $S_{l,\mathrm{high}}$, indicating values respectively less than $S_{l,\mathrm{infl}}$ and greater than $S_{l,\mathrm{infl}}$) satisfy

$$f_l'(S_{l,\mathrm{low}}) = -x_s(t)/(2-t) \tag{4.8}$$

$$f_l'(S_{l,\mathrm{high}}) = (x_s(t) - x_{s,\mathrm{switch}})/(t-1) \tag{4.9}$$

where $x_{s,\mathrm{switch}}$ (i.e. the value of x_s at the instant of switching to flow reversal) satisfies $x_{s,\mathrm{switch}} \equiv -f_l'(S_{l,\mathrm{fwd}})$, i.e. it corresponds to the location that the original fan in the forward flow mode reached at dimensionless time $t = 1$. For our data $S_{l,\mathrm{fwd}} \approx 0.3124$ and $x_{s,\mathrm{switch}} \approx -1.4083$. Given t and $x_s(t)$, equations (4.8)–(4.9) are nonlinear equations to solve for $S_{l,\mathrm{low}}$ and $S_{l,\mathrm{high}}$. Equation (4.8) recognises that all characteristics on the reflection of the original forward flow fan focus in on $(x,t) = (0,2)$ (see Figure 4(a)), whereas equation (4.9) recognises that all characteristics on the new fan produced after $t = 1$ originate from $(x,t) = (x_{s,\mathrm{switch}}, 1)$ (see Figure 4(b)).

Once we know x_s, $S_{l,\mathrm{low}}$ and $S_{l,\mathrm{high}}$ and hence $f_{l,\mathrm{low}} \equiv f_l(S_{l,\mathrm{low}})$ and $f_{l,\mathrm{high}} \equiv f_l(S_{l,\mathrm{high}})$, we then also know how the shock trajectory evolves, according to a Rankine-Hugoniot condition [60]

$$\mathrm{d}x_s/\mathrm{d}t = \Delta f_l/\Delta S_l = (f_{l,\mathrm{high}} - f_{l,\mathrm{low}})/(S_{l,\mathrm{high}} - S_{l,\mathrm{low}}). \tag{4.10}$$

We can use equation (4.10) to update the shock location x_s between a time t and $t + \delta t$, and then for the new location, solve (4.8)–(4.9) for updated $S_{l,\mathrm{low}}$ and $S_{l,\mathrm{high}}$. An updated shock location

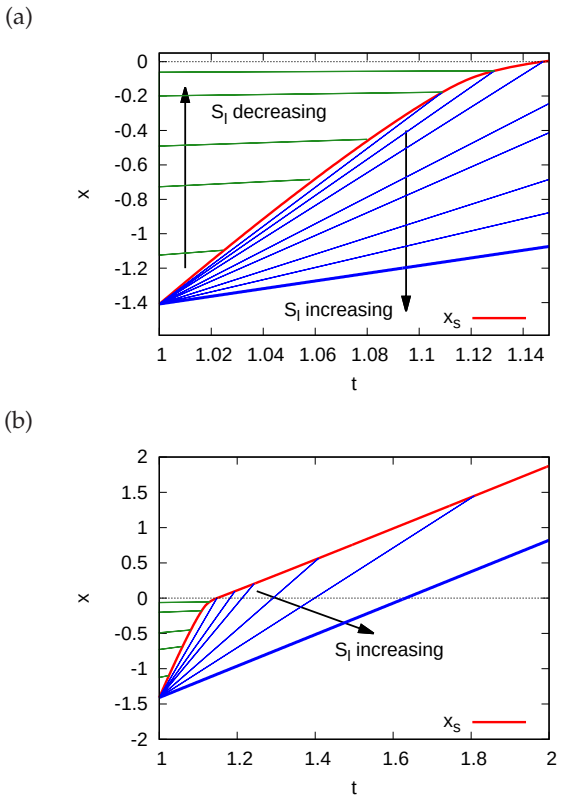

Figure 5. (a) Shock location x_s vs time t (shown as a curve) that separates two characteristic fans in the x-t plane (indicated by sets of straight lines). One fan with smaller S_l values is on the left (with S_l decreasing from bottom to top; S_l values plotted are 0.31, 0.305, 0.3, 0.2829, 0.1743, corresponding $M_{\rm tot}$ values are 3.3683, 3.8778, 4.2865, 5.0709, 6.8481). The other fan with larger S_l values is on the right, with S_l increasing from top to bottom; S_l values plotted are 0.369, 0.37, 0.3713, 0.374, 0.376, 0.38, 0.384 and $S_{l,{\rm rev},\infty} \equiv 0.3904$ (thicker line). Corresponding $M_{\rm tot}$ values are 0.1811, 0.1795, 0.1778, 0.1751, 0.1738, 0.1727, 0.1729 and 0.1751. Note that in the asymptotic limit as $t \to 1$ the shock starts out parallel to one of the characteristics in the fan on the right, specifically $S_l = S_{l,{\rm rev},0} \equiv 0.3672$. This is not plotted however as it only survives in the $t \to 1$ limit, and in that limit, it would be indistinguishable from the trajectory of the shock itself. (b) Zoomed out view of x_s vs t. When $x_s > 0$, only the characteristic fan on the right is relevant, and is plotted here with S_l values (from top to bottom) 0.3713, 0.374, 0.376, 0.38, 0.384 and $S_{l,{\rm rev},\infty} \equiv 0.3904$. Asymptotically as $t \to \infty$, the shock ends up parallel to this last mentioned characteristic.

for yet another time step can now be obtained using equation (4.10) and the process iterates. The result is plotted in Figure 5 (corresponding to a computation using a time step $\delta t = 0.001$): Figure 5(a) is a zoomed in view (for times just shortly after the instant of flow reversal), whereas Figure 5(b) is a zoomed out view (extending to rather longer times and hence larger x_s).

In order to obtain this solution, it is necessary to impose suitable initial conditions at $t = 1$. Not only (as already mentioned) is $x_s = x_{s,{\rm switch}}$ at this time, but also the value of $S_{l,{\rm low}}$ is necessarily $S_{l,{\rm fwd}}$ on the grounds that $x_{s,{\rm switch}}$ was determined by tracking a front with saturation $S_{l,{\rm fwd}}$ during the original forward flow mode. The initial value of $S_{l,{\rm high}}$ meanwhile is determined by recognising that in Figure 5(a), at $t = 1$ the trajectory of the shock in the x-t plane is initially parallel to a particular characteristic $S_{l,{\rm high}} = S_{l,{\rm rev},0}$ with

$$f_l'(S_{l,{\rm rev},0}) = (f_l(S_{l,{\rm rev},0}) - f_l(S_{l,{\rm fwd}}))/(S_{l,{\rm rev},0} - S_{l,{\rm fwd}}), \tag{4.11}$$

this value $S_l = S_{l,\mathrm{rev},0}$ also being indicated on the f_l vs S_l plot in Figure 3(a). We find $S_{l,\mathrm{rev},0} \approx 0.3672$. Note also in Figure 3(c) that the mobility M_{tot} at $S_{l,\mathrm{rev},0}$ is substantially lower than at $S_{l,\mathrm{fwd}}$, and lower even than the M_{tot} value for pure liquid (which is unity by definition).

The implication of equation (4.11) is that the "shock" strictly speaking starts out asymptotically as a contact discontinuity (in the x-t plane characteristics enter it from one side only, being parallel to it on the other side), and only evolves with time to become a true shock (characteristics enter it on both sides). What this means geometrically in Figure 5(a), is that if we select any characteristic in the left hand fan and follow it in the direction of increasing t, it is never parallel to the shock, and therefore must enter, i.e. intersect with, the shock. Meanwhile for the right hand fan, in the limit at $t \to 1$, the shock starts off parallel to one of the characteristics, which (moving in the direction of increasing t) initially prevents that characteristic and the shock from intersecting.

As the shock moves upwards over time, the liquid saturation on its "low" S_l side falls. This is indicated in Figure 5(a) (see the characteristics to the left of the shock) and is also shown directly in Figure 6(a). As $S_{l,\mathrm{low}}$ falls, the difference $\Delta S_l = S_{l,\mathrm{high}} - S_{l,\mathrm{low}}$ grows, for a relatively modest change in $\Delta f_l = f_{l,\mathrm{high}} - f_{l,\mathrm{low}}$ as Figure 7(a) makes clear. Via (4.10), a consequence is that $\mathrm{d}x_s/\mathrm{d}t$ falls, meaning the shock is necessarily a curve in the x-t plane (as Figure 5(a) shows), unlike the characteristics themselves which are straight lines. Once the shock trajectory starts to reorient over time, we can follow characteristics in the right hand fan in Figure 5(a) in the direction of increasing t and now see them entering, i.e. intersecting with, the shock. Moreover the intersection corresponds to characteristics with increasingly large $S_{l,\mathrm{high}}$ values as time proceeds. This is clear from Figure 5(a)–(b) and also from Figure 7(a)–(b). Values of $S_{l,\mathrm{high}}$ are plotted vs t in Figure 6(b). Note that (see Figure 5 and 7) the speed of the shock $\mathrm{d}x_s/\mathrm{d}t$ exceeds the slope of the characteristic $f_l'(S_{l,\mathrm{low}})$ on the "low" saturation side, but is less than the slope of the characteristic $f_l'(S_{l,\mathrm{high}})$ on the "high" saturation side: in Figure 5 therefore, characteristics do indeed enter the shock from sides. Comparisons between the shock speed and the speeds associated with characteristics either side of it are plotted vs time on Figure 8(a).

(d) Reverse flows at longer times and/or larger reverse displacements

Figure 5 indicates that, in our 1-D model, at a certain time the shock crosses over the location $x = 0$, meaning that, during the reverse flow phase, the shock has now covered the exact same distance spanned by the fan during the original forward flow phase. In the context of a 2-D pressure-driven growth model, certain points on a front would likely stop before they backtracked through a distance equivalent to the distance covered during an initial forward flow phase: in Figure 2(a) a point which, at the instant of flow reversal, was immediately below point B would be an example. It would only ever backtrack to the neutral depth, indicated in Figure 2(a) by a bold dashed line which happens to pass through point B. However other points can backtrack further than they moved forward initially. Point C is an example. It followed a relatively short curved path to reach its location in Figure 2(a) (close what was originally the bottom of the foam front) but upon flow reversal can backtrack all the way to the neutral depth (the bold dashed line). This is a 2-D picture of course in which depth influences net driving pressure difference, and hence the flux which that pressure difference generates. For the present however we focus on a 1-D model, in which the flux is specified, undergoing a change in sign but not in magnitude upon flow reversal.

In the 1-D system, how far the shock backtracks then depends upon how long the reverse flow phase persists: the shock x_s will always manage to cross over $x = 0$ provided the reverse flow phase persists for long enough. Since the shock that appears after $t = 1$ has a speed that is rather faster than the original forward flow during $t \leq 1$, this cross over happens well before $t = 2$ as Figure 5(a) shows, i.e. it happens well before the original "forward flow" fan focuses in completely upon itself. In our data $x_s = 0$ at time $t \approx 1.1476$. We denote this cross-over time t_{cross}.

The time t_{cross} signals a change in the structure of the solution for how S_l varies with x. This change can be inferred by tracing through the characteristic pattern in Figure 5 varying spatial coordinate x at any fixed time t: results of doing this at various times are plotted in Figure 9.

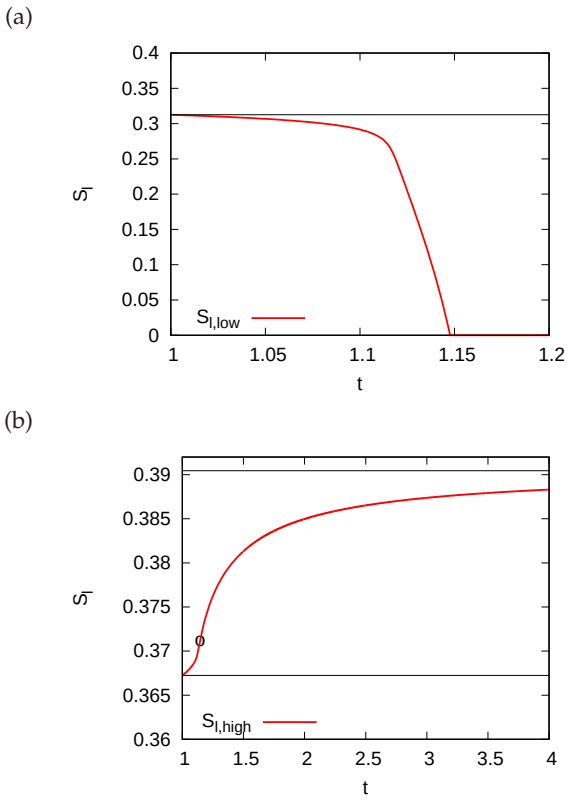

Figure 6. Liquid saturations either side of the shock vs time. (a) $S_{l,\mathrm{low}}$ vs t. The horizontal line denotes the value $S_{l,\mathrm{fwd}}$. (b) $S_{l,\mathrm{high}}$ vs t. The horizontal lines denote the values $S_{l,\mathrm{rev},0}$ and $S_{l,\mathrm{rev},\infty}$. The circle indicates the time $t_{\mathrm{cross}} \approx 1.1476$ at which the shock x_s crosses $x = 0$, which is also the time at which $S_{l,\mathrm{low}}$ falls to zero. The corresponding $S_{l,\mathrm{high}}$ value at this particular time is $S_{l,\mathrm{high}} \approx 0.3713$.

During the reverse flow at some time t greater than unity but prior to time t_{cross}, sufficiently far upstream i.e. for $x \leq x_{s,\mathrm{switch}}$ we have pure liquid (or more generally a maximum liquid saturation beyond which gas is irreducible), whereas sufficiently far downstream for $x \geq 0$ we have pure gas (or more generally irreducible liquid). As we move from $x = x_{s,\mathrm{switch}}$ to $x = 0$, the value of S_l (see Figure 9) falls continuously through the fan from $S_l = 1$ down to $S_l = S_{l,\mathrm{high}}$, then it jumps immediately to $S_{l,\mathrm{low}}$ at the shock $x = x_s$, and subsequently falls continuously through the fan to $S_l = 0$. This rather complex S_l vs x profile therefore follows from the complex double fan structure that is developed around the shock.

After time t_{cross} however, on the "low" saturation side of the shock, $S_{l,\mathrm{low}}$ has already fallen to zero (or more generally to an irreducible S_l). The S_l vs x profile in Figure 9 now changes, with S_l falling to zero immediately downstream of the shock. The shock now invades an entirely gas filled region, rather than invading a mixed gas-liquid fan that developed during the original forward flow phase. Only a single fan remains relevant now (i.e. the fan on the "high" saturation side of the shock), with S_l falling continuously from $S_l = 1$ at $x = x_{s,\mathrm{switch}}$ to $S_{l,\mathrm{high}}$ at $x = x_s$. Since the shock velocity $\Delta f_l / \Delta S_l$ (which reduces to $f_{l,\mathrm{high}}/S_{l,\mathrm{high}}$ under the present circumstances), remains less than the slope of the characteristic $f_l'(S_{l,\mathrm{high}})$ (this can be seen in Figure 5(b)) the shock continues to evolve towards higher and higher values of $S_{l,\mathrm{high}}$. However increasing $S_{l,\mathrm{high}}$ (with $S_{l,\mathrm{low}}$ fixed at zero), tends to increase the speed of the shock, as is seen in Figure 8(b): the shock decelerates between $t = 1$ and $t = t_{\mathrm{cross}}$, but accelerates again after t_{cross}.

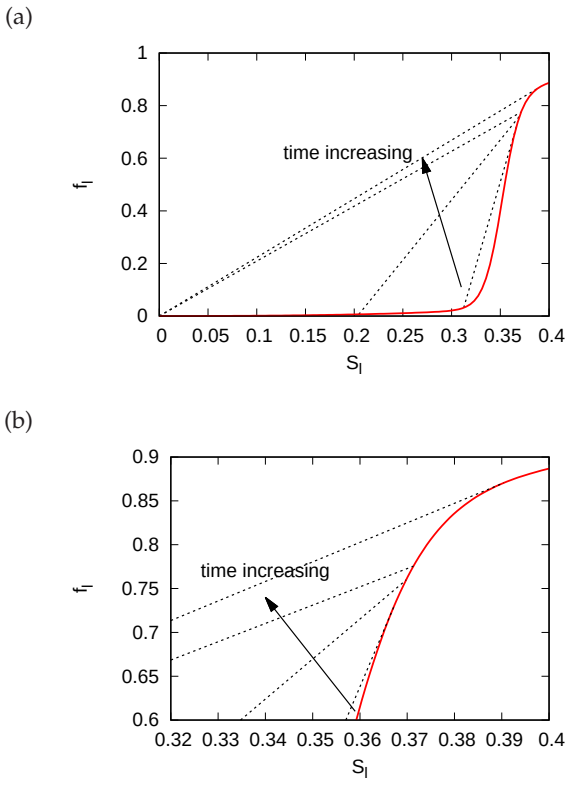

Figure 7. (a) Fractional flow curve f_l vs S_l with dashed lines drawn indicating (at various times) the shock joining $(S_{l,\mathrm{low}}, f(S_{l,\mathrm{low}}))$ to $(S_{l,\mathrm{high}}, f(S_{l,\mathrm{high}}))$. The specific times corresponding to the dashed lines are $t = 1$ (the instant of flow reversal), $t = 1.125$, $t = 1.1476$ (the instant t_{cross} at which $x_s = 0$ and $S_{l,\mathrm{low}}$ falls to zero), and $t \to \infty$. (b) Zoomed view, showing in particular how $S_{l,\mathrm{high}}$ grows over time. Note that the high S_l end of the shock (dashed line) is only tangent to the fractional flow curve when $t = 1$ and when $t \to \infty$, but not for intermediate times.

There is however a limit to how much the shock can accelerate. The system asymptotes to a S_l value that we denote $S_{l,\mathrm{rev},\infty}$ at which the shock speed matches the speed of a characteristic

$$f_l'(S_{l,\mathrm{rev},\infty}) = f_l(S_{l,\mathrm{rev},\infty})/S_{l,\mathrm{rev},\infty}. \tag{4.12}$$

The value of $S_{l,\mathrm{rev},\infty}$ is indicated on Figure 3(a). As the shock asymptotes to this particular characteristic, at long times the shock evolves towards a contact discontinuity again, albeit a different contact discontinuity from what was seen at the instant of flow reversal. Note that this contact discontinuity with $S_l = S_{l,\mathrm{rev},\infty}$ corresponds to what we would have in a situation in which the front underwent a reverse flow (i.e. liquid pushed into gas) without any initial forward flow phase. At sufficiently long times therefore, the reverse flow has proceeded for long enough that the initial forward flow phase no longer has a bearing on the solution.

(e) Pressure required to drive fractional flow

So far our analysis of the 1-D fractional flow model has considered a specified flux of fluids (liquid plus gas) denoted q in dimensional variables, but has not considered anything about the pressure difference needed to drive though fluids along. This pressure difference (reverting to dimensional variables) is given by $\Delta p = \int q/(k\mathcal{M}_{\mathrm{tot}})\,\mathrm{d}x \equiv \int q\mu_l/(kM_{\mathrm{tot}})\,\mathrm{d}x$ where the integral needs to proceed from an upstream location to a downstream one (we leave the exact integration

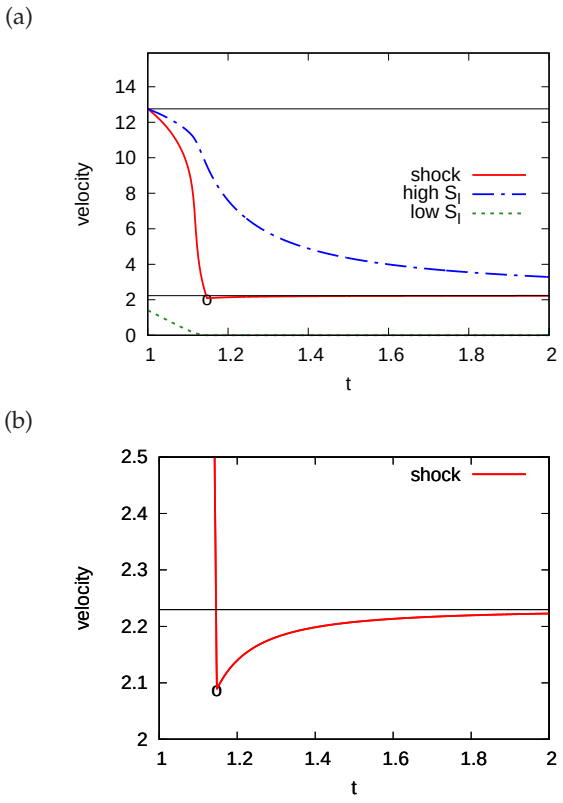

Figure 8. (a) Speed of the shock compared with speed of characteristics on both the high S_l side of the shock and the low S_l side. The horizontal lines indicate the initial and final speeds of the shock (which coincide with the speeds of the characteristics respectively at $S_{l,\mathrm{rev},0}$ and $S_{l,\mathrm{rev},\infty}$). The circle indicates the time t_{cross} at which the shock x_s crosses $x_s = 0$, which is also the time at which $S_{l,\mathrm{low}}$ falls to zero. (b) Zoomed view showing just the shock velocity.

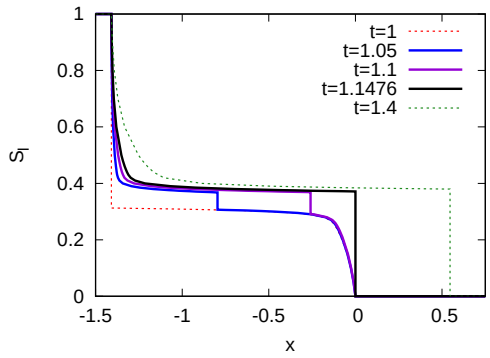

Figure 9. Plot of S_l vs x at various times, $t = 1$ (the instant of flow reversal), $t = 1.05$, $t = 1.1$, $t = 1.1476$ (the time t_{cross} at which the shock location x_s crosses zero) and $t = 1.4$.

limits unspecified for the moment). Remembering that distances can be non-dimensionalised on a scale $t_r|q|/\phi$, and supposing we define $\Delta\mathcal{P}$ via $\Delta p = \mu_l q^2 t_r/(k\phi)\Delta\mathcal{P}$, a dimensionless analogue is obtained (for compactness of notation, using x now to denote dimensionless coordinate)

$$\Delta\mathcal{P} = \int \mathrm{d}x/M_{\mathrm{tot}}. \tag{4.13}$$

Here M_{tot} is a known function of liquid saturation S_l (see Figure 3(b)), but (at any dimensionless time t), S_l is also a known function of dimensionless coordinate x.

For the data used here, values of M_{tot} vs S_l are plotted in Figure 3(b)–(c) and have already been discussed back in section 3(d). Recall that pure gas is ten times more mobile here than pure liquid, so that as S_l increases, M_{tot} tends to decrease. Moreover, at a certain S_l value, recall that M_{tot} exhibits a sharp decrease due to the presence of foam. The total mobility for any higher S_l values is then almost entirely accounted for by the liquid relatively mobility alone (as is seen in Figure 3(c)), but this can still be rather less than the mobility of pure liquid. Mixtures of gas and liquid can thereby have substantially lower mobility than either pure liquid or pure gas.

If gas-liquid mixtures found within characteristic fans thereby make the dominant contribution to the pressure drop, it is possible to change the integration variable from x to S_l leading to

$$\Delta\mathcal{P} \approx \int_0^{S_{l,\mathrm{low}}} \frac{1}{M_{\mathrm{tot}}} \left|\frac{\mathrm{d}x}{\mathrm{d}S_l}\right| \mathrm{d}S_l + \int_{S_{l,\mathrm{high}}}^1 \frac{1}{M_{\mathrm{tot}}} \left|\frac{\mathrm{d}x}{\mathrm{d}S_l}\right| \mathrm{d}S_l. \tag{4.14}$$

The integral is divided into two parts, one for each fan (assuming time t is less than t_{cross}, otherwise just a single fan, i.e. the "high" S_l fan, is relevant). In the low S_l fan, $x = -f_l'(S_l)(2-t)$ whereas in the high S_l fan, $x = f_l'(S_l)(t-1) + x_{s,\mathrm{switch}}$. Equation (4.14) therefore becomes

$$\Delta\mathcal{P} \approx \int_0^{S_{l,\mathrm{low}}} \frac{1}{M_{\mathrm{tot}}(S_l)} |f_l''(S_l)|(2-t)\,\mathrm{d}S_l + \int_{S_{l,\mathrm{high}}}^1 \frac{1}{M_{\mathrm{tot}}(S_l)} \left|f_l''(S_l)\right| (t-1)\,\mathrm{d}S_l. \tag{4.15}$$

The exact values of the integrals in the above depend on the functional forms of M_{tot} and f_l''. These integrals are quite complex, since at first sight S_l values with the smallest M_{tot} should contribute the most, but these also tend to have smallest f_l'' (close to the inflection point of f_l). Close to the inflection point, moderate changes in S_l produce only very small changes in x implying a limited contribution to pressure drop.

Despite this complexity, what is clear however is that early on, i.e. immediately after the instant of flow reversal $t = 1$, the pressure drop is dominated by the first integral (arising from the "low" S_l fan) since the second integral (from the "high" S_l fan) vanishes. As time proceeds however, the balance necessary shifts from the first to the second integral, partly because of the factor $2 - t$ decreasing whilst $t - 1$ increases, but also because of the integration limit $S_{l,\mathrm{low}}$ in the first integral falling towards zero. By the time $t = t_{\mathrm{cross}}$ at which x_s crosses over $x = 0$, the value of $S_{l,\mathrm{low}}$ has fallen to zero, and so only the second integral survives.

One way of approximating these complex integrals, is to revert to equation (4.13), but integrating now in two sections from $x = x_s$ to $x = 0$ (the low S_l fan) and from $x = x_{s,\mathrm{switch}}$ to $x = x_s$ (the high S_l fan). Hence

$$\Delta\mathcal{P} \approx \int_{x_s}^0 \frac{1}{M_{\mathrm{tot}}(S_l(x))}\,\mathrm{d}x + \int_{x_{s,\mathrm{switch}}}^{x_s} \frac{1}{M_{\mathrm{tot}}(S_l(x))}\,\mathrm{d}x. \tag{4.16}$$

On each fan the lowest M_{tot} values arise from the S_l values closest to the shock (i.e. from the values $S_{l,\mathrm{low}}$ and $S_{l,\mathrm{high}}$). Given that these are the lowest values of mobility M_{tot}, they make the largest contribution to each integral in equation (4.16). We now suppose that M_{tot} stays close to these lowest mobility values over a fraction $\varepsilon \ll 1$ of each integration domain (the shaded regions in Figure 2(b) represent these portions of the domain schematically), and we suppose that M_{tot} is much larger in other parts of the integration domain. Hence the integrals can be assumed to

	$R_f = 185$	$R_f = 1850$	$R_f = 18500$
$S_{l,\mathrm{fwd}}$	0.3124	0.2911	0.2700
$f_l(S_{l,\mathrm{fwd}})$	0.0316	0.0278	0.0245
$M_{\mathrm{tot,fwd}}$	*3.0861*	*3.0473*	*2.9692*
$S_{l,\mathrm{infl}}$	0.3520	0.3317	0.3107
$M_{\mathrm{tot,infl}}$	0.2786	0.2199	0.1906
$S_{l,\mathrm{rev},0}$	0.3672	0.3468	0.3258
$f_l(S_{l,\mathrm{rev},0})$	0.7302	0.8253	0.8382
$M_{\mathrm{tot,rev},0}$	0.1846	0.1457	0.1266
$S_{l,\mathrm{min\ mob}}$	0.3811	0.3586	0.3368
$M_{\mathrm{tot,min}}$	0.1727	0.1377	0.1202
$S_{l,\mathrm{rev},\infty}$	0.3904	0.3657	0.3436
$f_l(S_{l,\mathrm{rev},\infty})$	0.8705	0.9604	0.9714
$M_{\mathrm{tot,rev},\infty}$	0.1751	0.1392	0.1215

Table 2. Key liquid saturations ($S_{l,\mathrm{fwd}}$, $S_{l,\mathrm{infl}}$, $S_{l,\mathrm{rev},0}$, $S_{l,\mathrm{min\ mob}}$, $S_{l,\mathrm{rev},\infty}$) and associated total mobilities ($M_{\mathrm{tot,fwd}}$, $M_{\mathrm{tot,infl}}$, $M_{\mathrm{tot,rev},0}$, $M_{\mathrm{tot,min}}$, $M_{\mathrm{tot,rev},\infty}$) for different values of the foam mobility reduction factor R_f. We consider here not only the base case value $R_f = 185$, but also higher values $R_f = 1850$ and $R_f = 18500$ (discussed further in supplementary material). Any total mobility values shown in italics actually exceed the mobility of pure liquid (normalised to unity here). It is only for total mobilities (not in italics) that are substantially smaller than unity that it is reasonable to suppose the the bulk of the dissipative pressure drop occurs close to the foam front. A number of f_l values are also reported, specifically for $S_{l,\mathrm{fwd}}$, $S_{l,\mathrm{rev},0}$ and $S_{l,\mathrm{rev},\infty}$, these f_l values being needed to determine shock speeds via the Rankine-Hugoniot condition.

evaluate to

$$\Delta\mathcal{P} \approx \frac{|x_s|\varepsilon}{M_{\mathrm{tot}}(S_{l,\mathrm{low}})} + \frac{|x_s - x_{s,\mathrm{switch}}|\varepsilon}{M_{\mathrm{tot}}(S_{l,\mathrm{high}})} \tag{4.17}$$

where the first term on the right hand side is only relevant when $x_s < 0$ (otherwise the term is discarded, which follows because, when $x_s > 0$ there is no longer a fan on the "low" S_l side of the shock, only on the "high" S_l side; see Figure 5(b)). Provided $x_s < 0$, so that both terms on the right hand side are included, we *assume* here (for simplicity) that the same value ε is applicable on both sides of the shock, although this could be generalised to having different ε values on the "low" and "high" side.

We now approximate further by assuming that at all times, $M_{\mathrm{tot}}(S_{l,\mathrm{low}})$ can be estimated by $M_{\mathrm{tot}}(S_{l,\mathrm{fwd}})$ (hereafter denoted $M_{\mathrm{tot,fwd}}$), and $M_{\mathrm{tot}}(S_{l,\mathrm{high}})$ can be estimated by $M_{\mathrm{tot}}(S_{l,\mathrm{rev},\infty})$ (hereafter denoted $M_{\mathrm{tot,rev},\infty}$). The latter approximation is a relatively good one, since M_{tot} changes relatively little as $S_{l,\mathrm{high}}$ evolves from $S_{l,\mathrm{rev},0}$ to $S_{l,\mathrm{rev},\infty}$ (see Table 2 and also Figure 3(c)). This follows because both $S_{l,\mathrm{rev},0}$ and $S_{l,\mathrm{rev},\infty}$ tend to be close to a value that we denote $S_{l,\mathrm{min\ mob}}$ at which mobility M_{tot} reaches an overall minimum $M_{\mathrm{tot,min}}$. The former approximation is less robust, although significant falls in $S_{l,\mathrm{low}}$ below $S_{l,\mathrm{fwd}}$ leading in turn to significant rises in M_{tot} (see Figure 3(c)) only tend to happen for (dimensionless) times bigger than about 1.1 (see Figure 6(a)) by which time $|x_s|$ has shrunk to around 20% of the original value it had at unit time (see Figure 5(a)). This makes the first term on the right hand side of equation (4.17) relatively unimportant anyway.

If we rearrange equation (4.17) and convert it back in terms of dimensional pressure and dimensional coordinate, we deduce

$$q = \frac{k\,\Delta p}{\mu_l}\left(\frac{|x_s|\varepsilon}{M_{\mathrm{tot,fwd}}} + \frac{|x_s - x_{s,\mathrm{switch}}|\varepsilon}{M_{\mathrm{tot,rev},\infty}}\right)^{-1} \tag{4.18}$$

where again the first term in parentheses on the right hand side is only relevant to situations in which $x_s < 0$, otherwise the term is discarded.

(f) Implications of the pressure drop vs flux relation

Equation (4.18) allows us to relate the total fluid flux q to an imposed pressure difference Δp for a 1-D forward-and-reverse fractional flow: the consequences of this equation are now explored. Immediately after flow switches from forward to reverse flow mode, $|x_s - x_{s,\mathrm{switch}}| \gg |x_s|$, so the first term on the right hand side of (4.18) dominates the second: the bulk of the pressure drop occurs across the reflection of the original characteristic fan that was developed during forward flow. As time proceeds however $|x_s|$ decreases whilst $|x_s - x_{s,\mathrm{switch}}|$ grows, so the balance within (4.18) shifts from the first to the second term. Moreover this shift can actually happen quite quickly even before x_s has displaced very far from $x_{s,\mathrm{switch}}$, since $M_{\mathrm{tot,rev},\infty}$ tends to be significantly smaller than $M_{\mathrm{tot,fwd}}$, as Figure 3(c) and Table 2 show.

In fact for the system we are currently considering it turns out that $M_{\mathrm{tot,fwd}}$ is actually larger than unity (see Table 2). This means that the total mobility associated with the forward flow characteristic fan that develops when gas propagates into liquid (i.e. a fan with relatively high saturations of gas, but relatively low saturations of liquid up to $S_{l,\mathrm{fwd}}$) is actually *greater* than the mobility of pure liquid (since pure liquid has $M_{\mathrm{tot}} \equiv 1$ by definition). Saturations which produce much lower mobilities, whilst they exist in principle within Figure 3(c), are not being selected in forward flow mode, at least not in forward flow mode with our current parameter set.

This has a number of implications. It means for instance that, for our parameter set, the pressure drop across parts of the flow domain that are entirely filled with liquid cannot necessarily be neglected, despite one of the assumptions used to justify pressure-driven growth [40] having been that the mobility of mixed gas-liquid flows (within characteristic fans) is much lower than the mobility of pure liquid or pure gas flows outside fans. Nevertheless under circumstances with $M_{\mathrm{tot,fwd}} > 1$, equation (4.18) can still be considered applicable to determine total fluid fluxes q but Δp now needs to be interpreted to mean pressure drop applied across the characteristic fan region, which will generally be less than the pressure drop applied across the entire flow field.

Moreover in the situation of interest here, any issues with applicability of equation (4.18) gradually resolve themselves over time. During forward and reverse flow, we know that a second characteristic fan is produced upon the instant of flow reversal. This fan (corresponding to pushing liquid into a gas-liquid mixture) has relatively high liquid saturations and the mobility $M_{\mathrm{tot,rev},\infty}$ that we associate with it really does satisfy $M_{\mathrm{tot,rev},\infty} \ll 1$ (see Table 2). It is then reasonable to suppose that the bulk of any imposed pressure drop really does occur across that particular characteristic fan. Whereas $S_{l,\mathrm{fwd}}$ corresponds a point at which M_{tot} in the presence of foam is still relatively high, but is just beginning to fall below M_{tot} in the absence of foam, by way of contrast $S_{l,\mathrm{rev},\infty}$ gives a M_{tot} value in the presence of foam that is very much smaller and actually close to a global minimum. Ironically then, despite the 2-D pressure-driven growth model having been developed originally for a forward flow situation, the underlying 1-D fractional-flow theory implies via equation (4.18) that the assumption underlying pressure-driven growth (i.e. the assumption that $M_{\mathrm{tot}} \ll 1$ for mixed liquid and gas flow) is actually more robust in a forward and reverse flow situation such as we consider here. The way to use equation (4.18) to generalise pressure-driven growth to a forward and reverse flow mode is discussed next.

(g) Forward and reverse flow: Pressure-driven growth

In a 2-D pressure-driven growth scenario, consider a situation in which an initial injection pressure P_{inj} suddenly reduced to a multiple $(1-\chi)$ of its original value for some $\chi < 1$. If the injection pressure and hydrostatic pressure originally came into balance at a unit dimensionless depth below the top of the foam front, they will now come into balance at a depth of $(1-\chi)$ units, i.e. at a location χ units higher up than before. If we then set, as before, the zero of our coordinate vertical system at the original "neutral" depth at which injection pressure and hydrostatic pressure originally balanced, the new "neutral" Y location shifts to $Y_{\mathrm{neut}} = \chi$: this is indicated schematically by the bold dashed line in Figure 2(a) which has shifted upwards relative to what was originally the bottom of the front. For any points satisfying $Y > Y_{\mathrm{neut}}$,

equation (4.4) continues to apply, just with a new formula for (dimensionless) net driving pressure. In dimensionless form we have $\mathrm{d}\boldsymbol{X}/\mathrm{d}\tau = ((Y - Y_{\mathrm{neut}})/s)\,\boldsymbol{n}$.

The situation described above is a minor modification of conventional pressure-driven growth, so we do not consider it any further. Instead points satisfying $Y < Y_{\mathrm{neut}}$ are of interest here. For such points it is convenient upon flow reversal to switch the direction of the front normal (so as to align it with the direction of the arrows shown in Figure 2(a)), ensuring it continues to point along the direction in which net pressure decreases, which is now from liquid towards gas. For any given point with $Y < Y_{\mathrm{neut}}$, we define a distance s_{switch} that it displaced up to the point at which flow reversal occurred, and we also define a distance s_{since} that it has backtracked since flow reversal.

We are now in a position to generalize equation (4.18) to a situation of 2-D pressure-driven growth recognising that s_{switch} can be identified with $|x_{s,\mathrm{switch}}|$ in that equation, whereas s_{since} can be identified with $|x_s - x_{s,\mathrm{switch}}|$. We therefore deduce (in dimensional variables)

$$\boldsymbol{q} \equiv q\,\boldsymbol{n} = \frac{k\,\Delta P}{\mu_l}\left(\frac{|s_{\mathrm{switch}} - s_{\mathrm{since}}|\varepsilon}{M_{\mathrm{tot,fwd}}} + \frac{s_{\mathrm{since}}\varepsilon}{M_{\mathrm{tot,rev},\infty}}\right)^{-1}\boldsymbol{n}. \tag{4.19}$$

This applies to points satisfying $s_{\mathrm{since}} < s_{\mathrm{switch}}$, i.e. that have backtracked less than they moved in the original forward flow phase. During pressure-driven growth, some points satisfy this constraint at all times, e.g. in Figure 2(a) points that start backtracking just slightly below point B will reach the neutral depth, indicated by the horizontal bold dashed line in Figure 2(a) (at which point s_{since} stops evolving), long before s_{since} (the distance backtracked) is anywhere near s_{switch} (the distance moved forward originally). Other points however (point C in Figure 2(a) for instance) potentially backtrack further than they moved forward initially. Analogously with what we saw for equation (4.18), once $s_{\mathrm{since}} > s_{\mathrm{switch}}$, the first term in the parenthesis on the right hand side of equation (4.19) is discarded, and only the second term survives.

Equation (4.19) gives a total fluid flux, but not yet the velocity at which a pressure-driven growth front propagates. To establish this we draw an analogy with equation (4.2) to deduce (again in dimensional variables)

$$\frac{\mathrm{d}\boldsymbol{X}}{\mathrm{d}\tau} = \frac{q}{\phi}\frac{\Delta f_l}{\Delta S_l}\boldsymbol{n}. \tag{4.20}$$

This recognizes that what we are now tracking is a shock with speed $(q/\phi)\Delta f_l/\Delta S_l$ with Δf_l and ΔS_l being jumps in fractional flow and in liquid saturation across the shock. This therefore generalises equation (4.2) (forward flow mode) in which a contact discontinuity propagated with speed $(q/\phi)(1 - f_l)/(1 - S_l)$.

Combining equation (4.19) and (4.20) gives

$$\frac{\mathrm{d}\boldsymbol{X}}{\mathrm{d}\tau} = \frac{k\,\Delta P}{\phi\mu_l}\left(\frac{|s_{\mathrm{switch}} - s_{\mathrm{since}}|\varepsilon}{M_{\mathrm{tot,fwd}}} + \frac{s_{\mathrm{since}}\varepsilon}{M_{\mathrm{tot,rev},\infty}}\right)^{-1}\frac{\Delta f_l}{\Delta S_l}\boldsymbol{n}. \tag{4.21}$$

It is clear from the results of Figure 6–7 that Δf_l and ΔS_l are functions of time since flow reversal. However the data of Figure 5 indicate that to a reasonable approximation

$$\Delta f_l/\Delta S_l \approx (f_{l,\mathrm{rev},0} - f_{l,\mathrm{fwd}})/(S_{l,\mathrm{rev},0} - S_{l,\mathrm{fwd}}) \tag{4.22}$$

provided $x_s < 0$ (i.e. provided $s_{\mathrm{since}} < s_{\mathrm{switch}}$), whereas

$$\Delta f_l/\Delta S_l \approx f_{l,\mathrm{rev},\infty}/S_{l,\mathrm{rev},\infty} \tag{4.23}$$

if $x_s > 0$ (i.e. $s_{\mathrm{since}} > s_{\mathrm{switch}}$).

In dimensionless form (using the same dimensionless scales as used back in section (a), and retaining the same symbols $\boldsymbol{X}$ and τ for compactness of notation) equation (4.21) now reduces to

$$\frac{\mathrm{d}\boldsymbol{X}}{\mathrm{d}\tau} = |Y - Y_{\mathrm{neut}}|\left(|s_{\mathrm{switch}} - s_{\mathrm{since}}| + s_{\mathrm{since}}\frac{M_{\mathrm{tot,fwd}}}{M_{\mathrm{tot,rev},\infty}}\right)^{-1}\frac{(f_{l,\mathrm{rev},0} - f_{l,\mathrm{fwd}})}{(S_{l,\mathrm{rev},0} - S_{l,\mathrm{fwd}})}\frac{(1 - S_{l,\mathrm{fwd}})}{(1 - f_{l,\mathrm{fwd}})}\boldsymbol{n} \tag{4.24}$$

which applies for $Y < Y_{\rm neut}$ and $s_{\rm since} < s_{\rm switch}$. Here $|Y - Y_{\rm neut}|$ is the dimensionless analogue of ΔP, while equation (4.22) has been used as an approximation for $\Delta f_l/\Delta S_l$. Meanwhile for a situation in which $s_{\rm since} > s_{\rm switch}$ (still with $Y < Y_{\rm neut}$), we have instead

$$\frac{{\rm d}\boldsymbol{X}}{{\rm d}\tau} = |Y - Y_{\rm neut}| \frac{M_{\rm tot,rev,\infty}}{M_{\rm tot,fwd}\, s_{\rm since}} \frac{f_{l,{\rm rev},\infty}}{S_{l,{\rm rev},\infty}} \frac{(1 - S_{l,{\rm fwd}})}{(1 - f_{l,{\rm fwd}})} \boldsymbol{n}. \tag{4.25}$$

Here we only need to consider a low mobility fan growing proportionally to $s_{\rm since}$ located behind the shock, but without any fan surviving ahead of it, which is why terms in $|s_{\rm switch} - s_{\rm since}|$ have been discarded. Also equation (4.23) has been used in place of (4.22). The value of $s_{\rm switch}$ (dimensionless distance travelled up to the instant of flow reversal) is inherited from the original forward flow propagation of the front, whilst the value of $s_{\rm since}$ (dimensionless distance travelled since flow reversal) satisfies

$$ {\rm d}s_{\rm since}/{\rm d}\tau = ({\rm d}\boldsymbol{X}/{\rm d}\tau).\boldsymbol{n} \tag{4.26}$$

with $s_{\rm since} = 0$ at the instant of flow reversal.

Equations (4.24)–(4.26) are the key results in this paper, providing a well-defined way to generalise pressure-driven growth to the case of flow reversal. We make the following observations. As already noted in section (f), via Table 2, the ratio $M_{\rm tot,fwd}/M_{\rm tot,rev,\infty}$ tends to be considerably larger than unity, meaning that within the parentheses in equation (4.24), the second term can dominate the first term even for $s_{\rm since}$ values considerably smaller than $|s_{\rm switch} - s_{\rm since}|$, i.e. even for a front that has backtracked by a relatively small amount. This follows because the set of liquid saturations adjacent to the backtracking front tend to be associated with much lower mobility than those associated with the original forward propagating front.

As far as the front propagation is concerned, these lower mobilities (reducing total fluid flux and hence front propagation rate), are partly offset by another effect, namely that, for a specified total fluid flux, the backtracking shock tends to move faster than the original forward propagating front would do. This is seen by the ratio between $(f_{l,{\rm rev},0} - f_{l,{\rm fwd}})/(S_{l,{\rm rev},0} - S_{l,{\rm fwd}})$ and $(1 - f_{l,{\rm fwd}})/(1 - S_{l,{\rm fwd}})$ in equation (4.24), this ratio having a value rather larger than unity (see slopes of lines plotted in Figure 3(a) with relevant data given in Table 2). Note also that if the front ever manages to backtrack by further than it originally moved forward, a significant reduction in propagation speed is predicted to occur (see e.g. Figure 5(b)). The relevant ratio in equation (4.25) is that between $f_{l,{\rm rev},\infty}/S_{l,{\rm rev},\infty}$ and $(1 - f_{l,{\rm fwd}})/(1 - S_{l,{\rm fwd}})$ (again see Figure 3(a) and Table 2), which although slightly greater than unity, is not nearly big enough to compensate for the backtracking mobility $M_{\rm tot,rev,\infty}$ being much smaller than $M_{\rm tot,fwd}$.

5. Conclusions

To conclude, equations (4.24)–(4.26) taken together constitute a model for what happens in 2-D pressure-driven growth in situations in which a flow reversal occurs due to a reduction in driving pressure. Under circumstances like these, whereas gas pushes into liquid initially, later on liquid pushes back into gas. In fact only parts of the front at depth undergo the flow reversal. Points higher up on the front (above a "neutral" depth) do not undergo flow reversal, and continue to be described by the original fractional flow equation (4.4), just with a reduced net driving pressure. In realistic oil recovery applications, operations are designed such that most of the oil is likely to be encountered higher up (i.e. above the "neutral depth") so any reverse flow at depth tends to involve other fluids (e.g. water invading foamed gas).

The reverse flow model for 2-D pressure-driven growth associates each point on the 2-D front with local 1-D motion of a shock described by an underlying 1-D fractional-flow theory. Moreover the 2-D model captures key features of the underlying 1-D theory: during reverse flow there is a complex double fan structure either side of a shock, with comparatively low liquid saturations downstream of the shock (these saturations also appear during the forward flow) and comparatively high liquid saturations upstream (saturations that do not appear during forward flow). The lowest mobilities are associated with the higher liquid saturations near the upstream

side of the shock, so it is this side that determines how rapidly fluids (i.e. liquid plus gas) can flow, and hence how fast the 1-D shock or equivalently 2-D front propagates. Even though the 1-D model feeds into the 2-D one, there is (unlike in 1-D) no requirement in the 2-D model for points to retrace the same trajectory during reverse flow as they executed during forward flow.

In this work we have presented equations (4.24)–(4.26) but not attempted to solve them, leaving that task for further work. What we do know is that any material point on the front, tracked to long enough time, should eventually attain the aforementioned "neutral" depth at which its motion stops. The model described by equations (4.24)–(4.26) however indicates how quickly material points evolve towards that final neutral depth. Such evolution might however be less straightforward than is initially apparent. The backtracking portion of the front has a concave shape seen from the direction towards which it is moving. It is already known [41] for the pressure-driven growth model that concavities have the potential to focus down into sharp corners, which physically correspond to regions over which a foam front reorients direction over a distance scale much less than the overall extent of the front. Whether or not this sort of behaviour is prominent when equations (4.24)–(4.26) are solved still remains to be seen.

Another task for further work concerns how well the flow-reversed pressure-driven growth model (4.24)–(4.26) (which assigns dissipative pressure drops entirely to a low mobility foam front) would compare with a simulation based on Darcy's law (which distributes pressure drops over the entire flow domain). The indications from the results presented here are that mobilities at the foam front are even lower in reverse flow mode than in forward flow, a result that follows from having different saturations in forward and reverse flows, even assuming the same underlying fractional flow curve in both situations as has been done here. It follows thereby that agreement between a pressure-driven growth model and a Darcy simulation can be expected to be better in reverse flow than in a forward flow mode.

Nonetheless difficulties remain even in reverse flow mode. We have stated that validity of the pressure-driven growth model assumes the low mobility region at the foam front is thin compared to the distance the front itself displaces. This applies not just in forward flow but in reverse flow also. Indeed in reverse flow the requirement to have a thin front is particularly delicate. Suppose that an arbitrarily thin front is replaced by a small but finite thickness region near the front, and then flow reverses and the system starts to backtrack. Points with different saturations within that small but finite thickness region then start to interact not just with points on the specific path that was executed to reach one particular location on the front (e.g. point C in Figure 2), but also with points (and their corresponding saturations) on neighbouring paths executed to reach neighbouring locations on the front. This represents a considerable complication.

Ethics. This paper does not raise any ethical issues.

Data Accessibility. Programs used to generate results and data obtained from them are supplied as supplementary material.

Authors' Contributions. P. Grassia (PG) suggested the research problem to M. Eneotu (ME), for ME to tackle as part of his PhD project (under PG's supervision). ME conceived the technique for obtaining the solution, and implemented it (albeit, for a set of parameter values different from those reported here). ME wrote up that work as chapters within his PhD thesis. PG then implemented the solution for the actual set of parameter values reported here and assisted with re-drafting ME's written work into journal article format. Both authors approved the final version and agree to be accountable for all aspects the work.

Competing Interests. We declare we have no competing interests.

Funding. M. Eneotu was funded by the Petroleum Technology Development Fund (PTDF), Nigeria.

Acknowledgements. P. Grassia acknowledges useful discussions with I. Frigaard, who (some years ago now) enquired what might happen to pressure-driven growth under flow reversal.

References

1. Lake LW, Johns R, Rossen WR, Pope G. 2014 *Fundamentals of Enhanced Oil Recovery*. Richardson, TX: Society of Petroleum Engineers.
2. Willhite GP. 1986 *Waterflooding*. Richardson, TX: Society of Petroleum Engineers.
3. Green DW, Willhite GP. 1998 *Enhanced Oil Recovery*. Richardson, TX: Society of Petroleum Engineers.
4. Farajzadeh R. 2009 *Enhanced Transport Phenomena in CO_2 Sequestration and CO_2 EOR*. PhD thesis Delft University of Technology.
5. Sorbie KS. 1991 *Polymer-Improved Oil Recovery*. Glasgow: Blackie & Son.
6. Schramm LL, Wassmuth F. 1994 Foams: Basic Principles. In Schramm LL, editor, *Foams: Fundamentals and Applications in the Petroleum Industry* vol. 242 *Advances in Chemistry* pp. 3–45. Washington, DC: American Chemical Society.
7. Kovscek AR, Radke CJ. 1994 Fundamentals of Foam Transport in Porous Media. In Schramm LL, editor, *Foams: Fundamentals and Applications in the Petroleum Industry* vol. 242 *Advances in Chemistry* pp. 115–163. Washington, DC: American Chemical Society.
8. Rossen WR. 1996 Foams in Enhanced Oil Recovery. In Prud'homme RK, Khan SA, editors, *Foams: Theory, Measurements and Applications* Surfactant Science Series pp. 99–187. New York: Marcel Dekker.
9. Farajzadeh R, Andrianov A, Krastev R, Hirasaki GJ, Rossen WR. 2012 Foam-oil interaction in porous media: Implications for foam assisted enhanced oil recovery. *Adv. Coll. Interface Sci.* **183–184**, 1–13. doi.org/10.1016/j.cis.2012.07.002.
10. Cottin C, Bodiguel H, Colin A. 2010 Drainage in two-dimensional porous media: From capillary fingering to viscous flow. *Phys. Rev. E* **82**, 046315. doi.org/10.1103/PhysRevE.82.046315.
11. Géraud B, Jones SA, Cantat I, Dollet B, Méheust Y. 2016 The flow of a foam in a two-dimensional porous medium. *Water Resour. Res.* **52**, 773–790. doi.org/10.1002/2015WR017936.
12. Bertin HJ, Apaydin OG, Castanier LM, Kovscek AR. 1999 Foam flow in heterogeneous porous media: Effect of cross flow. *SPE J.* **4**, 75–82. doi.org/10.2118/56009-PA.
13. Kovscek AR, Bertin HJ. 2003a Foam mobility in heterogeneous porous media. I. Scaling concepts. *Transport in Porous Media* **52**, 17–35. doi.org/10.1023/A:1022312225868.
14. Kovscek AR, Bertin HJ. 2003b Foam mobility in heterogeneous porous media. II. Experimental observations. *Transport in Porous Media* **52**, 37–49. doi.org/10.1023/A:1022368228594.
15. Khatib ZI, Hirasaki GJ, Falls AH. 1988 Effects of capillary pressure on coalescence and phase mobilities in foams flowing through porous media. *SPE Reservoir Engineering* **3**, 919–926. doi.org/10.2118/15442-PA.
16. Falls AH, Hirasaki GJ, Patzek TW, Gauglitz DA, Miller DD, Ratulowski T. 1988 Development of a mechanistic foam simulator: The population balance and generation by snap-off. *SPE Reservoir Engineering* **3**, 884–892. doi.org/10.2118/14961-PA.
17. Kovscek AR, Patzek TW, Radke CJ. 1994 Mechanistic prediction of foam displacement in multidimensions: A population balance approach. In *SPE/DOE Improved Oil Recovery Symposium, Tulsa, OK, 17th–20th April*. doi.org/10.2118/27789-MS.
18. Kovscek AR, Patzek TW, Radke CJ. 1995 A mechanistic population balance model for transient and steady-State foam flow in Boise sandstone. *Chem. Engng Sci.* **50**, 3783–3799. doi.org/10.1016/0009-2509(95)00199-F.
19. Kovscek AR, Patzek TW, Radke CJ. 1997 Mechanistic foam flow simulation in heterogeneous and multidimensional porous media. *SPE J.* **2**, 511–526. doi.org/10.2118/39102-PA.
20. Cheng L, Reme AB, Shan D, Coombe DA, Rossen WR. 2000 Simulating foam processes at high and low foam qualities. In *SPE/DOE Improved Oil Recovery Symposium, Tulsa, OK, 3rd–5th April*. doi.org/10.2118/59287-MS.
21. Kam SI. 2008 Improved mechanistic foam simulation with foam catastrophe theory. *Colloids and Surf. A, Physicochem. and Engg Aspects* **318**, 62–77. doi.org/10.1016/j.colsurfa.2007.12.017.
22. Rossen WR. 2013 Numerical challenges in foam simulation: A review. In *SPE Annual Technical Conference and Exhibition, New Orleans, LA, 30th September–2nd October*. doi.org/10.2118/166232-MS.
23. Ma K, Lopez-Salinas JL, Puerto MC, Miller CA, Biswal SL, Hirasaki GJ. 2013 Estimation of

parameters for the simulation of foam flow through porous media. Part 1: The dry-out effect. *Energy & Fuels* **27**, 2363–2375. doi.org/10.1021/ef302036s.
24. Ma K, Ren G, Mateen K, Morel D, Cordelier P. 2015 Modeling techniques for foam flow in porous media. *SPE J.* **20**, 453–470. doi.org/10.2118/169104-PA.
25. Farajzadeh R, Lotfollahi M, Eftekhari AA, Rossen WR, Hirasaki GJ. 2015 Effect of permeability on implicit-texture foam model parameters and the limiting capillary pressure. *Energy & Fuels* **29**, 3011–3018. doi.org/10.1021/acs.energyfuels.5b00248.
26. Zeng Y, Muthuswamy A, Ma K, Wang L, Farajzadeh R, Puerto M, Vincent-Bonnieu S, Eftekhari AA, Wang Y, Da C, Joyce JC, Biswal SL, Hirasaki GJ. 2016 Insights on foam transport from a texture-implicit local-equilibrium model with an improved parameter estimation algorithm. *Ind. Eng. Chem. Res.* **55**, 7819–7829. doi.org/10.1021/acs.iecr.6b01424.
27. Jiménez AI, Radke CJ. 1989 Dynamic Stability of Foam Lamellae Flowing Through a Periodically Constricted Pore. In Borchardt JK, Yen TF, editors, *Oil-Field Chemistry: Enhanced Recovery and Production Stimulation* number 396 in ACS Symposium Series pp. 460–479. Washington: American Chemical Society.
28. Rossen WR. 1990a Minimum pressure gradient for foam flow in porous media: Effect of interactions with stationary lamellae. *J. Colloid and Interf. Sci.* **139**, 457–468. doi.org/10.1016/0021-9797(90)90118-8.
29. Rossen WR. 1990b Theory of mobilization pressure gradient of flowing foams in porous media: I. Incompressible foam. *J. Colloid and Interf. Sci.* **136**, 1–16. doi.org/10.1016/0021-9797(90)90074-X.
30. Rossen WR. 1990c Theory of mobilization pressure gradient of flowing foams in porous media: III. Asymmetric lamella shapes. *J. Colloid and Interf. Sci.* **136**, 38–53. doi.org/10.1016/0021-9797(90)90076-Z.
31. Cox SJ, Neethling S, Rossen WR, Schleifenbaum W, Schmidt-Wellenburg P, Cilliers JJ. 2004 A theory of the effective yield stress of foam in porous media: The motion of a soap film traversing a three-dimensional pore. *Colloids and Surf. A, Physicochem. and Engg Aspects* **245**, 143–151. doi.org/10.1016/j.colsurfa.2004.07.004.
32. Ferguson DJ, Cox SJ. 2013 The motion of a foam lamella traversing an idealised bi-conical pore with a rounded central region. *Colloids and Surf. A, Physicochem. and Engg Aspects* **438**, 56–62. doi.org/10.1016/j.colsurfa.2013.02.015.
33. Nonnekes LE, Cox SJ, Rossen WR. 2015 Effect of gas diffusion on mobility of foam for enhanced oil recovery. *Transp. Porous Media* **106**, 669–689. doi.org/10.1007/s11242-014-0419-z.
34. Shi JX, Rossen WR. 1998 Improved surfactant-alternating-gas foam process to control gravity override. In *Improved Oil Recovery Symposium, Tulsa, OK, 19th–22nd April*. doi.org/10.2118/39653-MS.
35. Shi JX. 1996 *Simulation and Experimental Studies of Foam for Enhanced Oil Recovery*. PhD thesis University of Texas at Austin.
36. Rossen WR, van Duijn CJ, Nguyen QP, Shen C, Vikingstad AK. 2010 Injection strategies to overcome gravity segregation in simultaneous gas and water injection into homogeneous reservoirs. *SPE J.* **15**, 76–90. doi.org/10.2118/99794-PA.
37. de Velde Harsenhorst RM, Dharma AS, Andrianov A, Rossen WR. 2014 Extension and verification of a simple model for vertical sweep in foam SAG displacements. *SPE Reservoir Evaluation & Engg* **17**, 373–383. doi.org/10.2118/164891-PA.
38. Boeije CS, Rossen WR. 2014 Gas injection rate needed for SAG foam processes to overcome gravity override. *SPE J.* **20**, 49–59. doi.org/10.2118/166244-PA.
39. Zeng Y, Farajzadeh R, Biswal SL, Hirasaki GJ. 2019 A 2-D simulation study on CO_2 soluble surfactant for foam enhanced oil recovery. *J. Ind. Eng. Chem.* **72**, 133–143. doi.org/10.1016/j.jiec.2018.12.013.
40. Shan D, Rossen WR. 2004 Optimal injection strategies for foam IOR. *SPE J.* **9**, 132–150. doi.org/10.2118/88811-PA.
41. Grassia P, Mas-Hernández E, Shokri N, Cox SJ, Mishuris G, Rossen WR. 2014 Analysis of a model for foam improved oil recovery. *J. Fluid Mech.* **751**, 346–405. doi.org/10.1017/jfm.2014.287.
42. Grassia P, Lue L, Torres-Ulloa C, Berres S. 2017 Foam front advance during improved oil recovery: Similarity solutions at early times near the top of the front. *J. Fluid Mech.* **828**, 527–572. doi.org/10.1017/jfm.2017.541.
43. Zhou ZH, Rossen WR. 1995 Applying fractional-flow theory to foam processes at the

'limiting capillary pressure'. *SPE Advanced Technology Series* **3**, 154–162. doi.org/10.2118/24180-PA.
44. Rossen WR, Zeilinger SC, Shi JX, Lim MT. 1999 Simplified mechanistic simulation of foam processes in porous media. *SPE J.* **4**, 279–287. doi.org/10.2118/57678-PA.
45. Dholkawala ZF, Sarma HK, Kam SI. 2007 Application of fractional flow theory to foams in porous media. *J. Petrol. Sci. Eng.* **57**, 152–165. doi.org/10.1016/j.petrol.2005.10.012.
46. Ashoori E, van der Heijden TLM, Rossen WR. 2010 Fractional-flow theory of foam displacements with oil. *SPE J.* **15**, 260–273. doi.org/10.2118/121579-PA.
47. Afsharpoor A, Lee GS, Kam SI. 2010 Mechanistic simulation of continuous gas injection period during surfactant-alternating-gas (SAG) processes using foam catastrophe theory. *Chem. Engng Sci.* **65**, 3615–3631. doi.org/10.1016/j.ces.2010.03.001.
48. Mas-Hernández E, Grassia P, Shokri N. 2016 Modelling foam improved oil recovery within a heterogeneous reservoir. *Colloids and Surf. A, Physicochem. and Engg Aspects* **510**, 43–52. doi.org/10.1016/j.colsurfa.2016.07.064.
49. Grassia P, Torres-Ulloa C, Berres S, Mas-Hernández E, Shokri N. 2016 Foam front propagation in anisotropic oil reservoirs. *Eur. Phys. J. E* **39**, 42. doi.org/10.1140/epje/i2016-16042-5.
50. Grassia P. 2017 Foam front displacement in improved oil recovery in systems with anisotropic permeability. *Colloids and Surf. A, Physicochem. and Engg Aspects* **534**, 44–51. doi.org/10.1016/j.colsurfa.2017.03.059.
51. Mas-Hernández E, Grassia P, Shokri N. 2015a Foam improved oil recovery: Foam front displacement in the presence of slumping. *Colloids and Surf. A, Physicochem. and Engg Aspects* **473**, 123–132. doi.org/10.1016/j.colsurfa.2014.12.023.
52. Mas-Hernández E, Grassia P, Shokri N. 2015b Foam improved oil recovery: Modelling the effect of an increase in injection pressure. *Eur. Phys. J. E* **38**, 67. doi.org/10.1140/epje/i2015-15067-6.
53. Lotfollahi M, Farajzadeh R, Delshad M, Varavei A, Rossen WR. 2016 Comparison of implicit-texture and population-balance foam models. *J. Nat. Gas Sci. Eng.* **31**, 184–197. doi.org/10.1016/j.jngse.2016.03.018.
54. Brooks RH, Corey AT. 1964 Hydraulic properties of porous media. Technical report Hydrology Papers, Colorado State University.
55. Corey AT. 1954 The interrelation between gas and oil relative permeabilities. *Prod. Monthly* **19**, 38–41.
56. Persoff P, Radke CJ, Pruess K, Benson SM, Witherspoon PA. 1991 A laboratory investigation of foam flow in sandstone at elevated pressure. *SPE Reservoir Engg* **6**, 365–372. doi.org/10.2118/18781-PA.
57. Rossen WR, Boeije CS. 2015 Fitting foam-simulation-model parameters to data: II. Surfactant-alternating-gas foam applications. *SPE Reservoir Evaluation & Engg* **18**, 273–283. doi.org/10.2118/165282-PA.
58. Gauglitz PA, Friedmann F, Kam SI, Rossen WR. 2002 Foam generation in homogeneous porous media. *Chem. Engng Sci.* **57**, 4037–4052. doi.org/10.1016/S0009-2509(02)00340-8.
59. Buckley SE, Leverett MC. 1942 Mechanism of fluid displacements in sands. *Trans. AIME* **146**, 107–116. doi.org/10.2118/942107-G.
60. Courant R, Friedrichs KO. 1948 *Supersonic Flow and Shock Waves*. New York: Interscience.
61. Zhou ZH, Rossen WR. 1994 Applying fractional-flow theory to foams for diversion in matrix acidization. *SPE Prod. Facil.* **9**, 29–35. doi.org/10.2118/24660-PA.
62. Gong J, Flores Martinez W, Vincent-Bonnieu S, Bahrim RZK, Mamat CANBC, Tewari RD, Amir MIM, Farajzadeh R, Rossen W. 2020 Effect of superficial velocity on liquid injectivity in SAG foam EOR. Part 2: Modelling. *Fuel* **279**, 118302. doi.org/10.1016/j.fuel.2020.118302.

PROCEEDINGS A

rspa.royalsocietypublishing.org

Research

Article submitted to journal

Subject Areas:
Mathematical modelling, Applied mathematics

Keywords:
Pressure-driven growth, Fractional-flow theory, Foam improved oil recovery, Flow in porous media, Flow reversal, Method of characteristics

Author for correspondence:
P. Grassia
e-mail: paul.grassia@strath.ac.uk

THE ROYAL SOCIETY PUBLISHING

Supplementary Material: Modelling Foam Improved Oil Recovery: Towards a Formulation of Pressure-Driven Growth with Flow Reversal

M. Eneotu[1], P. Grassia[1]

[1] Department of Chemical and Process Engineering, University of Strathclyde, James Weir Building, 75 Montrose Street, Glasgow G1 1XJ, UK

This supplementary section examines how predictions of fractional flow theory incorporating reverse flow are sensitive to model parameters when parameters are varied about the base case values specified in the main text. Increasing the maximum mobility reduction factor associated with foamed gas causes liquid saturations adjacent to a propagating foam front to shift to slightly lower values. Whilst the total relative mobility of fluid tends to be lower at the front than anywhere else in the domain, the mobility at the front itself is relatively insensitive to changes in the maximum mobility reduction factor, since fluid mobility tends to dominated by liquid rather than by gas. On the other hand, changing the relative permeability formula for liquid (along with that for unfoamed gas) has more significant impact on lowering total relative mobility at the front.

A. Sensitivity to model parameters

The results presented in the main text focussed on one very specific parameter set, namely relative permeabilities for liquid and for gas (in the absence of foam) that follow equation (3.1) and with a mobility reduction factor due to foam that follows equation (3.2). In the present section we examine how much our predictions would change if parameters used in the model are varied about base case values specified in Table 1. Specifically in section (a) we vary the maximum amount R_f that foam reduces gas relative mobility and in section (b) we look at varying power law exponents within the relative permeability formulae themselves.

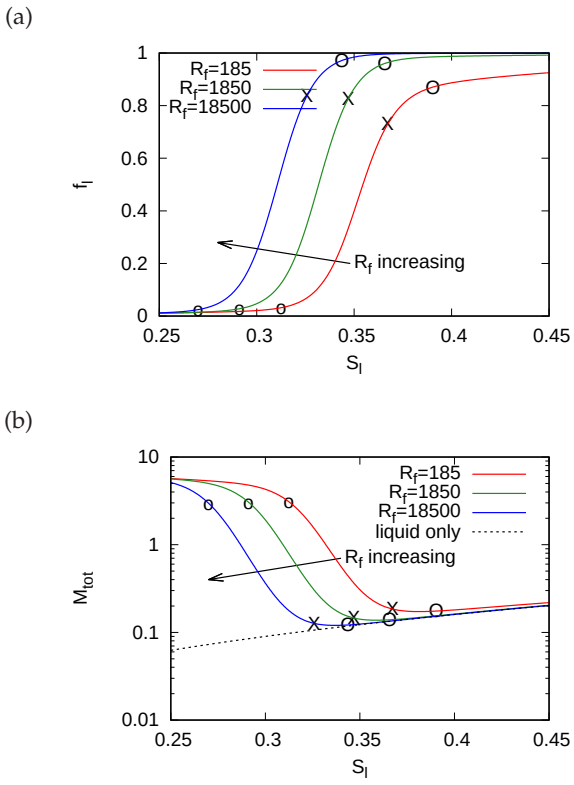

Figure A 1. Effect of increasing foam mobility reduction factor R_f on (a) fractional flow curve and (b) mobility. For each curve the symbols (○, X and ◯) indicate values $S_l = S_{l,\mathrm{fwd}}$, $S_l = S_{l,\mathrm{rev},0}$ and $S_l = S_{l,\mathrm{rev},\infty}$ respectively.

(a) Varying maximum mobility reduction factor

In Figure A 1 we see the effect increasing the parameter R_f within equation (3.2) which represents the maximum mobility reduction due to foam. Specifically we considered $R_f = 185$ (our base case), $R_f = 1850$ and $R_f = 18500$. Other parameters are fixed as per Table 1 in the main text. As Figure A 1(a) shows, with increasing R_f, the transition in fractional flow f_l from values $f_l \ll 1$ to values $f_l \approx 1$ tends to happen at smaller S_l values. As such the values of $S_{l,\mathrm{fwd}}$, $S_{l,\mathrm{rev},0}$ and $S_{l,\mathrm{rev},\infty}$ also shift to smaller values as Figure A 1(a) and (in the main text) Table 2 show.

The values of total relative mobility in forward flow $M_{\mathrm{tot,fwd}}$ (see Figure A 1(b)) are not greatly affected. In particular $M_{\mathrm{tot,fwd}}$ remains significantly above unity, which means that strictly speaking in forward flow mode it is not possible to ignore the pressure drop associated with pure liquid filled regions (for which mobility $M_{\mathrm{tot}} \equiv 1$ by definition) relative to pressure drop across the gas-liquid mixture at the front itself: this has already been discussed in section 4(f). Mobilities associated with reverse flow e.g. $M_{\mathrm{tot,rev},0}$ and/or $M_{\mathrm{tot,rev},\infty}$ are reduced when R_f increases (see Figure A 1(b) and Table 2), but they certainly do not reduce by orders of magnitude. In fact the total flow under these reverse flow conditions is dominated by the liquid, so the decrease in M_{tot} with increasing R_f, really just reflects relative permeability of liquid $k_{r,l}$ (see equation (3.1)) decreasing slightly as $S_{l,\mathrm{rev},0}$ and $S_{l,\mathrm{rev},\infty}$ decrease.

	$R_f = 185$	$R_f = 1850$	$R_f = 18500$
$S_{l,\mathrm{fwd}}$	0.3258	0.3061	0.2865
$M_{\mathrm{tot,fwd}}$	0.6553	0.5745	0.4861
$S_{l,\mathrm{infl}}$	0.3614	0.3434	0.3241
$M_{\mathrm{tot,infl}}$	0.0467	0.0291	0.0221
$S_{l,\mathrm{rev},0}$	0.3767	0.3575	0.3380
$M_{\mathrm{tot,rev},0}$	0.0324	0.0204	0.0156
$S_{l,\mathrm{min\ mob}}$	0.3852	0.3631	0.3428
$M_{\mathrm{tot,min}}$	0.0314	0.0200	0.0154
$S_{l,\mathrm{rev},\infty}$	0.4315	0.3778	0.3558
$M_{\mathrm{tot,rev},\infty}$	0.0403	0.0215	0.0165

Table A 1. Key liquid saturations ($S_{l,\mathrm{fwd}}$, $S_{l,\mathrm{infl}}$, $S_{l,\mathrm{rev},0}$, $S_{l,\mathrm{min\ mob}}$, $S_{l,\mathrm{rev},\infty}$) and associated total mobilities ($M_{\mathrm{tot,fwd}}$, $M_{\mathrm{tot,infl}}$, $M_{\mathrm{tot,rev},0}$, $M_{\mathrm{tot,min}}$, $M_{\mathrm{tot,rev},\infty}$) for different values of the foam mobility reduction factor R_f, and using an alternative model for relative permeabilities $k_{r,l}$ and $k^0_{r,g}$, equation (A.1) instead of equation (3.1). Mobilities reported here are significantly lower than those reported in Table 2.

(b) Varying relative permeability formulae

Another way that we can alter the model is by changing the relative permeability model used for liquid and/or for gas (in the absence of foam). Instead of (3.1), we now propose

$$k_{r,l} = S_l^4, \quad k^0_{r,g} = (1 - S_l)^4 \tag{A.1}$$

Literature supports formulae like these [1–3] in which, compared to equation (3.1), $k_{r,l}$ and $k^0_{r,g}$ grow more slowly as S_l respectively increases from zero or decreases from unity.

If foam is present, the main difference from employing equation (A.1) instead of equation (3.1) is expected to arise from having changed the formula for $k_{r,l}$ rather than from changing the $k^0_{r,g}$ formula. This is because as far as gas is concerned, the most important effect upon mobility is $k_{r,g}$ falling via equation (3.2) to values far below $k^0_{r,g}$, not the modification in the value of $k^0_{r,g}$ itself.

Data are shown in Figure A 2 and Table A 1 at various R_f values, namely $R_f = 185$, 1850 and 18500, again with other parameters fixed as per Table 1. Values of $S_{l,\mathrm{fwd}}$ and $S_{l,\mathrm{rev},0}$ change by relatively modest amounts compared to the former data set for which relative permeabilities were given by equation (3.1). In the case $R_f = 185$, comparing Figure 3(a) with Figure A 1(a), we see $S_{l,\mathrm{rev},\infty}$ changing by a slightly more significant amount (from a value 0.3904 in Table 2 to 0.4315 in Table A 1). This is associated (see Figure A 2(a)) with a surprisingly slow increase in f_l between $S_l = S_{l,\mathrm{rev},0}$ and $S_l = S_{l,\mathrm{rev},\infty}$, which comes about as follows. For $R_f = 185$, even though at $S_l = S_{l,\mathrm{rev},0}$, the value of $\lambda_{r,g} = k_{r,g}/\mu_g$ has fallen to a level much smaller than $\lambda^0_{r,g} = k^0_{r,g}/\mu_g$, it is also the case that owing to equation (A.1), the value of $\lambda_{r,l} = k_{r,l}/\mu_l$ is now itself an order of magnitude smaller than $\lambda^0_{r,g}$. Thus even though $\lambda_{r,g}$ has already fallen dramatically from $\lambda^0_{r,g}$ to around $\lambda^0_{r,g}/R_f$, for the case when $R_f = 185$, this is only an order of magnitude less than $\lambda_{r,l}$. Further increases in $f_l \equiv \lambda_{r,l}/(\lambda_{r,l} + \lambda_{r,g})$ with increasing S_l rely on $\lambda_{r,l}$ increasing: such increases are gradual.

Total relative mobilities M_{tot} are now smaller than unity at $S_l = S_{l,\mathrm{fwd}}$ (see Figure A 2(b) and Table A 1, a contrast with Figure 3(c) and Table 2). Even in forward flow mode then, foam at the front is now less mobile than pure liquid, in line with what the pressure-driven growth model hypothesises. However for reverse flow e.g. at $S_l = S_{l,\mathrm{rev},0}$ or at $S_l = S_{l,\mathrm{rev},\infty}$, the total mobility M_{tot} is much lower still (see Figure A 2(c) and Table A 1).

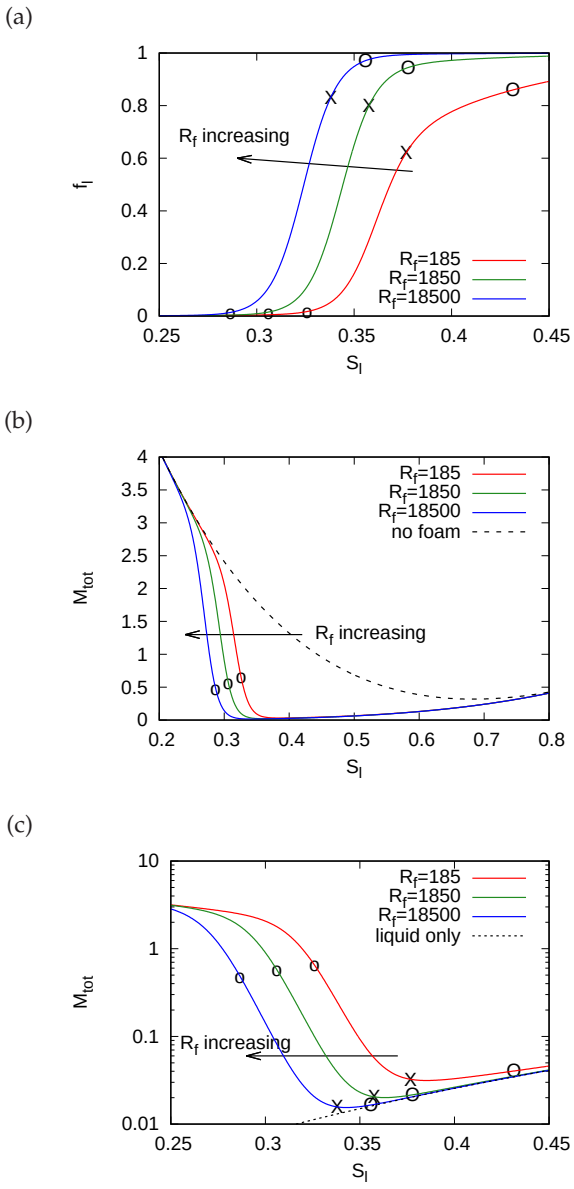

Figure A 2. Effect of looking at different a priori relative permeability functions (a) f_l vs S_l. (b) $M_{\rm tot}$ vs S_l. (c) $M_{\rm tot}$ vs S_l on log scale. Symbols on each curve (○, X and ◯) indicate $S_l = S_{l,\rm fwd}$, $S_l = S_{l,\rm rev,0}$ and $S_l = S_{l,\rm rev,\infty}$.

References

1. Corey AT. 1954 The interrelation between gas and oil relative permeabilities. *Prod. Monthly* **19**, 38–41.
2. Brooks RH, Corey AT. 1964 Hydraulic properties of porous media. Technical report Hydrology Papers, Colorado State University.
3. Rossen WR, Boeije CS. 2015 Fitting foam-simulation-model parameters to data: II. Surfactant-alternating-gas foam applications. *SPE Reservoir Evaluation & Engg* **18**, 273–283. doi.org/10.2118/165282-PA.

Chapter 6

Conclusions/Further Work

This chapter concludes this research and gives an insight into what could possibly be added to this work in the future.

6.1 Conclusions

To conclude, this work has succeeded in looking into an area of foam improved oil recovery not yet covered in literature, namely foam improved oil recovery during a flow reversal process. Having studied the evolution of the foam front (in particular the evolution of a shock) over time when there is a change of flow direction, the following specific conclusions have been drawn.

- The fractional flow theory and the method of characteristics (MOC) have been used to explain what happens after a change of flow direction during foam improved oil recovery (IOR). During this process, a shock is formed between foamed gas with a small amount of water (downstream of the shock) and water with a small amount of foamed gas (upstream of the shock).

- The major difference between a normal flow or flow in one direction during foam improved oil recovery and a reverse flow situation is that, on one hand in the former,

there is only one fan on one side of the shock or more correctly contact discontinuity (i.e. low liquid saturations on the upstream side of the forward propagating system). On the other hand, in the latter case, a complex structure appears with fans existing on either side of the shock (i.e. low liquid saturations and high liquid saturations on the downstream and upstream of the shock respectively).

- During flow reversal in foam IOR, characteristics that start off behind (i.e. upstream of) the shock will collide with the shock as they move downstream. Meanwhile the shock will collide with characteristics that start off ahead of (i.e downstream of) it.

- As the reverse flow proceeds, the water or liquid saturation immediately behind the shock (i.e. immediately upstream) will increase while the water saturations ahead (i.e. downstream) of the shock will decrease.

- In foam IOR during flow reversal, depending on how quickly water saturation S_w (or more generally liquid saturation) increases upstream of the shock and how quickly S_w decreases of downstream of it, the shock velocity may either decrease or increase over time. Initially velocity decreases driven by a decrease in downstream S_w. Later on downstream S_w reaches connate or irreducible water saturation and falls no further. The shock velocity then rises driven by an increase in upstream S_w.

- The overall solution to a flow reversal problem during foam improved oil recovery depends on the interaction between the two characteristic fans upstream and downstream of the shock.

6.2 Further Work

This work has met the objective of giving insight into flow reversed fractional flow systems for foam in porous media. However there remain a number of open research questions that could be answered in the future.

For this work, one such research question that could be answered in future work is whether the pressure field would still be comparatively uniform in the gas bank for both forward and reversed direction or will the mobility at the front in either the forward flow or the reversed flow direction be too high for that to happen, meaning that pressure drops occur throughout the gas bank not just at the front?

It would also be of interest to include the presence of oil as a task for further work. This is because this study only considered either that oil, if present, only exists at the residual saturation (i.e. oil is not mobile at the residual oil saturation) or else oil was treated as being incorporated within a generic liquid phase along with aqueous surfactant. If oil is considered as a separate phase, there is the possibility that it could have an effect on the foam texture, which could ultimately have an effect on the mobility of the gas. Hence, the influence of oil on foam quality needs to be investigated. If oil is considered in the model as a separate (third) fluid phase, the relative permeability of the oil phase could be included in the model similar to the study of Tang et al. (2019) where a three-phase relative permeability function was used to study foam-oil interaction. Hence, such approach could be followed, only that in our case, flow reversal will additionally be taken into consideration. Be that as it may, it is important to remember that the presence of oil could also significantly affect the relative permeability of foamed gas, as oil tends to

break foam, so the mobility of the gas would not be reduced by as much as it would be in the absence of oil. Ultimately, this would be an interesting area to consider in further work, in the context of this research.

Also, a case of foam injection following surfactant preflush could also be considered. According to Rossen et al. (2011), albeit for a forward displacement process only, a foam injection process following surfactant preflush is possible instead of a surfactant-alternating-gas SAG process. After flow reversal, this would have significant impact on conditions downstream of the front/shock. It would be interesting to know what effect this could have on the reversed flow.

Furthermore, similar sensitivity analysis to parameters governing foam mobility as done in the published paper could be included in the future work. Sensitivities could be done with respect to some of the parameters appearing in the relative permeability functions. For instance, because of the relative permeability functions used (see equations (2.59)–(2.63) and figures 2.19 and 2.20) in this study, it can be observed that after the 'S_w' value at which gas mobility falls sharply; somewhere around 'S_w' = 0.37, the value of 'f_w' (see figures 2.21 and 3.1) only increases quite gradually as the relative permeability of water is still very low around that area (see figure 2.20), and 'f_w' can only more increase significantly with increasing 'S_w' as relative permeability of water increases. Other relative permeability formulae that we might consider need not exhibit that feature of such low water permeabilities in this part of the S_w domain, so need not have quite such gradual f_w increases in this region.

Another effect of the relative permeability function used in this study can be seen in figure 4.5 where there was a fairly abrupt change in downstream 'S_w' versus 't_D' near the minimum i.e. irreducible 'S_w'. This comes about because there is a wide domain of

S_w values above the irreducible saturation at which $f'(S_w)$ is tiny, meaning that many characteristic lines with different S_w values cluster close to $x_D = 0$ and the shock crosses all these characteristic lines in a short time interval. This also manifests in figure 4.6 in which as well as a jump in S_w at the shock, there is also (at $x_D = 0$ which is still some distance downstream of the shock in this case) a large spatial gradient of S_w vs x_D, for S_w values immediately above the irreducible saturation. A different relative permeability function could possibly yield a different result. As such, it will be interested to consider this in future work.

Finally, it would be interesting to carry out some experimental work to validate the mathematical modelling used in this study. In addition, in this study it is noticed that emphases have not been placed on determination of recovery or displacement efficiency (that is the fraction of the original oil or reservoir fluids in place that have been recovered at any instant in time) during a foam flow reversal process. Rather the emphasis is on how the shock front (simply put, a jump in saturation at the foam front) travels in the case of a flow reversal process. Of course, this itself could give an indication of the sweep efficiency and by extension the effectiveness of the foam displacement process, but this study did not quantify the measure with which this could happen. In other words, calculations were not done to determine the actual recovery efficiency not even assuming a forward flow mode. Welge (1952) has a method which uses the saturation profile and the fractional flow curve to determine the recovery efficiency. Thus, as a task for further work, it would be interesting to attempt to use this method; albeit in a modified form to determine recovery efficiency as it relates to this research incorporating reverse flow.

Nomenclature

A = cross-sectional area

C_s = surfactant concentration in water phase

C_s^o = threshold surfactant concentration for foam

f = foam quality

f_w = fractional flow of water or water-cut

f_{wf} = fractional flow of water in the foam or flood bank

i_w = rate of water injection

k_o = oil effective permeability

k_w = water effective permeability

k_g = gas effective permeability

k_{ro} = oil relative permeability

k_{rw} = water relative permeability

k_{rw}^o = water relative permeability at the residual gas saturation

k_{rg} = gas relative permeability

k_{rg}^o = gas relative permeability at the connate water saturation

k_{rg^o} = gas relative permeability without foam

n = parameter in Fisher model

n_w and n_g = exponents on Corey's relative permeability curves

P_c^* = limiting capillary pressure

P_o = oil pressure

P_w = water pressure

q_g = flow rate of gas

q_o = flow rate of oil

q_t = total fluid flow rate

q_w = flow rate of water

R = parameter in the fixed- P_c^* model for gas mobility with foam

S_{or} = residual oil saturation

S_w = water saturation

S_{wI} = initial water saturation

S_{wr} = connate water saturation

S_{wi} = irreducible water saturation

S_w^* = limiting water saturation (i.e. water saturation at P_c^*)

S_{wf} = water saturation at the front, flood bank or in the foam

S_{gr} = residual gas saturation in the gas-water system

t = time

t_D = dimensionless time in fractional flow model

V_w = volume of liquid in foam

V_g = volume of gas in foam

x = distance or position

x_D = dimensionless distance in fractional flow model

$(x)_{sw}$ = distance from the injection for a given saturation

Greek Symbols:

α = dip angle (positive for updip flow and negative for downdip flow)

ϵ = parameter in the fixed-P_c* model (or more precisely in the progressive collapse generalisation thereof) for gas mobility with foam

λ_g = gas mobility

λ_{rw} = aqueous phase relative mobility

λ_{rg} = gaseous phase relative mobility

$\lambda_{rw}*$ = parameter in Fisher model for aqueous phase relative mobility

$\lambda_{rg}*$ = parameter in Fisher model for gaseous phase relative mobility

ϕ = porosity of porous media

ρ_o = oil density

ρ_w = water density

μ_o = oil viscosity

μ_w = water viscosity

μ_g = gas viscosity

Bibliography

Akbari, S., Nour, A. H., Yunus, R. M., Farhan, A. H., 2018. Biosurfactants as promising multifunctional agent: A mini review. *International Journal of Innovative Research and Scientific Studies* **1**(01), 1–7.

Al-Jarba, M., Al-Anazi, B. D., 2009. A comparison study of the of the CO_2-oil physical properties-literature correlations accuracy using visual basic modeling technique. *Nafta* **60**(05), 287–291.

Ali, J., Burley, R. W., Nutt, C. W., 1985. Foam enhanced oil recovery from sand packs. *Chemical Engineering Research and Design* **63**(02), 101–111.

Almajid, M. M., 2019. Experimental and numerical evaluation of foam physics in porous media across multiple scales. Ph.D. thesis, Stanford University, Stanford, California.

Almajid, M. M., Kovscek, A., 2016. Pore-level mechanics of foam generation and coalescence in the presence of oil. *Advances in colloid and interface science* **233**, 65–82.

Almajid, M. M., Kovscek, A., 2020. Pore network investigation of trapped gas and foam generation mechanisms. *Transport in Porous Media* **131**(01), 289–313.

Almajid, M. M., Nazari, N., Kovscek, A., 2019. Modeling steady–state foam flow: Hysteresis and backward front movement. *Energy & Fuels* **33**(11), 11353–11363.

Alvarez, J., Rivas, H., Rossen, W. R., 2001. Unified model for steady-state foam behavior at high and low foam qualities. *SPE Journal* **6**(03), 325–333.

AlYousef, Z., Almobarky, M., Schechter, D., 2017. Enhancing the stability of foam by the use of nanoparticles. *Energy & Fuels* **31**(10), 10620–10627.

Andrianov, A., Farajzadeh, R., Mahmoodi, N. M., Talanana, M., Zitha, P. L., 2012. Immiscible foam for enhancing oil recovery: bulk and porous media experiments. *Industrial & Engineering Chemistry Research* **51**(05).

Ashoori, E., Rossen, W. R., 2010. Can formation relative permeabilities rule out a foam EOR process. In: *ECMOR XII-12th European Conference on the Mathematics of Oil Recovery, Oxford, UK, 06–09 September*, cp–163.

Ashoori, E., van der Heijden, T. L. M., Rossen, W. R., 2009. Fractional-flow theory of CO_2 foam displacements with surfactant dissolved in the CO_2. In: *15th European Symposium on Improved Oil Recovery, Paris, France, 27–29 April*, cp–124.

Bedrikovetsky, P., 2013. *Mathematical theory of oil and gas recovery: with applications to ex-USSR oil and gas fields*. Vol. **4**. Springer Science & Business Media.

Belhaij, A., AlQuraishi, A., Al-Mahdy, O., 2014. Foamability and foam stability of several surfactants solutions: the role of screening and flooding (SPE paper 172185). In: *SPE Saudi Arabia section technical symposium and exhibition, Al-Khobar, Saudi Arabia, 21–24 April*.

Bernard, G. G., Holm, L. W., 2001. Effect of foam on permeability of porous media to gas. *SPE Journal* **4**(03), 267–274.

Bernard, G. G., Holm, L. W., Jacobs, W. L., 1965. Effect of foam on trapped gas saturation and on permeability of porous media to water. *SPE Journal* **5**(04), 295–300.

Bertin, H. J., Apaydin, O. G., Castanier, L. M., Kovscek, A. R., 1999. Foam flow in heterogeneous porous media: effect of cross flow. *SPE Journal* **4**(02), 75–82.

Bikerman, J. J., 1953. *Foams: Theory and Industrial Applications*. Reinhold Publishing Corporation, New York, 1–25.

Boeije, C. S., Rossen, W. R., 2014. Gas-injection rate needed for SAG foam processes to overcome gravity override. *SPE Journal* **20**(01), 49–59.

Brooks, R. H., Corey, A. T., 1964. Hydraulic properties of porous media and their relation to drainage design. *Transactions of the ASAE* **7**(01), 26–0028.

Buckley, S. E., Leverett, M., 1942. Mechanism of fluid displacement in sands. *Trans. AIME* **146**, 107–116.

Cantat, I., Cohen-Addad, S., Elias, F., Graner, F., Höhler, R., Pitois, O., Rouyer, F., Saint-Jalmes, A., 2013. *Foams: structure and dynamics*. Oxford University Press, 75–127.

Castillo, R. O. S., Ter Haar, S. F., Ponners, C. G., Bos, M., Rossen, W. R., 2020. Fractional-flow theory for non-newtonian surfactant-alternating-gas foam processes. *Transport in Porous Media* **131**(02), 399–426.

Chambers, K. T., Radke, C. J., 1990. Capillary phenomena in foam flow through porous media. *Interfacial Phenomena in Oil Recovery*.

Chang, S., Grigg, R. B., 1996. Foam displacement modeling in CO_2 flooding processes (SPE paper/DOE 35401). In: *SPE/DOE 10th Symposium on Improved Oil Recovery, Tulsa, OK, 21–24 April*, 575–583.

Chang, S., Owusu, L. A., French, S. B., Kovarik, F. S., 1990. The effect of microscopic heterogeneity on CO_2 foam mobility: Part 2- Mechanistic foam simulation (SPE paper/DOE 20191). In: *SPE/DOE Enhanced Oil Recovery Symposium, Tulsa, OK, 22–25 April*, 154–162.

Chang, Y., 1990. Development and application of an equation of state compositional simulator. Ph.D. thesis, The University of Texas at Austin, Austin, Texas.

Chen, H., Li, Z., Wang, F., Li, A., Wanambwa, S., Lu, T., 2020. Experimental study on the enhanced oil recovery by in situ foam formulation. *Energy Science & Engineering* **8**(04), 1092–1103.

Clark, N. J., 1969. Elements of petroleum reservoirs. Society of Petroleum Engineers of AIME.

Computer Modeling Group, 2006. STARS User's Guide. CMG Ltd. Calgary, Alberta, Canada.

Corey, A. T., 1954. The interrelation between gas and oil relative permeabilitiese. *Producers monthly* **19**(01), 38–41.

Corey, A. T., Rathjens, C. H., Henderson, J. H., Wyllie, M. R. J., 1956. Three-phase relative permeability. *Journal of Petroleum Technology* **8**, 63–65.

Courant, R., Friedrichs, K. O., 1948. Supersonic flow and shock waves. In: *Pure and Applied Mathematics: a Series of Texts and Monographs* (ed. Bohr, H., Courant, R. and Stoker, J. J). Interscience Publisher.

Courant, R., Friedrichs, K. O., 1999a. Supersonic flow and shock waves. Vol. **21**. Springer Science & Business Media.

Courant, R., Friedrichs, K. O., 1999b. *Supersonic flow and shock waves*. Vol. 21. Springer Science & Business Media.

Dake, L. P., 1978. *Fundamentals of reservoir engineering, volume 8 of Developments in petroleum science*. Elsevier Scientific Publishing Company.

Debbabi, Y., Jackson, M. D., Hampson, G. J., Fitch, P. J., Salinas, P., 2017. Viscous crossflow in layered porous media. *Transport in Porous Media* **117**, 281–309.

Delshad, M., Pope, G. A., Sepehrnoori, K., 2000. UTCHEM technical documentation version 9.0. *Center For Petroleum and Geosystems Engineering, The University of Texas at Austin*.

DeNevers, N., Silcox, G. D., 1991. *Fluid mechanics for chemical engineers*. McGraw-Hill, 163–166.

Dharma, A. S., 2013. Simulation studies of foam for enhanced oil recovery. Ph.D. thesis, Delft University of Technology, Delft, Netherlands.

Dholkawala, Z. F., Sarma, H. K., Kam, S. I., 2007. Application of fractional flow theory to foams in porous media. *Journal of Petroleum Science and Engineering* **57**(01–02), 152–165.

Ding, L., Cui, L., Jouenne, S., Gharbi, O., Pal, M., Bertin, H., Rahman, M. A., Romero, C., Guérillot, D., 2020. Estimation of local equilibrium model parameters for simulation of the laboratory foam-enhanced oil recovery process using a commercial reservoir simulator. *ACS Omega* **5**(36), 23437–23449.

Durand, M., Langevin, D., 2002. Physicochemical approach to the theory of foam drainage. *The European Physical Journal E* **7**(01), 35–44.

Eftekhari, A. A., Farajzadeh, R., 2017. Effect of foam on liquid phase mobility in porous media. *Scientific reports* **7**(01), 1–8.

Eneotu, M., Grassia, P., 2020. Modelling foam improved oil recovery: towards a formulation of pressure-driven growth with flow reversal. *Proceedings of the Royal Society A* **476**(2244), 20200573.

Ettinger, R. A., Radke, C. J., 1992. Influence of texture on steady foam flow in Berea Sandstone. *SPE Reser. Engng* **7**(01), 83–90.

Fakher, S., Elgahawy, Y., Abdelaal, H., 2020. Oil swelling measurement techniques: Conventional methods and novel pressure-based method. In: *Unconventional Resources Technology Conference (URTeC), Austin, TX, 20–22 July.*

Falls, A. H., Hirasaki, G. J., Patzek, T. E. A., Gauglitz, D. D., Ratulowski, J., 1988. Development of a mechanistic foam simulator: the population balance and generation by snap-off. *SPE Reser. Engng* **3**, 884–892.

Falls, A. H., Musters, J. J., Ratulowski, J., 1989. The apparent viscosity of foams in homogeneous bead packs. *SPE Reser. Engng* **4**, 155–164.

Fanchi, J. R., 2002. *Shared Earth Modeling: Methodologies for Integrated Reservoir Simulations*. Gulf Professional Publishing, 272–281.

Farajzadeh, R., 2009. Enhanced transport phenomena in CO_2 sequestration and CO_2 EOR. Ph.D. thesis, Delft University of Technology, Delft, Netherlands.

Farajzadeh, R., Andrianov, A., Krastev, R., Hirasaki, G. J., Rossen, W. R., 2012a. Foam–oil interaction in porous media: implications for foam assisted enhanced oil recovery. *Advances in Colloid and Interface Science* 183, 1–13.

Farajzadeh, R., Eftekhari, A. A., Hajibeygi, H., Kahrobaei, S., Van der Meer, J. M., Vincent-Bonnieu, S., Rossen, W. R., 2016. Simulation of instabilities and fingering in surfactant alternating gas (SAG) foam enhanced oil recovery. *Journal of Natural Gas Science and Engineering* **34**, 1191–1204.

Farajzadeh, R., Lotfollahi, M., Eftekhari, A. A., Rossen, W. R., Hirasaki, G. J., 2015. Effect of permeability on implicit-texture foam model parameters and the limiting capillary pressure. *Energy & Fuels* **29**(05), 3011–3018.

Farajzadeh, R., Wassing, B. L., Lake, L. W., 2019. Insights into design of mobility control for chemical enhanced oil recovery. *Energy Reports* **5**, 570–578.

Farajzadeh, R., Wassing, B. M., Boerrigter, P. M., 2012b. Foam assisted gas–oil gravity drainage in naturally-fractured reservoirs. *Journal of Petroleum Science and Engineering* **94**, 112–122.

Farzaneh, S. A., Sohrabi, M., 2013. A review of the status of foam application in enhanced oil recoveryd (SPE paper 164917). In: *EAGE Annual Conference & Exhibition incorporating SPE Europec, London, United Kingdom, 10–13 June*.

Fisher, A. W., Foulser, R. W. S., Goodyear, S. G., 1990. Mathematical modelling of foam flooding (SPE paper/DOE 20195). In: *SPE/DOE Enhanced Oil Recovery Symposium, Tulsa, OK, 22–25 April*, 154–162.

Friedmann, F., Chen, W. H., Gauglitz, P. A., 1991. Experimental and simulation study of high-temperature foam displacement in porous media. *SPE Reser. Engng* **5**, 37–45.

Friedmann, F., Jensen, J. A., 1986. Some parameters influencing the formation and prop-

agation of foams in porous media (SPE paper 15078). In: *SPE Regional Meeting, Oakland, CA, 2–4 April*, 441–449.

Gauglitz, P. A., Friedmann, F., Kam, S. I., Rossen, W. R., 2002. Foam generation in homogeneous porous media. *Chemical Engineering Science* **57**(19), 4037–4052.

Géraud, B., Méheust, Y., Cantat, I., Dollet, B., 2017. Lamella division in a foam flowing through a two-dimensional porous medium: A model fragmentation process. *Physical review letters* **118**(09), 098003.

Gillis, J. V., Radke, C. J., 1990. A dual-gas tracer technique for determining trapped gas saturation during steady foam flow in porous media (SPE paper-20519MS). In: *SPE Annual Technical Conference and Exhibition, New Orleans, Louisiana, 23–26 September*, 475–485.

Grassia, P., Mas-Hernandez, E., Shokri, N., Cox, S., Mishuris, G., Rossen, W., 2014. Analysis of a model for foam improved oil recovery. *Journal of Fluid Mechanics* **751**, 346–405.

Hallack, M., Heilen, W., Howard, C., Semmler, H., Douglas, C., 2010. Mechanisms for Combating Macro and Microfoam in Low-VOC Waterborne Systems. [Online] Available from: https://www.pcimag.com/articles/90457-mechanisms-for-combating-macro-and-microfoam-in-low-voc-waterborne-systems/ [Accessed: 19 September 2020].

Harris, P. C., 1989. Effects of texture on rheology of foam fracturing fluids. *SPE Production Engineering* **4**(03), 249–257.

Harris Jr, O. A., 1992. A relationship between critical and irreducible water saturations. *Gulf Coast Association of Geological Societies Transactions* **42**, 809–809.

Hirasaki, G. J., 1989. A review of steam-foam process mechanisms. SPE paper 19518 **5**(04), 1–8.

Hirasaki, G. J., 2009. Chapter 7 Two Phase, One Dimensional, Displacement-Lecture Notes in Chemical and Biomolecular Engineering. Rice University, Houston, Texas.

Holm, L. W., 1968. The mechanisms of gas and liquid flow through porous media in the presence of foam. SPE Journal **8**, 359–369.

Holm, L. W., Garrison, W. H., 1988. CO_2 diversion with foam in an immiscible CO_2 field project. *SPE Reser. Engng* **4**, 112–118.

Homsy, G. M., 1987. Viscous fingering in porous media. *Annual review of fluid mechanics* **19**(01), 271–311.

Honarpour, M., Koederitz, L., Harvey, A., 1982. Empirical equations for estimating two-phase relative permeability in consolidated rock. *Journal of Petroleum Technology* **34**(12), 2905–2908.

Hong, S. A., Bae, J. H., Lewis, G. R., 1987. An evaluation of lignosulfonate as a sacrificial adsorbate in surfactant flooding. *SPE Reservoir Engineering* **2**(01), 17–27.

Huh, D. G., Handy, L. L., 1989. Comparison of steady and unsteady-state flow of gas and foaming solution in porous media. *SPE Reservoir Engineering* **4**(01), 77–84.

Islam, M. R., Ali, S. M., 1990. Numerical simulation of foam flow in porous media. *Journal of Canadian Petroleum Technology* **29**(04), 47–51.

Itamura, M. T., Udell, K. S., 1989. The role of noncondensible gases in heat and mass transfer in porous media containing a steam foam. multiphase flow. *Heat and Mass Transfer, ASME HTD* **109**, 87–92.

Jiménez, A. I., Radke, C. J., 1989. Dynamic stability of foam lamellae flowing through a periodically constricted pore. In: Oil-Field Chemistry Enhanced Recovery and Production Stimulation. ACS Publications, 460–469.

Khatib, Z. I., Hirasaki, G. J., Falls, A. H., 1986. Effects of capillary pressure on coalescence and phase mobilities in foams flowing through porous media. *SPE Reser. Engng* **3**(3), 919–926.

Kovscek, A. R., 1998. Reservoir simulation of foam displacement processes. In: *7th UNITAR International Conference on Heavy Crude and Tar Sand, Beijing, China, 27–30 October*.

Kovscek, A. R., Patzek, T. W., Radke, C. J., 1993. Simulation of foam transport in porous media (SPE paper 26402). In: *SPE Annual Technical Conference and Exhibition, Houston, TX, 3–6 October*.

Kovscek, A. R., Patzek, T. W., Radke, C. J., 1997. Mechanistic foam flow simulation in heterogeneous and multidimensional porous media. *SPE Journal* **2**, 511–526.

Kovscek, A. R., Radke, C. J., 1993a. A comprehensive description of transient foam flow in porous media. In: *NIPER Symposium on Field Application of Foams for Oil Production, Bakersfield, CA, 11–12 February*. DOE, pp. FS–9.

Kovscek, A. R., Radke, C. J., 1993b. Fundamentals of foam in porous media. Tech. rep., University of California, Berkeley, California and Lawrence Berkeley Laboratory, Berkeley, California, Bartlesville, Oklahoma (US.), Prepared for the U.S. Department of Energy, Assistant Secretary for Fossil Energy DE93000174.

Kovscek, A. R., Radke, C. J., 1994. Fundamentals of foam transport in porous media. In

Foams: Fundamentals and Applications in the Petroleum Industry (ed. Schramm, L. L.). Advances in Chemistry, Vol. **242**, American Chemical Society, 115–163.

Kovscek, A. R., Tang, G.-Q., Radke, C. J., 2007. Verification of roof snap off as a foam-generation mechanism in porous media at steady state. *Colloids and Surfaces A: Physicochemical and Engineering Aspects* **302**(01), 251–260.

Kraynik, A. M., 1988. Foam flows. *Annual Review of Fluid Mechanics* **20**(01), 325–357.

Kuehne, D. L., Ehman, D. I., Emanuel, A. S., Magnani, C. F., 1990. Design and evaluation of a nitrogen-foam field trial. *Journal of Petroleum Technology* **42**(04), 504–512.

Kuhlman, M. I., Falls, A. H., Hara, S. K., Monger-McClure, T. G., Borchardt, J. K., 1992. CO_2 foam with surfactants used below their critical micelle concentrations. *SPE Reser. Engng.* **7**(04), 445–452.

Kuhlman, M. I., Falls, A. H., Wellington, S. L., 1994. Gas/oil lamallae and surfactant propagation in the oil in carbon dioxide foam (SPE paper-27788MS). In: *SPE/DOE Improved Oil Recovery Symposium, Tulsa, OKlahoma, 17–20 April*, 57–70.

Kular, G. S., Lowe, K., Coombe, D. A., 1989. Foam application in an oil sands steamflood process (SPE paper 19690). In: *SPE Annual Technical Conference and Exhibition, San Antonio, TX, 8–11 October*, 154–162.

Kwok, W., Nasr-El-Din, H. A., Hayes, R. E., Sethi, D., 1993. Static and dynamic adsorption of a non-ionic surfactant on berea sandstone. *Colloids and Surfaces A: Physicochemical and Engineering Aspects* **78**, 193–209.

Lake, L. W., 1989. *Enhanced Oil Recovery*, 3rd Edition. Prentice-Hall, 59–137.

Lau, H. C., O'Brien, S. M., 1988. Surfactant transport through porous media in steam-foam processes. *SPE Reser. Engng.* **3**(04), 1–177.

Lee, H. O., Heller, J. P., 1990. Laboratory measurements of CO_2-foam mobility. *SPE Reservoir Engineering* **5**(02), 193–197.

Leeftink, T. N., Latooij, C. A., Rossen, W. R., 2015. Injectivity errors in simulation of foam EOR. *Journal of Petroleum Science and Engineering* **126**, 26–34.

Lescure, B. M., Claridge, E. L., 1986. CO_2 foam flooding performance vs. rock wettability (SPE paper 15445). In: *SPE Annual Technical Conference and Exhibition, New Orleans, LA, 5–8 October.*

Liu, P. C., Besserer, G. J., 1988. Application of foam injection in triassic pool, Canada: Laboratory and field test results (SPE paper 18080). In: *SPE Annual Technical Conference and Exhibition, Houston, TX, 2–5 October.*

Lotfollahi, M., Farajzadeh, R., Delshad, M., Varavei, A., Rossen, W. R., 2016. Comparison of implicit-texture and population-balance models. *Journal of Natural Gas Science and Engineering* **31**, 184–197.

Manlowe, D. J., Radke, C. J., 1990. A pore-level investigation of foam/oil interactions in porous media. *SPE Reservoir Engineering* **5**(04), 77–84.

Mannhardt, K., Schramm, L. L., Novosad, J. J., 1993. Effect of rock type and brine composition on adsorption of two foam-forming surfactants. *SPE Advanced Technology Series* **1**(01), 212–218.

Marfoe, C. H., Kazemi, H., Ramirez, W. F., 1987. Numerical simulation of foam flow in

porous media (SPE paper 16709). In: *SPE Annual Technical Conference and Exhibition, Dallas, TX, 27–30 September.*

Mas-Hernandez, E., 2016. Modelling foam displacement during improved oil recovery with the pressure-driven growth model. Ph.D. thesis, The University of Manchester, Manchester, UK.

Mohammadi, S. S., Collins, J., Coombe, D. A., 1995. Field application and simulation of foam for gas diversion. In: *8th European Symposium on Improved Oil Recovery, Vienna, Austria, 15–17 May.*

Mohammadi, S. S., Coombe, D. A., 1992. Characteristics of steam/foam drive process in massive multi-zone and thin single zone reservoirs (SPE paper 24030). In: *SPE Western Regional Meeting, Bakersfield, CA, 30 March–1 April.*

Mohanty, K. K., 1981. Fluids in porous media: Two-phase distribution and flow. Ph.D. thesis, University of Minnesota, Minneapolis.

Myers, T. J., Radke, C. J., 2000. Transient foam displacement in the presence of residual oil: experiment and simulation using a population-balance model. *Industrial & engineering chemistry research* **39**(08), 2725–2741.

Nguyen, Q. P., Alexandrov, A. V., Zitha, P. L., Currie, P. K., 2000. Experimental and modeling studies on foam in porous media: a review. In: *SPE International Symposium on Formation Damage Control, Lafayette, Louisiana, 23–24 February.*

Persoff, P., Radke, C. J., Pruess, K., Benson, S. M., Witherspoon, P. A., 1991. A laboratory investigation of foam flow in sandstone at elevated pressure. *SPE Reser. Engng* **6**(03), 365–372.

Ploeg, J. F., Duerksen, J. H., 1985. Two successful steam/foam field tests, sections 15a and 26c, midway-sunset field (SPE paper 13609). In: *SPE California Regional Meeting, Bakersfield, CA, 27–29 March*.

Pope, G. A., 1980. The application of fractional flow theory to enhanced oil recovery. *SPE Journal* **20**(03), 191–205.

Prieditis, J., Paulett, G. S., 1992. CO_2-foam mobility tests at reservoir conditions in San Andres cores (SPE paper 24178). In: *SPE/DOE Eighth Symposium on Enhanced Oil Recovery, Tulsa, Oklahoma, 22–24 April*.

Rankine, W. J. M., 1870. On the thermodynamic theory of waves of finite longitudinal disturbance. *Philosophical Transactions of the Royal Society of London* (160), 277–288.

Ransohoff, T. C., Radke, C. J., 1988. Laminar flow of a wetting liquid along the corners of a predominantly gas-occupied noncircular pore. *Journal of Colloid and Interface Science* **121**(02), 392–401.

Rezk, M. G., Foroozesh, J., 2018. Determination of mass transfer parameters and swelling factor of CO_2-oil systems at high pressures. *International Journal of Heat and Mass Transfer* **126**, 380–390.

Rossen, W. R., 1996. Foams in enhanced oil recovery. In: *Foams: Theory, Measurement and Applications* (ed. R. K. Prud'homme and S. Khan). Vol. **57**. Marcel Dekker, 413–457.

Rossen, W. R., 2003. A critical review of roof snap-off as a mechanism of steady-state foam generation in homogeneous porous media. *Colloids and Surfaces A: Physicochemical and Engineering Aspects* **225**(01), 1–24.

Rossen, W. R., 2008. Comment on "verification of roof snap-off as a foam-generation mechanism in porous media at steady state". *Colloids and Surfaces A: Physicochemical and Engineering Aspects* **322**(01), 261–269.

Rossen, W. R., Gauglitz, P. A., 1990. Percolation theory of creation and mobilization of foams in porous media. *AIChE Journal* **36**(08), 1176–1188.

Rossen, W. R., Lim, M. T., 1995. Injectivity and gravity override in surfactant-alternating-gas foam processes (SPE paper-30753MS). In: *SPE Annual Technical Conference and Exhibition, Dallas, Texas, 22–25 October*, 521–533.

Rossen, W. R., Venkatraman, A., Johns, R. T., Kibodeaux, K. R., Lai, H., Tehrani, N. M., 2011. Fractional flow theory applicable to non-Newtonian behavior in EOR processes. *Transport in Porous Media* **89**(02), 213–236.

Rossen, W. R., Wang, M. W., 1999. Modeling foams for acid diversion. *SPE Journal* **4**(02), 92–100.

Rossen, W. R., Zeilinger, S. C., Shi, J. X., Lim, M. T., 1994. Mechanistic simulation of foam processes in porous media (SPE paper 28940). In: *SPE Annual Technical Conference and Exhibition, New Orleans, LA, 26–28 September.*

Rossen, W. R., Zhou, Z. H., 1995. Modeling foam mobility at the "limiting capillary pressure" (SPE paper 22627). *SPE Advanced Technology Series* **3**(01), 146–153.

Rossen, W. R., Zhou, Z. H., Mamum, C. K., 1991. Modeling foam mobility in porous media (SPE paper 22627). In: *SPE Annual Technical Conference and Exhibition, Dallas, TX, 6–9 October.*

Sagbana, I., Diaz, P., Eneotu, M., Centeno, M., Vajihi, F., Farhadi, A., 2017. Application of low concentration surfactant enhanced water-alternating-gas flooding. In: *19th European Symposium on Improved Oil Recovery, Stavanger, Norway, 24–27 April*, 1–15.

Saint-Jalmes, A., Durian, D. J., 1999. Vanishing elasticity for wet foams: Equivalence with emulsions and role of polydispersity. *Journal of Rheology* **43**(06), 1411–1422.

Sanchez, J. M., Hazlett, R. D., 1992. Foam flow through an oil-wet porous medium: a laboratory study. *SPE Reservoir Engineering* **7**(01), 91–97.

Satter, A., Iqbal, G. M., 2016. *Reservoir engineering: the fundamentals, simulation, and management of conventional and unconventional recoveries*. Gulf Professional Publishing, 343–377.

Schobeiri, M. T., 2010. *Fluid mechanics for engineers: a graduate textbook*. Springer Science & Business Media.

Schramm, L. L., 1994. Foam sensitivity to crude oil in porous media. In: *Foams: Fundamentals, and Applications in the Petroleum Industry* (ed. Schramm. L. L.), *Advances in Chemistry*, Series 242. American Chemical Society, pp. 165–197.

Shan, D., Rossen, W. R., 2004. Optimal injection strategies for foam IOR. *SPE Journal* **9**, 132–150.

Sheng, J. J., 2011. *Modern chemical enhanced oil recovery: theory and practice*. Gulf Professional Publishing.

Sheng, J. J., 2013. Foams and their applications in enhancing oil recovery. In: *Enhanced Oil Recovery Field Case Studies* (ed. Sheng, J. J.). Gulf Professional Publishing, pp. 251–280.

Shi, J. X., 1996. Simulation and experimental studies of foam for enhanced oil recovery. Ph.D. thesis, The University of Texas at Austin, Austin, Texas.

Simjoo, M., Rezaei, T., Andrianov, A., Zitha, P. L. J., 2013. Foam stability in the presence of oil: effect of surfactant concentration and oil type. *Colloids and Surfaces A: Physicochemical and Engineering Aspects* **438**, 148–158.

Skauge, A., Solbakken, J., Ormehaug, P. A., Aarra, M. G., 2020. Foam generation, propagation and stability in porous medium. *Transport in Porous Media* **131**(01), 5–21.

Speight, J. G., 2017. *Rules of thumb for petroleum engineers*. John Wiley & Sons, 59–137.

Suffridge, F. E., Raterman, K. T., Russell, G. C., 1989. Foam performance under reservoir conditions (SPE paper 19691). In: *SPE Annual Technical Conference and Exhibition, San Antonio, TX, 8–11 October*.

Surguchev, L., Manrique, E., Alvarado, V., 2005. Improved oil recovery: status and opportunities (WPC-18-0886). In: *18th World Petroleum Congress, Johannesburg, South Africa, 25–29 September*.

Tang, G. Q., Kovscek, A. R., 2006. Trapped gas fraction during steady-state foam flow. *Transport in porous media* **65**(02), 287–307.

Tang, J., Castañeda, P., Marchesin, D., Rossen, W. R., 2019. Three-phase fractional-flow theory of foam-oil displacement in porous media with multiple steady tates. *Water Resources Research* **55**(12), 10319–10339.

Tanzil, D., Hirasaki, G. J., Miller, C. A., 2002. Mobility of foam in heterogeneous media: Flow parallel and perpendicular to stratification. *SPE Journal* **7**(02), 203–212.

Tarek, A., 2006. *Reservoir Engineering Handbook*, 3rd Edition. Gulf Professional Publishing, 936–1011.

Tarek, A., Nathan, M. D., 2012. *Advanced Reservoir Management and Engineering*, 2nd Edition. Gulf Professional Publishing, 318.

Walsh, M. P., Lake, L. W., 1989. Applying fractional flow theory to solvent flooding and chase fluids. *Journal of Petroleum Science and Engineering* **2**, 281–303.

Walstra, P., 1989. Principles of foam formation and stability. In: *Foams: Physics, chemistry and structure* (ed. A. J. Wilson). Springer, London, pp. 1–15.

Wang, J., Liu, H., Zhang, H., Zhang, G., Liu, P., Sepehrnoori, K., 2015. A novel model of foam flooding considering multi-factors for enhancing oil recovery. *Oil & Gas Science and Technology–Revue d'IFP Energies nouvelles* **70**(06), 1007–1023.

Weaire, D., Hutzler, S., 1999. *The Physics of Foams*. Oxford University Press, New York, 102–116.

Weaire, D., Hutzler, S., Cox, S., Kern, N., Alonso, M. D., Drenckhan, W., 2002. The fluid dynamics of foams. *Journal of Physics: Condensed Matter* 15(01), S65–S73.

Weaire, D., Hutzler, S., Verbist, G., Peters, E., 1997. A review of foam drainage. In *Advances in Chemical Physics* (ed. Prigogine, I. and Rice, S. A.). Advances in Chemical Physics, vol. 102, pp. 315–374.

Weaire, D., Verbist, G., Cox, S. J., Hutzler, S., 2001. Frontiers of the physics of foams. In: *Proceedings of the First International Symposium*. European Space Agency, pp. 103–108.

Welge, H. J., 1952. A simplified method for computing oil recovery by gas or water drive. *Journal of Petroleum Technology* **4**(04), 91–98.

Yaghoobi, H., Heller, J. P., 1996. Effect of capillary contact on CO_2 foam mobility in heterogeneous core samples (SPE paper 35169). In *Permian Basin Oil and Gas Recovery Conference, Midland, TX, 27–29 March*, 245–255.

Zanganeh, M. N., Kam, S. I., LaForce, T., Rossen, W. R., 2011. The method of characteristics applied to oil displacement by foam. *SPE Journal* **16**(01), 8–23.

Zeilinger, S. C., Wang, M., Kibodeaux, K. R., Rossen, W. R., 1995. Improved prediction of foam diversion in matrix acidization. In: *SPE Production Operations Symposium, Tulsa, Oklahoma, 2–4 April*.

Zendehboudi, S., Bahadori, A., 2017. *Shale oil and gas handbook: theory, technologies, and challenges*. Gulf Professional Publishing, 285–319.

Zhang, Z. F., Freedman, V. L., Zhong, T. W., 2009. Foam transport in porous media– a review. Tech. rep., Pacific Northwest National Laboratory, (No. PNNL-18918), Richland, WA (US.), Prepared for the U.S. Department of Energy Under Contract DE-AC05-76Rl01830.

Zhou, Z. H., 1994. Modeling foam flow in porous media and applications to EOR and acidization. Ph.D. thesis, The University of Texas at Austin, Austin, Texas.

Zhou, Z. H., Rossen, W. R., 1992. Applying fractional-flow theory to foams for diversion in matrix acidization (SPE paper 24660). In: *Proceedings of the 67th Annual SPE Technical Conference and Exhibition, Washington DC, 4–7 October*.

Zhou, Z. H., Rossen, W. R., 1994. Applying fractional-flow theory to foams for diversion in matrix acidization. *SPE Production and Facilities* **9** (01), 29–35.

Zhou, Z. H., Rossen, W. R., 1995. Applying fractional-flow theory to foam processes at the 'limiting capillary pressure'. *SPE Advanced Technology Series* **3**(01), 154–162.

Appendix A

Appendix A

In table A.1, we show solutions (for x_D, $S_{w,high}$ and $S_{w,low}$) generated by MATLAB for time intervals before the solution reaches $x_D = 0$. Also, in table A.2, we show solutions generated by MATLAB before the system asymptotes to the slope of the characteristic that corresponds to the theoretical final liquid saturation (i.e. $S_w = 0.4479$). As can be seen, the solution never exactly reaches that value even taken out to comparatively long times, but it asymptotes to that value.

Table A.1: Shock migration up to $x_D = 0$

Dimensionless time t_D	**Shock position** (x_D)	**Liquid saturation behind shock** $S_{w,high}$	**Liquid saturation ahead of shock** $S_{w,low}$	**Shock speed** (dx/dt)
1	−1.9820	0.3964	0.3221	6.782
1.001	−1.9752	0.3964	0.3220	6.7777
1.002	−1.9684	0.3964	0.3219	6.7726
1.003	−1.9617	0.3965	0.3219	6.7674
1.004	−1.9549	0.3965	0.3218	6.7623
1.005	−1.9481	0.3965	0.3217	6.7571
1.006	−1.9414	0.3965	0.3216	6.7519
1.007	−1.9346	0.3966	0.3215	6.7468
1.008	−1.9279	0.3966	0.3215	6.7416
1.009	−1.9211	0.3966	0.3214	6.7364
1.01	−1.9144	0.3967	0.3213	6.7312
1.011	−1.9077	0.3967	0.3212	6.7260
1.012	−1.9009	0.3967	0.3211	6.7208
1.013	−1.8942	0.3967	0.3211	6.7155
1.014	−1.8875	0.3968	0.3210	6.7103
1.015	−1.8808	0.3968	0.3209	6.7051
1.016	−1.8741	0.3968	0.3208	6.6998
1.017	−1.8674	0.3968	0.3207	6.6946
1.018	−1.8607	0.3969	0.3206	6.6893
1.019	−1.8540	0.3969	0.3206	6.6841
1.354	**0.0000**	**0.4110**	**0.2040**	**3.1248**

Table A.2: Shock migration from $x_D = 0$ to final state

Dimensionless time t_D	**Shock position** (x_D)	**Liquid saturation behind shock** $S_{w,high}$	**Liquid saturation ahead of shock** $S_{w,low}$	**Shock speed** (dx/dt)
1.354	0.0000	0.4110	0.2024	3.1009
1.354	0.0000	0.4110	0.2000	3.0657
1.454	0.3066	0.4188		3.1463
1.554	0.6212	0.4238		3.1850
1.654	0.9397	0.4273		3.2066
1.754	1.2604	0.4299		3.2200
1.854	1.5824	0.4320		3.2288
1.954	1.9052	0.4336		3.2349
2.054	2.2287	0.4349		3.2394
2.154	2.5527	0.4359		3.2427
2.254	2.8769	0.4369		3.2452
2.354	3.2014	0.4376		3.2472
2.454	3.5262	0.4383		3.2488
2.554	3.8511	0.4389		3.2501
2.654	4.1761	0.4394		3.2512
2.754	4.5012	0.4399		3.2521
2.854	4.8264	0.4403		3.2528
2.954	5.1517	0.4407		3.2535
3.054	5.4770	0.4410		3.2540
3.154	5.8024	0.4414		3.2545
3.254	6.1279	0.4416		3.2549
144.054	**465.0153**	**0.4478**		**3.2592**